

AN ELECTRIC PROPULSION CONCEPT BASED ON DIRECT ION ACCELERATION WITH BEATING ELECTROSTATIC WAVES

BAYARD G. GARDINEER, IV

Class of 2011

SUBMITTED TO THE
DEPARTMENT OF MECHANICAL AND AEROSPACE ENGINEERING,
PRINCETON UNIVERSITY,

IN PARTIAL FULFILLMENT OF THE REQUIREMENTS OF
UNDERGRADUATE INDEPENDENT WORK

AND THE
ENGINEERING PHYSICS CERTIFICATE.

FINAL REPORT

APRIL 28, 2011

PROF. EDGAR Y. CHOEIRI

PROF. SZYMON SUCKEWER

MAE 442

111 PAGES

FILE COPY

COLOR PRINTING

© by Bayard Gilbert Gardineer, IV, 2011.
All Rights Reserved.

Abstract

A theoretical and numerical investigation of a novel electric propulsion concept based on direct ion acceleration with beating electrostatic waves (BEW) is conducted, with the goal of demonstrating its validity and feasibility as a potential plasma thruster concept. It is hoped that this acceleration mechanism will form the basis of a new Beating Wave Thruster (BWT) that is electrodeless, efficient, and variable in its operation.

Numerical studies and simulations are conducted for a thermalized ion ensemble in the absence of BEW (the “unperturbed” case) to demonstrate that a rectilinear magnetic slope configuration generates a net linear ion current along the magnetic null. Optimal unperturbed thruster geometries are determined, and benchmark specific impulse and thrust values are calculated. Beating waves are introduced into the Hamiltonian and a thorough investigation of the corresponding “perturbed” case is conducted. Perturbed ion trajectories are elucidated, and a phenomenon referred to as “ion channeling” is demonstrated, in which stochastic ions are preferentially transported away from the thruster walls and towards the magnetic null. The ability of BEW to push ions from trapped orbits into forward-drifting trajectories is demonstrated. Under the right conditions, BEW are shown to increase the number of ions subject to forward-drifting orbits as well as the exit velocity of ions that were already following forward-drifting trajectories prior to BEW propagation. It is postulated that lowering the stochastic acceleration threshold is an effective method of increasing overall thruster performance. Optimal wave parameters are determined from the electrostatic ion cyclotron wave dispersion relation, and numerical simulations are conducted using Monte Carlo methods to determine ensemble behavior in both the

single and beating wave cases. BEW is shown to be superior for the chosen wave parameters. Theoretical thrust density and specific impulse values for the BWT are calculated, and shown to be comparable to existing Hall and ion thruster configurations. It is concluded that the Beating Wave Thruster has the potential to be an effective and efficient electric propulsion device, and that subsequent investigation and experimentation related to the BWT is both warranted and encouraged.

Acknowledgements

In this, the culmination of my Princeton career, I am so grateful to so many. Here are just a few of the people to whom I owe outstanding debts of gratitude:

To my adviser and mentor, Professor Edgar Choueiri, whose invitation for me to work in his lab the summer after my freshman year quite literally changed the course of my life. I thank you for introducing me to plasmas, for your support, and for your friendship. And also, for 3-D audio, David Blaine, and cool magic tricks.

To Ben Jorns, whose guidance throughout this entire process was both immeasurable and invaluable. With your combination of brilliance and patience, I have no doubt that you will do great things.

To fellow EPPDyLites Dan Lev, Justin Little, and Matthew Feldmann, for the many stimulating discussions that took place in the dreary depths of the E-Quad. Now that the resident undergrad is gone, I'm counting on you guys to hold down the fort. And yes, I know I don't have a Master's degree. But neither does Matthew. Yet.

To Bob Sorenson, whose economic and political musings over the past four years have made me seriously consider investing in gold. Thank you for all your advice and guidance.

To Master Jeff Nunokawa, whose three-hour dinner conversations limited my sleep, but expanded my mind.

To the Princeton Triangle Club, for giving me a home when I had none, and for instilling in me an appreciation for theater and the arts that I will carry with me for as long as I live.

To my top three – Ray Brusca, Nick DiBerardino, and Yoel Bitran. You guys made all of the late nights bearable, and all of the nights out memorable. Thanks for being friends with me even though I’m in Tower.

To my sister, Sarah, for her 4am Facebook posts assuring me that I was not the only Gardineer who was awake. With your tenacity, I’m sure you will succeed in whatever you choose to pursue.

To my brother, Alex, for being a good brother, and a good kid. Enjoy your time in college. It’s over before you know it.

And last, but certainly not least, to my parents. Everything I have, I owe to you. From practicing my multiplication tables at the bus stop in Skillman to this very moment, you have supported me wholeheartedly in all of my endeavors. And for that, I am, and always will be, eternally grateful.

The Earth is the cradle of humanity, but
mankind cannot stay in the cradle forever.

Konstantin E. Tsiolkovsky

Contents

Abstract	ii
Acknowledgements	iv
1 Introduction	1
1.1 Overview	1
1.2 Fundamentals of Spacecraft Propulsion	1
1.3 Limitations of Chemical Rockets	3
1.4 Merits of Electric Propulsion	5
1.5 A Novel Plasma Propulsion Mechanism	7
1.6 Organization of This Thesis	8
2 Beating Wave Phenomenon	10
2.1 Observations	10
2.2 Theoretical Foundation	12
2.3 Analytical and Numerical Formulation	14
2.3.1 Single Electrostatic Wave (SEW) Acceleration	15
2.3.2 Beating Electrostatic Wave (BEW) Acceleration	19
2.4 Propulsive Applications	26
3 Beating Wave Thruster (BWT) Concept	27

3.1	Magnetic Field Topography	27
3.2	Hamiltonian Formulation	29
3.3	Unperturbed Ion Trajectories ($\varepsilon = 0$)	31
3.4	Orbit Domain Representations	35
3.5	Ensemble Behavior (k -normalized)	42
3.5.1	$\bar{\rho}$ Optimization	44
3.6	Alternative Hamiltonian Formulation	46
3.7	Ensemble Behavior ($\bar{\rho}_L$ -normalized)	47
3.7.1	L Optimization	48
3.8	Benchmark Specific Impulse	49
3.9	Benchmark Thrust	51
3.10	Introduction to the Perturbed Case ($\varepsilon \neq 0$)	53
4	Effects of BEW Propagation	54
4.1	Perturbed Ion Trajectories ($\varepsilon \neq 0$)	54
4.2	Ion Channeling	60
4.3	EIC Dispersion Relation	61
4.4	BWT Specific Impulse Estimate	63
4.5	Optimization Procedure	68
4.6	BWT Thrust Estimate	69
4.7	Summary of Results	70
5	Conclusions and Future Work	71
5.1	Conclusions	71
5.2	Future Work	72
5.2.1	Continued Theoretical Development	72
5.2.2	Simulation Improvements	73

5.2.3	Proof-of-Concept Demonstration	75
A	Hamiltonian Mechanics	78
A.1	The Hamiltonian Formulation	78
A.2	Numerical Methods	79
A.2.1	Separable Case	80
A.2.2	Nonseparable Case	80
B	Derivation of the Hamiltonian	81
B.1	Arbitrary B-field	81
B.2	Rectilinear (z -directed) B-field	82
B.2.1	Case 1: UNIFORM	82
B.2.2	Case 2: y -DEPENDENCE	83
B.2.3	Case 3: x - AND y -DEPENDENCE	84
B.3	Canonical Transformations	84
C	Maxwellian Distributions	87

List of Figures

1.1	Electric vs. Chemical Propulsion	7
2.1	S3-3 Data and the CIF	11
2.2	Off-Resonant SEW Poincaré Sections	16
2.3	Off-Resonant SEW Ion Trajectories	17
2.4	On-Resonant SEW Poincaré Sections	18
2.5	On-Resonant SEW Ion Trajectories	18
2.6	Off-Resonant SEW vs. BEW Poincaré Sections	19
2.7	BEW Acceleration Domains	21
2.8	Off-Resonant BEW Ion Trajectories	22
2.9	BEW Poincaré Sections for Various ε and ν_1	24
2.10	On-Resonant BEW Poincaré Section and Ion Trajectories	25
3.1	Magnetic Slope Configuration	28
3.2	Effective Potential ($\varepsilon = 0$)	32
3.3	Ion Trajectories for $P_X > 0$	33
3.4	Ion Energies for $P_X < 0$	34
3.5	Ion Trajectories for $P_X < 0$	34
3.6	Orbit Domains (P_X - \mathcal{H}_k Plane)	36
3.7	Orbit Domains (Y_{GC} - ρ Plane)	39

3.8	Orbit Domains for Varying $\bar{\delta}$	41
3.9	k -normalized Ensemble Contours	43
3.10	$\bar{\rho}$ Optimization	45
3.11	Optimal Configuration ($\bar{\rho}$)	46
3.12	Optimal Configuration (L)	48
3.13	Ion Trajectory Distribution (X - Y Plane)	49
3.14	Unperturbed Exit Velocity Distribution	50
4.1	Perturbed Ion Trajectories ($\rho_0 < \rho_f < \rho_{th}$)	56
4.2	Perturbed Ion Trajectories ($\rho_0 < \rho_{th} < \rho_f$)	57
4.3	Perturbed Ion Trajectories ($\rho_{th} < \rho_0 < \rho_f$)	58
4.4	Perturbed Ion Trajectories ($\rho_0 > \rho_f$)	59
4.5	Ion Channeling	61
4.6	EIC Dispersion Relation	62
4.7	SEW vs. BEW – Exit Velocity Distributions	65
5.1	Magnetic Field Generation	76

List of Tables

1.1	Chemical Propellant Characteristics	4
1.2	Δv for Various Missions	4
1.3	Electric Thruster Characteristics	6

List of Symbols

\mathbf{T}	Thrust
I_{sp}	Specific impulse
u_{ex}	Exhaust velocity
g_0	Standard gravity (sea-level)
\dot{m}	Time rate of change of rocket mass
m_i	Initial rocket mass
m_f	Final rocket mass
m_p	Propellant mass
Δv	Velocity increment
\mathbf{v}	Velocity
\mathbf{B}	Magnetic field
ω_{ci}	Ion cyclotron frequency
\bar{v}	Root mean square (RMS) velocity
v_{\perp}	Perpendicular velocity (relative to \mathbf{B})
\mathbb{N}	Set of positive integers
q	Ion charge
m	Ion mass
E_0	Electric field amplitude
\mathbf{q}	Generalized coordinate

\mathbf{p}	Generalized momentum
v_{ph}	Wave phase velocity
ω	Wave frequency
k	Wave number
φ	Wave phase
ν	Normalized wave frequency
κ	Normalized wave number
ε	Normalized wave amplitude
ε_{th}	Stochastic amplitude threshold
τ	Normalized time
τ_c	Poincaré section sampling period
ρ	Normalized Larmor radius
θ	Cyclotron phase angle
ρ_{th}	Stochastic Larmor radius threshold
ρ_{UB}	Stochastic Larmor radius upper bound
$\bar{\rho}_L$	RMS Larmor radius
$\bar{\rho}$	Normalized RMS Larmor radius
h	Hamiltonian
\mathcal{H}_k	k -normalized Hamiltonian
$\mathcal{H}_{\bar{\rho}_L}$	$\bar{\rho}_L$ -normalized Hamiltonian
u_e	Normalized average energy density
$\rho_s(\theta)$	Separatrix between regular and forbidden acceleration regions
δ	Half-width of magnetic slope
$\bar{\delta}$	Normalized half-width of magnetic slope
\mathbf{A}	Magnetic vector potential

ϕ	Electrostatic potential
\mathbf{P}	Normalized momentum
$\overline{\mathbf{A}}$	Normalized vector potential
(X_{GC}, Y_{GC})	Normalized guiding center coordinates
\mathcal{L}	Lagrangian
T	Kinetic energy
V	Potential energy
V_{eff}	Effective potential
L	Thruster bound
ξ_f	Fraction of forward-drifting ions
ξ_{esc}	Fraction of ions that escape to the walls
ξ_{ex}	Fraction of ions that breach the exit plane
$V_{X,Y}$	Normalized velocity
U_{ex}	Normalized exhaust velocity
T_i	Ion temperature
T_e	Electron temperature
T_r	Ratio of T_e to T_i
n	Ion density
A	Thruster cross-sectional area
T_i	Ion temperature
ℓ	Thruster depth (in z)
k_B	Boltzmann's constant
ρ_f	Forward-drifting Larmor radius threshold
Z	Ion charge (in units of e)
$ Y_{UB} $	Y upper bound for forward-drifting ions

Chapter 1

Introduction

1.1 Overview

The main goal of this thesis is to demonstrate the validity and feasibility of a new plasma propulsion concept that uses beating electrostatic waves (BEW) coupled with a steeply-sloped rectilinear magnetic field to generate thrust via direct ion acceleration. It is hoped that this acceleration mechanism will form the basis of a high specific impulse Beating Wave Thruster (BWT) that is electrodeless, efficient, and variable in its operation via the manipulation of wave and plasma parameters. This thruster concept was initially proposed by Jorns and Choueiri in 2010 [1].

We begin this introductory chapter with a broad overview of space flight fundamentals, followed by a brief discussion of the deficiencies of chemical rockets and the motivation for electric propulsion. We go on to discuss some of the foreseeable advantages of the Beating Wave Thruster over other propulsive configurations, and conclude with a detailed description of the organization of the remainder of this thesis.

1.2 Fundamentals of Spacecraft Propulsion

Rockets accelerate by expelling a portion of their mass (propellant) opposite the direction of desired acceleration. By Newton's third law, this expulsion produces a reaction force called thrust that causes the rocket to accelerate. Thrust is vectorially defined as

$$\mathbf{T} = \dot{m}\mathbf{u}_{ex} \tag{1.1}$$

where \dot{m} is the rate of change of rocket mass and \mathbf{u}_{ex} is the propellant exhaust velocity

vector as defined in the rest frame of the spacecraft.

A practical quantity to investigate is the magnitude of thrust produced per unit flow of propellant mass. In the interest of mass savings, it is clearly desirable for this ratio to be large. Normalizing this quantity by one standard gravity g_0 yields the specific impulse I_{sp} of the rocket:

$$I_{sp} = \frac{\dot{m}u_{ex}}{\dot{m}g_0} = \frac{u_{ex}}{g_0} \quad (1.2)$$

Note that I_{sp} has units of time and is simply the exhaust velocity divided by $g_0 \approx 9.81$ m/s². The quantity I_{sp} is often defined as the total impulse (or change in momentum) delivered per unit weight of fuel consumed.

The total mass of propellant required to complete a particular mission is dictated by the general rocket equation. By Newton's second law, in the absence of external forces (and for $v \ll c$), a rocket in vacuum has the following equation of motion:

$$m\dot{\mathbf{v}} = \dot{m}\mathbf{u}_{ex} \quad (1.3)$$

A solution to this first-order ODE can be obtained via simple separation of variables, yielding Tsiolkovsky's famous rocket equation:

$$\frac{m_f}{m_i} = e^{-\Delta v/u_{ex}} \quad (1.4)$$

where m_i and m_f denote the initial and final masses of the rocket, respectively, and Δv (or delta-v) denotes the total velocity increment required for the rocket to execute the orbital maneuver in question. When expressed in terms of the propellant mass m_p , the rocket equation becomes

$$\frac{m_p}{m_i} = 1 - e^{-\Delta v/u_{ex}} \quad (1.5)$$

Eq. (1.5) reveals that the minimum mass fraction of propellant required to complete a particular mission increases exponentially with delta-v. However, from a design perspective, for a given delta-v, the required propellant mass fraction decreases exponentially with increasing exhaust velocity. Thus, in order for an appreciable fraction of the rocket's initial mass to be accelerated to the final velocity, u_{ex} and Δv must be of comparable magnitude [2].

Due to the proportionality of specific impulse and exhaust velocity, I_{sp} is often

used to gauge the propellant mass efficiency of rocket propulsion systems.

1.3 Limitations of Chemical Rockets

Most spacecraft use conventional chemical rockets to accelerate their payloads. In these devices, chemicals react or decompose to produce large amounts of heat and subsequently increase the temperature of the post-reaction mixture. Thrust is generated by expanding this heated mixture through a de Laval (convergent-divergent) nozzle prior to ejection. While chemical rockets are capable of generating large thrust, their exhaust velocities are inherently limited by three factors: 1) the maximum heat generated in the relevant chemical reactions, 2) the tolerable heat transfer to the combustion chamber and nozzle throat due to material limitations, and 3) the unrecoverable loss of energy to both the internal rotational and vibrational modes of the gas (“frozen flow losses”) and the radiation emitted from the exhaust jet [2].

Table 1.1 features typical exhaust velocities for a variety of chemical rockets, while Table 1.2 features delta- v values for a number of potential space missions. Inspection of these data reveals that the exhaust velocities of standard chemical rockets are generally much smaller than the delta- v values required to accomplish many missions of interest. This deficiency effectively renders most interplanetary and deep space missions infeasible due to the severe constraints it places on the required propellant mass fraction. For example, even for an “exotic” propellant with a comparatively high exhaust velocity of 6.0 km/s^1 , by Eq. 1.5, a sample return mission to Mars would require approximately 99.7 percent of the rocket’s initial mass to be fuel; thus, every kilogram of payload would require approximately 290 kilograms of propellant to make the full trip. However, since “exotic” propellants are rarely used², a more realistic calculation features the use of a liquid bipropellant rocket fueled by (for example) liquid hydrogen and liquid oxygen ($u_{ex} \approx 4.5 \text{ km/s}$) [4]. This is the bipropellant combination used in the Space Shuttle Main Engine (SSME). Thus, for the SSME to complete a Mars sample return mission, every kilogram of useful payload would

¹This exhaust velocity value is a theoretical maximum. The highest specific impulse ever achieved by a chemical rocket in the laboratory to date was 5.32 km/s using a tripropellant mixture of lithium, fluorine, and hydrogen [3].

²Despite their high exhaust velocities, “exotic” propellants are often unrealistic due to material considerations that stem from substance volatility, elevated chamber temperatures, and corrosive combustion products [2].

Table 1.1. Typical exhaust velocity and specific impulse values for various chemical rockets. Taken from Ref. [2].

<i>Propellant Type</i>	$u_{ex}, km/s$	I_{sp}, s
Liquid monopropellants	1.7–2.9	170–300
Solid propellants	2.1–3.2	200–325
Liquid bipropellants (fuel and oxidizer)	2.9–4.5	300–450
“Exotic” bipropellants and tripropellants	4.0–6.0	400–600

Table 1.2. Characteristic Δv values for several hypothetical missions. Taken from Ref. [2].

<i>Mission</i>	$\Delta v, km/s$
Escape from earth surface (impulsive)	11.2
Escape from 300-mile orbit (impulsive)	3.15
Escape from 300-mile orbit (gentle spiral)	7.59
Earth orbit to Mars orbit and return	14
Earth surface to Mars surface and return	34
Earth orbit to Venus orbit and return	16
Earth orbit to Mercury orbit and return	31
Earth orbit to Jupiter orbit and return	64
Earth orbit to Saturn orbit and return	110

require nearly 2,000 kilograms of propellant – clearly a colossal amount.

Thus, while high-thrust chemical propulsion is still necessary for spacecraft to overcome the strong drag and gravitational forces associated with launch and low-altitude flight, it is highly impractical to use chemical rockets for missions with large Δv requirements due to intrinsic limitations on propellant exhaust velocity. Delivery of an appreciable payload to a distant destination via chemical propulsion alone would require an unprecedentedly massive rocket, the construction of which would present a slew of significant structural challenges, as well as nontrivial increases in overall mission cost (due to the comparative excess of required propellant and materials). Thus, in order for deep space travel to become a reality, the situational deficiencies of chemical rockets must be acknowledged and alternate (nonchemical) means of propulsion must be considered.

1.4 Merits of Electric Propulsion

One particularly promising method of nonchemical propulsion is electric propulsion. Electric propulsion (EP) is defined as “the acceleration of gases for propulsion by...electric and magnetic body forces”³ [2]. Since electric and magnetic fields exert forces only on charged particles, the reaction mass of an electric thruster must take the form of an ionized gas (or plasma) in order to experience electromagnetic body forces. Thus, while chemical propulsion produces thrust via a chemical reaction, electric propulsion produces thrust via the electromagnetic acceleration of a bulk plasma.

As stated in the previous section, one of the main disadvantages of chemical propulsion is that it is “energy limited” – reactants have a fixed amount of energy per unit mass, and this limitation places a strict upper bound on the maximum specific impulse attainable by a chemical rocket engine. One principal advantage of EP is that it is not energy limited; in theory, an arbitrarily large amount of energy can be delivered to the ionized propellant without the intrinsic limitations associated with the breaking and forming of chemical bonds. This allows electric thrusters to have much higher exhaust velocities than their chemical counterparts. However, all electric thrusters must pay a power supply penalty, and as such, are inherently “power limited” – the rate at which energy is delivered to the propellant is limited by the mass of the onboard power supply (which clearly cannot be arbitrarily large). Power delivery in electric thrusters tends to be several orders of magnitude lower than power delivery in chemical rockets. As a result, thrust generation is limited (on the order of mN) and thrust-to-mass ratios are very low for EP systems. This limitation lengthens the time required for electrically-propelled spacecraft to execute short-range maneuvers [5]. Table 1.3 features typical I_{sp} values for a variety of thruster, propellant, and power level combinations.

The high exhaust velocities of electric thrusters make them particularly well-suited for deep space missions with large delta- v requirements. However, electric thrusters are not impulsive; they generate thrust continuously via the gradual expulsion of propellant over extended periods of time. As a result, while the thrust produced in an impulsive maneuver effectively only accelerates the spacecraft, the thrust generated in a gradual maneuver accelerates both the spacecraft and the unused propellant

³For the purpose of clarity, this definition purposefully omits electrothermal propulsion, “wherein the propellant gas is heated electrically, then expanded in a suitable nozzle” [2].

Table 1.3. Typical I_{sp} values for various electric thruster configurations. Adapted from Ref. [6].

<i>Thruster</i>	<i>Propellant</i>	<i>Power Range, kW</i>	<i>I_{sp}, s</i>
Hall	Xe	0.3 – 6	1600
Ion	Xe	0.2 – 4	2800
PPT	Teflon	< 0.2	1000
FEED	Cs	< 0.001	6000
MPD (applied field)	H ₂ /NH ₃ /Ar	1 – 100	2000–5000
MPD (self-field)	H ₂ /NH ₃ /Ar	200 – 4000	2000–5000

required to complete said maneuver. Thus, for a given mission, the calculated delta-v for low-thrust electric propulsion is always higher than the corresponding delta-v for impulsive chemical propulsion.

Despite this discrepancy, however, due to their exceedingly high exhaust velocities, electric thrusters still tend to be much more mass efficient than their chemical counterparts. For example, if we consider escape from a 300-mile Earth-bound orbit (see Table 1.2), the required delta-v value for a gradual maneuver exceeds that of an impulsive maneuver by a factor of nearly 2.5 (7.59 km/s versus 3.15 km/s). However, while a typical liquid bipropellant rocket ($I_{sp} \approx 450$ s) would require approximately 1 kilogram of propellant per kilogram of payload to execute such a maneuver, a Xe ion thruster ($I_{sp} \approx 2800$ s) would require only about 0.3 kilograms of propellant per kilogram of payload. Thus, despite the appreciable delta-v discrepancy, an ion thruster would still require less than a third of the propellant mass required for a chemical rocket to complete the same maneuver.

The downside is that using a Xe thruster would also result in a much longer trip time due to the low-thrust characteristics of electric propulsion systems. On larger timescales, however, the low, continuous thrust of electric propulsion has the potential to accelerate spacecraft to much higher final velocities than the impulsive thrust of conventional chemical rockets. This corresponds to significant time savings when considering deep space missions over extended time periods (see Figure 1.1).

Therefore, while electric thrusters generate low thrust and cannot be employed effectively in the presence of large drag and/or gravitational forces, their high exhaust velocities render them extremely mass efficient, making them very attractive for missions with large delta-v requirements. Furthermore, the comparatively high efficiency of electric thrusters essentially validates the feasibility of many interplanetary and

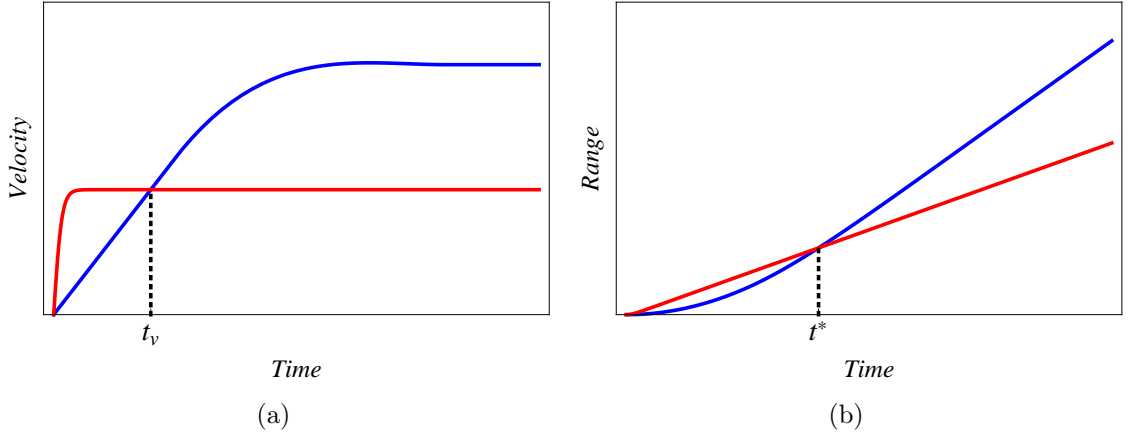


Figure 1.1. Velocity and range profiles for chemical (red) and electric (blue) propulsion systems over the course of an extended mission in free space. (a) While electric propulsion accelerates the spacecraft very slowly, after a time t_v , an EP spacecraft can actually surpass the maximum attainable velocity of a chemically-propelled rocket. (b) After a certain time t^* , the *average* velocity of an electrically-propelled spacecraft will also surpass that of a chemical rocket, at which point electric propulsion also proves more time efficient than chemical propulsion.

deep space missions that would otherwise be impossible using only current chemical means of propulsion.

1.5 A Novel Plasma Propulsion Mechanism

In 2010, Jorns and Choueiri proposed a new electric propulsion concept based on direct ion acceleration with beating electrostatic waves (BEW) [1]. The acceleration mechanism at the heart of this concept relies on BEW propagation to augment the linear ion current generated in a thermalized plasma by a steeply-sloped rectilinear applied magnetic field. As previously stated, the ultimate goal is for this mechanism to form the basis of a new plasma propulsion engine that we call the Beating Wave Thruster (BWT). The BWT has three principal characteristics that render it an attractive potential propulsion device:

Improved Lifetime

Electrode erosion hinders thruster performance and can ultimately lead to catastrophic structural failure. As a result, it is a life-limiting process for a variety of thruster classes, including MPD, ion, and Hall effect thrusters [7, 8]. The BWT con-

cept is electrodeless, and as such, offers the potential benefit of improved lifetime over other electric thruster configurations. Only the physical walls of the BWT interior are subject to ion and electron bombardment. However, as will be shown in Chapter 4, the BEW mechanism tends to preferentially transport ions away from the walls and towards the magnetic null at the center of the thruster. Thus, it is hoped that the BWT will also experience reduced sputtering from the thruster interior.

High Efficiency

As an EP device, the BWT is expected to have a specific impulse that is vastly superior to chemical rockets. Furthermore, the aforementioned “ion channeling” transport mechanism (whereby ions are preferentially siphoned towards the magnetic null) will serve to limit plasma-wall interactions, a source of appreciable energy losses in Hall thrusters [9]. Lastly, because ion acceleration is generally confined to the linear region along the magnetic null, the exhaust stream is expected to possess a beam-like character with minimal plume divergence, thereby minimizing momentum losses in the z -direction.

Variable Thrust and Specific Impulse

The BEW acceleration mechanism is affected by the frequency, amplitude, and wave number of the exciting waves [10]. Therefore, it is expected that variations in these parameters will correspond to changes in BWT specific impulse and thrust output. The ability to actively manipulate these thruster characteristics is clearly advantageous from a mission optimization standpoint, both in terms of thruster versatility and overall power consumption [11]. Furthermore, since heating the plasma (either in the ionization stage itself or in an intermediate stage) increases the average Larmor radius of the ion ensemble, it will also result in more pronounced ion trajectories. Thus, increasing the temperature of the plasma may be one method of improving both the thrust and the specific impulse of the BWT.

1.6 Organization of This Thesis

The goal of this thesis is simple: to demonstrate the effectiveness of BEW direct ion acceleration as an electromagnetic propulsion mechanism, and to lay the foundation

for the development of a new electric thruster that is based on said mechanism.

We begin in Chapter 2 with a literature review of ion acceleration by electrostatic waves, followed by a description of the analytical and numerical formulations of both the single and beating wave cases. In the latter section, we review much of the theoretical and numerical work conducted by Spektor – and subsequently, Jorns – and Choueiri in the area of BEW acceleration. We conclude with a discussion of the potential propulsive applications of the beating wave phenomenon. In Chapter 3, we introduce the fundamentals of the Beating Wave Thruster concept. We start with a description of magnetic field topography, followed by a Hamiltonian description of the single-ion problem. We follow the procedure of Jorns and Choueiri [1] to fully elucidate single-ion dynamics in the absence of BEW, and subsequently extend our analysis to a thermalized distribution of ions (constrained by thruster geometry) to demonstrate that this particular field configuration does indeed produce a net ion current in one direction. We then determine benchmark specific impulse and thrust levels for a collisionless Maxwellian ion ensemble in the presence of a steep magnetic slope via numerical simulation, and derive optimal configuration parameters under two different normalization schemes. In Chapter 4, we introduce beating waves into the system and conduct an investigation of ion dynamics in the perturbed case. We discuss how (under the right conditions) BEW acceleration can increase both the number and the velocity of ions that propagate along the magnetic null. We also discuss the tendency of BEW to preferentially transport ions away from the thruster walls and towards the magnetic null, a phenomenon which we refer to as “ion channeling.” We then introduce a degree of physical fidelity in the form of the electrostatic ion cyclotron wave dispersion relation, and determine optimal wave parameters to maximize BWT performance. We subsequently determine specific impulse and thrust values for both single and beating waves via numerical simulation, and the cases are compared. Finally, in Chapter 5, we summarize the major results of this thesis, and conclude with a discussion of open questions and potential directions for future research.

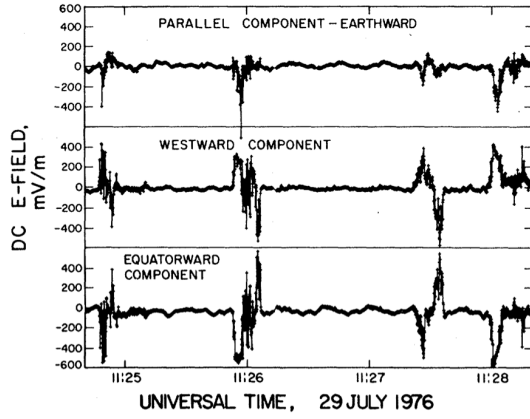
Chapter 2

Beating Wave Phenomenon

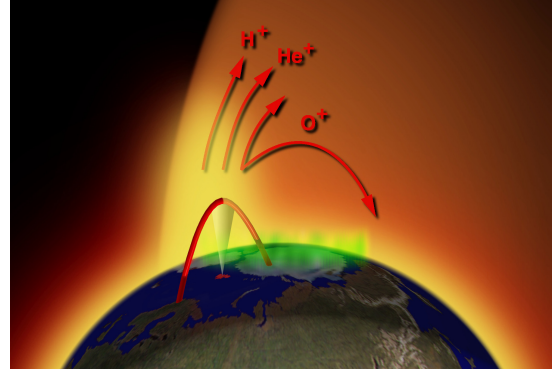
Beating Electrostatic Wave (BEW) acceleration in plasmas is a critical component of the Beating Wave Thruster (BWT) propulsion concept. This chapter seeks to characterize the BEW acceleration mechanism in necessary detail. We begin with an extensive literature review of this well-documented phenomenon followed by a description of the analytical and numerical formulation of the problem. We conclude with a discussion of the BEW acceleration mechanism in a propulsive context.

2.1 Observations

In the summer of 1976, the S3-3 satellite made the first ever *in situ* electric field measurements in the auroral region of the upper ionosphere [12]. The following year, citing S3-3 field data collected on July 29, 1976, Mozer *et al* documented a naturally occurring electrostatic phenomenon in the Earth's auroral zone at a reference altitude of approximately 7600 km and a magnetic latitude near 76° [13]. Spatially confined pairs of oppositely directed electric field spikes were observed at numerous points in the orbit and were found to possess large transverse components (~ 400 mV/m; see Figure 2.1(a)). Mozer and his team identified these spiked structures as paired electrostatic shocks resulting from the turbulent propagation of electrostatic ion cyclotron (EIC) waves. Furthermore, they found that in the vicinity of these large-field regions, oxygen and hydrogen ions were accelerated to energies of a few kilovolts between the satellite and the ionosphere, implying that EIC wave-particle interactions may be the root cause of ion acceleration in the upper ionosphere. In 1979, Kintner *et al* conducted a comparative study of upstreaming ions in the keV range and EIC wave propagation using S3-3 data and found these events to coincide



(a) S3-3 Auroral Electric Field Measurements



(b) Cleft Ion Fountain (CIF)

Figure 2.1. (a) Electric field component measurements made by the S3-3 satellite in a magnetic-field-oriented, nonrotating frame at an altitude of 7600 km in the northern auroral zone. Figure is taken from Ref. [13]. (b) Artist's depiction of the Cleft Ion Fountain (CIF), as well as the proposed trajectory of CAPER (Cleft Accelerated Plasma Experimental Rocket), an experimental rocket launched in January of 1999 to investigate accelerated ion behavior and CIF properties. This figure is taken from Ref. [17].

in more than 90% of the cases reviewed. The study also showed that EIC waves and energetic ions (>500 eV) exhibit a common floor in their altitude distributions near 5000 km, which further implies a causal relationship between these phenomena [14]. Ungstrup and Klumpar theorized a similar EIC acceleration mechanism in that same year, citing significant transverse acceleration components (measured by Isis 1 and 2) as a strong indicator that EIC waves propagating perpendicularly to the Earth's magnetic field were responsible for the observed ion upstreaming [15, 16]. They concluded that transverse excitation was converted to parallel motion via the magnetic mirror force due to the presence of significant ∇B in the polar regions.

Observations of prodigious ion acceleration in the topside ionosphere span several decades. Vela 4 [18], Topaz 3 [19], Isis 1 and 2 [20], and a variety of other satellites and sounding rockets [17, 21, 22, 23] have all successfully documented this phenomenon, thereby confirming the existence of high-energy magnetospheric ions of ionospheric origin. This acceleration has been most readily observable in the vicinity of the Cleft Ion Fountain (CIF), a naturally-occurring ion source in the topside polar region (see Figure 2.1(b)). First characterized by Lockwood *et al* in 1985, the CIF is a massive, well-documented outflow of highly energetic ions from the polar ionosphere that serves as a significant plasma source for the Earth's magnetosphere [24, 25, 26]. Intense

interest in the physics behind this ion injection mechanism and related phenomena served to motivate much of the theoretical and experimental work surrounding EIC wave-particle interactions in the decades to follow.

2.2 Theoretical Foundation

Early experiments intended to simulate ionospheric acceleration showed that plasma subject to a single EIC wave propagating above the ion cyclotron frequency ω_{ci} experienced significant ion heating under certain conditions [27, 28, 29, 30, 31]. In 1977, Karney and Bers theoretically demonstrated that an ion subject to a single perpendicularly propagating electrostatic wave (again, for $\omega > \omega_{ci}$) can only be accelerated if the wave amplitude exceeds a certain threshold. They also determined that the acceleration mechanism is stochastic in nature. Furthermore, in the presence of a given electrostatic wave, an ion will only accelerate if its perpendicular velocity v_{\perp} places it within a certain closed region of phase space, the lower bound of which is approximately equal to the phase velocity of the exciting wave v_{ph} [32]. Below this threshold, no such acceleration is observed. This implies that in order for an ion to exchange appreciable energy with a single electrostatic wave, its velocity must essentially be in a “broadened resonance” with the wave. Thus, phase space for a magnetized ion subject to a single perpendicularly propagating electrostatic wave can be divided into two regions of ion motion: a *forbidden* region (for $v_{\perp} \lesssim v_{ph}$), where wave-ion interactions are small and ion motion is coherent, and a *stochastic* region (for $v_{\perp} \gtrsim v_{ph}$), where an ion strongly interacts with the exciting wave and the resulting ion motion is effectively chaotic.¹ Single electrostatic wave (SEW) acceleration is therefore always stochastic.²

However, this single-wave model did not match the ion acceleration observed in the upper ionosphere [19]. In 1998, Ram *et al* proposed that particle interactions with a *spectrum* of electrostatic waves propagating perpendicularly to the Earth’s magnetic field was responsible for the prodigious ion acceleration observed in the vicinity of

¹It is important to note that we use the term *stochastic* (as defined by Spektor) to refer to “a process in which the trajectories of any two particles initially infinitely close to each other diverge exponentially with time” [10]. The stochastic acceleration referred to in this thesis is *not* the result of random forces. The equations of motion are wholly deterministic.

²As will be demonstrated later in this section, this assertion technically does not apply to the on-resonant case.

the CIF [19]. The single-wave model was thus expanded to include multiple waves. In that same year, Bénisti *et al* demonstrated that ions with arbitrarily low initial velocity can be stochastically accelerated via nonlinear wave-particle interactions if the aforementioned electrostatic spectrum contains at least two waves that satisfy a “beating criterion” such that their frequencies differ by an integer multiple of the cyclotron frequency [33, 34]:

$$\omega_2 - \omega_1 = \alpha \omega_{ci} \quad (2.1)$$

where ω_1 and ω_2 are the wave frequencies, $\omega_{ci} = qB/m$ is the local ion cyclotron frequency, and α is a nonzero integer. They claimed that in the presence of these beating electrostatic waves (BEW), the otherwise separate coherent and stochastic regions of phase space become interconnected, allowing ions with initial energies well below the SEW stochastic threshold to be coherently accelerated into the stochastic region. We will refer to this particular acceleration mechanism – in which ions experience coherent, and then stochastic, motion – as *regular* acceleration.

In 2004, Spektor and Choueiri showed that although the beating criterion is necessary for regular acceleration to occur, it is not sufficient [35]. They found that in order to ensure regular acceleration in the presence of BEW, an ion’s initial Hamiltonian must fall within a certain predefined range. This discovery led to the natural division of BEW phase space into three separate regions: a stochastic region, a forbidden region (populated by “trapped” ions whose Hamiltonians do not fall within the appropriate bounds), and a new regular acceleration region (in which ions are coherently accelerated up to – and through – the stochastic threshold).

In spite of this additional restriction on the Hamiltonian, the nonresonant interactions characteristic of the BEW phenomenon still result in the acceleration of ions with initial velocities much smaller than the phase velocities of the exciting waves. This stands in stark contrast to SEW acceleration, in which only the portion of the ion distribution that satisfies the broadened resonance condition experiences stochastic acceleration. This implies that for a general distribution, a larger portion of ions will satisfy the less stringent BEW acceleration criteria than will satisfy the corresponding SEW resonance condition.

Ion heating via BEW propagation was first demonstrated in a laboratory setting by Spektor and Choueiri in 2005 [36]. In 2009, Jorns and Choueiri were able to unambiguously demonstrate the superiority of BEW heating over SEW heating [37].

They reported a 90% increase in perpendicular ion temperature for BEW heating versus only a 50% increase for SEW heating at comparable wave energy densities. In 2011, Jorns and Choueiri derived an analytical expression that demonstrated the superiority of BEW heating over SEW heating for all parameter space [38]. This claim was also confirmed by their numerical results.

2.3 Analytical and Numerical Formulation

For the sake of clarity (and to qualify the theory discussed in the previous section), we present the SEW and BEW phenomena in an analytical and numerical context. We begin with an expression for the Hamiltonian of a charged particle of mass m and charge q in a uniform z -directed magnetic field subject to a spectrum of perpendicularly propagating electrostatic waves (see Appendix B for a detailed derivation):

$$h = \frac{1}{2m} \left(p_x^2 + q^2 B_0^2 x^2 \right) + \frac{qE_0}{k} \sum_{i=1}^n \cos(kx - \omega_i t) \quad (2.2)$$

where x and p_x are the generalized coordinate and momentum (respectively), B_0 is the magnitude of the field, E_0 is the amplitude of the waves, k is the wave number, and ω_i are the wave frequencies. In (2.2), we have assumed that all waves in the spectrum are of equal amplitude, wave number, and phase in order to simplify our analysis. In the beating wave case, we will assume that $n = 2$ such that ω_1 and ω_2 satisfy Eq. (2.1); in the single wave case, we will of course assume that $n = 1$.

Hamilton's equations reveal that this nonlinear system is analytically intractable in both cases; there is no general closed-form solution. However, because (2.2) is separable, we can use an efficient symplectic integration algorithm to solve Hamilton's equations numerically and generate accurate Poincaré sections of particle motion.³

To gain greater physical insight from these Poincaré plots, we take advantage of the periodicity of the system and express (2.2) in normalized action-angle coordinates. By normalizing lengths to k^{-1} and times to ω_{ci}^{-1} , and by making the appropriate canonical substitutions (see Appendix B for details), the Hamiltonian takes the following form [33]:

³For a discussion of Hamiltonian mechanics and a brief description of the numerical methods used in this thesis, see Appendix A.

$$\overline{\mathcal{H}}_k = \frac{\rho^2}{2} + \varepsilon \sum_{i=1}^n \cos(\rho \sin \theta - \nu_i \tau) \quad (2.3)$$

where ρ is the normalized Larmor radius, θ is the Larmor phase angle, ε is the normalized wave amplitude, ν_i is the normalized frequency, and τ is a normalized time variable ($\tau = \omega_{ci} t$). In the BEW case, the wave frequencies ν_1 and ν_2 satisfy a normalized beating criterion such that $\nu_2 - \nu_1 = \alpha$ where α is a nonzero integer. In the case of a uniform magnetic field, $\rho \propto v_\perp$. Thus, plotting our results in terms of ρ and θ gives us direct physical insight into the acceleration process [10].

2.3.1 Single Electrostatic Wave (SEW) Acceleration

We first examine the case of off-resonant SEW acceleration. In this context, off-resonant implies that ω is not an integer multiple of ω_{ci} ($\nu \notin \mathbb{N}$). As aforementioned, Karney determined that in order for an ion to experience SEW acceleration, the exciting wave amplitude must exceed a certain value, and the ion velocity must fall within a certain range, thereby satisfying a broadened resonance condition. With this knowledge, we can define a domain of parameter space in which SEW acceleration will occur for a given wave. In terms of our normalized parameters, the conditions for SEW acceleration can be expressed as follows [32]:

$$\varepsilon > \frac{\nu^{2/3}}{4} \equiv \varepsilon_{th} \quad (2.4)$$

$$\rho_{th} \equiv \nu - \sqrt{\varepsilon} < \rho < (4\varepsilon\nu)^{2/3}(2/\pi)^{1/3} \equiv \rho_{UB} \quad (2.5)$$

Only if both of these conditions are satisfied will SEW acceleration occur for a given wave-ion pair.

Figure 2.2 features two Poincaré sections intended to illustrate the structure of ion phase space in the presence of SEW. Figure 2.2(a) shows that for $\varepsilon < \varepsilon_{th} \approx 2.1$, ion motion is always coherent, even for $\rho > \rho_{th}$. In Figure 2.2(b), clearly $\varepsilon > \varepsilon_{th}$, and as a result, a stochastic region is clearly visible for $\rho \gtrsim \rho_{th}$. Thus, in the off-resonant SEW case, the coherent and stochastic regions of phase space remain strictly separate. If an ion starts in a given regime, it will remain in said regime for all time.

Figure 2.3 depicts the time evolution of ρ for four test ions of varying initial conditions subject to SEW propagation. The plot reveals that ion motion is clearly

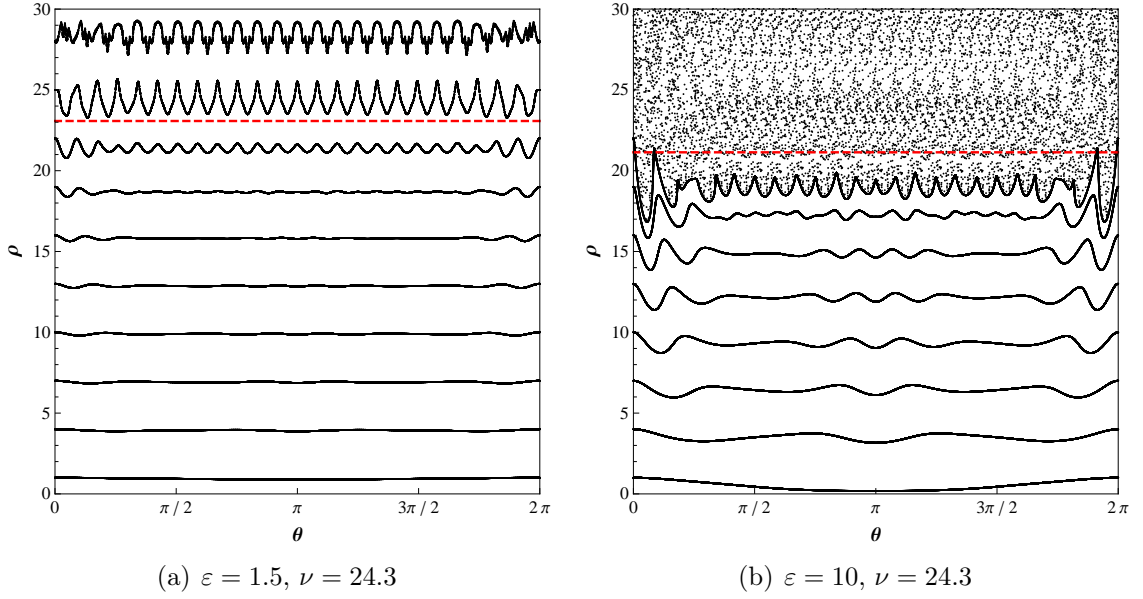


Figure 2.2. Poincaré sections depicting numerical solutions to Hamilton’s equations for $n = 1$ in the off-resonant case. Each section is a projection of ion motion onto the (ρ, θ) plane at a fixed interval τ_c corresponding to the normalized period of the exciting wave ($2\pi/\nu$). Each well-defined curve represents the trajectory of a single test ion in phase space. The dotted red lines represent ρ_{th} as defined in (2.5). In (a), the wave amplitude does not satisfy (2.4). Ion motion is thus coherent for all ρ ; no stochastic region is observed. In (b), (2.4) is clearly satisfied, and ion motion is roughly stochastic for $\rho > \rho_{th}$; otherwise, it is coherent.

coherent outside the upper and lower bounds prescribed by (2.5), even for ρ close to ρ_{th} . For $\rho_0 = 30$, ion motion starts and remains clearly stochastic, and the ion gains net energy from the wave. However, for $\rho_0 = 70$, while the ion clearly falls within the theoretical bounds of the stochastic region, its motion is essentially coherent: ρ varies little and the ion gains no net energy from interacting with the wave. This inconsistency suggests that the expression for ρ_{UB} featured in (2.5) is a poor approximation for the upper bound of the stochastic region, and that the bounds of the chaotic regime in the SEW case warrant further investigation. However, seeing that such an investigation is beyond the scope of this thesis, we simply acknowledge the apparent inconsistency and continue with our discussion.

Next we examine the case of on-resonant SEW acceleration ($\nu \in \mathbb{N}$). The Poincaré section featured in Figure 2.4(b) depicts particle motion in the on-resonant case (the familiar off-resonant case is included in Figure 2.4(a) for reference). For most of the region $\rho < \rho_{th}$, ion motion is coherent and phase trajectories are practically indistinguishable from those of the off-resonant case. However, as ρ approaches the

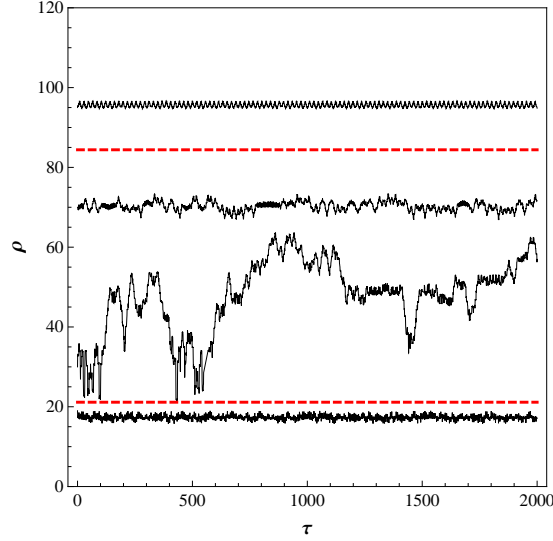


Figure 2.3. Time evolution of ρ in the off-resonant SEW case ($\varepsilon = 10$, $\nu = 24.3$) for various starting orbits (ρ_0). The upper and lower dotted red lines represent ρ_{UB} and ρ_{th} , respectively. For $\rho < \rho_{th}$ and $\rho > \rho_{UB}$, ρ is nearly constant and ion motion is coherent. Stochastic acceleration is clearly observed for $\rho_0 = 30$ ($> \rho_{th}$). However, for $\rho_0 = 70$, which falls well within the theoretical bounds of the stochastic regime, ion motion is roughly coherent.

stochastic threshold ρ_{th} in the on-resonant case, ions begin to exhibit new behavior. The phase plot features an array of hyperbolic points near ρ_{th} , and the impermeable boundary between the coherent and stochastic regions that was observed in the off-resonant case is no longer well-defined.

An examination of the ion trajectories featured in Figure 2.5 gives further insight into the process of on-resonant SEW acceleration. The three coherent test ion trajectories are very similar to the off-resonant trajectories depicted in Figure 2.3. However, for $\rho_0 = 18$, the test ion starts in the coherent regime, is coherently accelerated up to ρ_{th} , and is stochastically accelerated after breaking the threshold. This behavior is markedly different from the off-resonant case, in which ions are confined to either the coherent or stochastic regions for all time. This result implies that in the case of on-resonance, the coherent and stochastic regions of phase space are in fact connected, albeit only for a small range of ρ values close to ρ_{th} . Thus, in the single wave case, a narrow band of regular acceleration is observed in the vicinity of ρ_{th} for $\nu \in \mathbb{N}$.

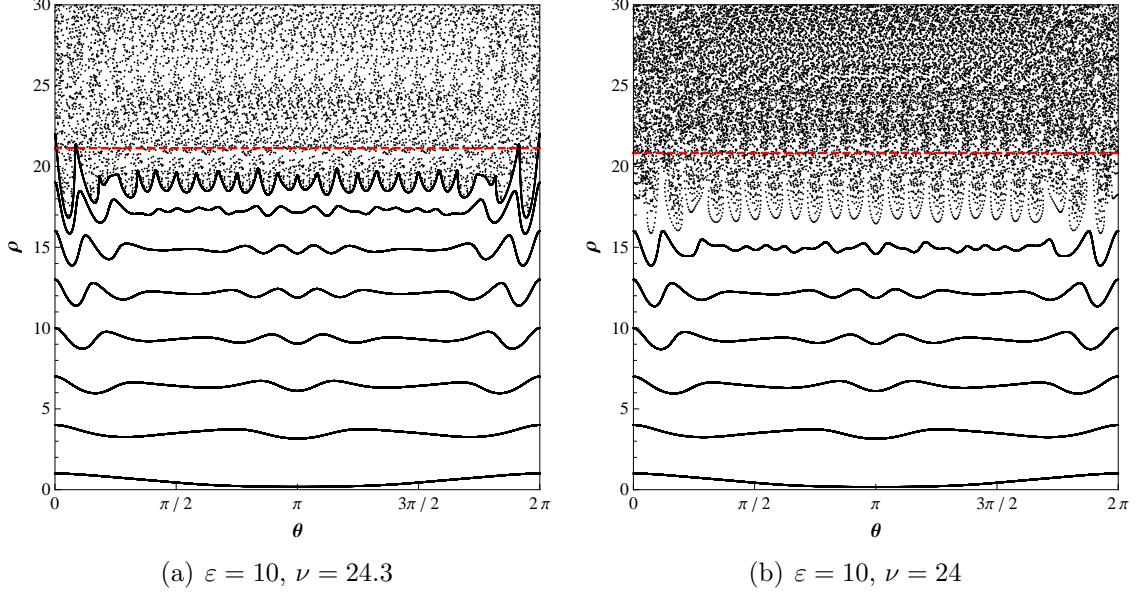


Figure 2.4. Poincaré sections depicting numerical solutions to (2.2) for $n = 1$ in the (a) off-resonant and (b) on-resonant cases. The off-resonant plot is included for the purpose of comparison. The dotted red lines again represent ρ_{th} as defined in (2.5). Note that in the on-resonant case, the section features an array of hyperbolic points below ρ_{th} , about which the coherent region appears to “bleed” into the stochastic regime.

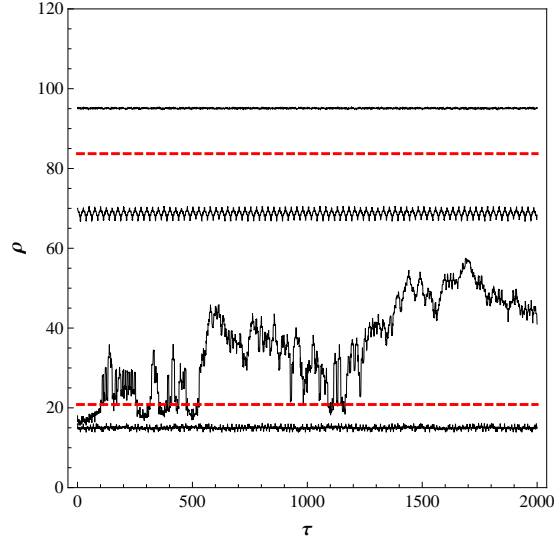


Figure 2.5. Time evolution of ρ in the on-resonant SEW case ($\varepsilon = 10, \nu = 24$) for various starting orbits (ρ_0). The upper and lower dotted red lines again represent ρ_{UB} and ρ_{th} , respectively. For $\rho_0 = 16$ and $\rho_0 = 95$, both of which do not satisfy (2.5), ρ is roughly constant and ion motion is coherent. Coherent motion is also observed for $\rho_0 = 70$, which satisfies (2.5), further suggesting that the upper bound criterion in (2.5) is inaccurate. However, for $\rho_0 = 18$ ($< \rho_{th}$), the test ion clearly starts in the coherent region, but is then coherently accelerated up to the stochastic threshold where it subsequently experiences stochastic acceleration and energization.

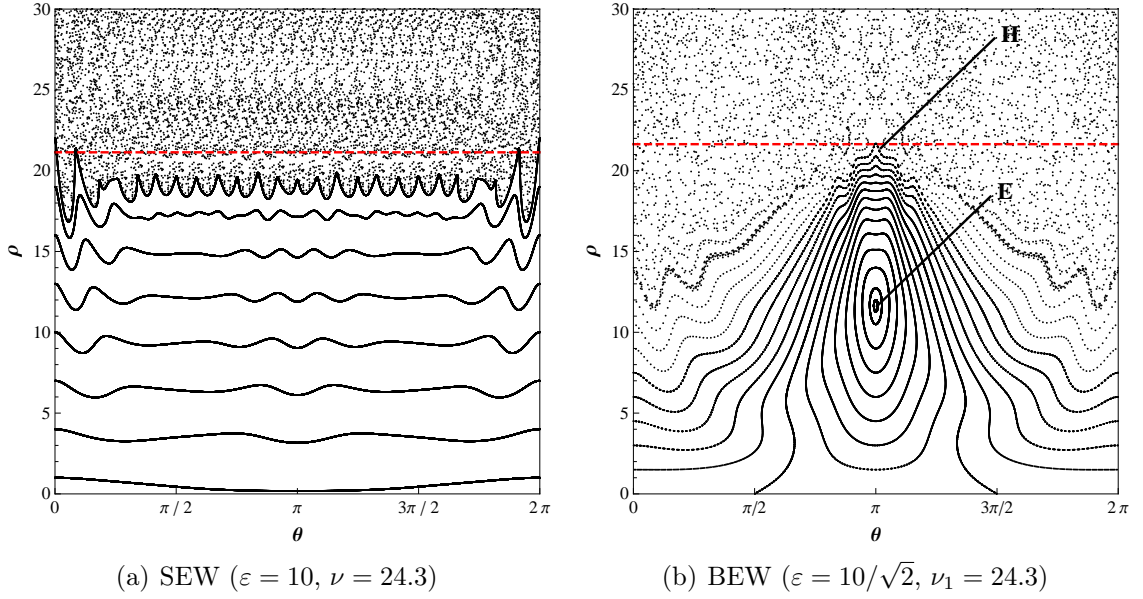


Figure 2.6. Poincaré sections for the off-resonant (a) SEW ($\varepsilon = 10, \nu = 24.3$) and (b) BEW ($\varepsilon = 10/\sqrt{2}, \nu_1 = 24.3$) cases. Normalized amplitudes were chosen such that total wave energy density is equal in both cases. In both plots, the dashed red line represents the single-wave stochastic threshold. In the BEW case, the hyperbolic and elliptic points are labeled **H** and **E**, respectively. In the BEW case, note that the stochastic region extends well below the SEW threshold.

2.3.2 Beating Electrostatic Wave (BEW) Acceleration

Next we consider the case of two off-resonant electrostatic waves that satisfy the beating criterion specified in (2.1). For this discussion – and for the remainder of this thesis – we will assume that the frequencies of these beating waves differ by ω_{ci} (in other words, $\nu_2 - \nu_1 = \alpha = 1$).

Figure 2.6 features two Poincaré sections that illustrate phase space structure in the off-resonant SEW and BEW cases for equal energy densities. For a spectrum of n electrostatic waves, the normalized average energy density u_e is

$$u_e = \sum_{i=1}^n \frac{\varepsilon_i^2}{2} \quad (2.6)$$

Thus, a single electrostatic wave with amplitude ε has the same energy density as two beating electrostatic waves with $\varepsilon_1 = \varepsilon_2 = \varepsilon/\sqrt{2}$. The BEW plot was generated by sampling ρ and θ of ions with varying initial conditions at a fixed time interval τ_c corresponding to the least common period of the beating waves (in this case, $\tau_c = 2\pi / 0.1$).

The BEW Poincaré section has many interesting properties. First, we immediately see that in the BEW case, for a range of θ values, the stochastic region actually extends below the single-wave threshold ρ_{th} . Thus, depending on their phase, ions with $\rho_0 < \rho_{th}$ can actually experience stochastic energization immediately after encountering the exciting waves [10]. Second, we see that contrary to the SEW case, ions subject to BEW can experience appreciable coherent acceleration. This coherent acceleration is observed in one of two forms: either the ion is coherently accelerated up to the stochastic threshold, after which it enters the stochastic region and is subsequently stochastically accelerated, or it is coherently accelerated up to a maximum $\rho_{max} < \rho_{th}$ and then is coherently decelerated. While the first case corresponds to a gradual and subsequently chaotic increase in Larmor radius, the second corresponds to the periodic contraction and expansion of a magnetized ion's orbit about its guiding center.

The physical domains of these two types of coherent motion can be determined by inspection of the critical points of the system. The Poincaré plot features two critical points of motion in phase space: a hyperbolic point \mathbf{H} at $\rho_H \approx \nu - \sqrt{\varepsilon}$ and $\theta_H = \pi$, and an elliptic point \mathbf{E} at $\rho_E \approx (\nu - \sqrt{\varepsilon})/2$ and $\theta_E = \pi$. The locations of these critical points were analytically and numerically confirmed by Spektor and Choueiri [35]. The elliptic point represents a local minimum of $\overline{\mathcal{H}}_k$, and is immediately surrounded by closed orbits in phase space. The hyperbolic point, on the other hand, represents a local maximum of $\overline{\mathcal{H}}_k$. Furthermore, the curve that intersects the hyperbolic point (henceforth referred to as $\rho_s(\theta)$) is clearly a separatrix of the system. Ions with ρ_0 and θ_0 such that $\rho_0 < \rho_s(\theta_0)$ are clearly trapped, and can never experience stochastic energization. These trapped ions can follow one of two trajectories: either they orbit about the elliptic point \mathbf{E} , or they cover the full θ range with ρ never surpassing \mathbf{H} . Ions with $\rho_0 > \rho_s(\theta_0)$, on the other hand, can indeed be stochastically accelerated, and – depending on the precise values of ρ_0 and θ_0 – may or may not be coherently accelerated first. Thus, this separatrix defines the boundary between the regular and forbidden acceleration regions characteristic of BEW phase space. Spektor and Choueiri expressed the domain of the forbidden region in terms of the normalized Hamiltonian as follows [35]:

$$\overline{\mathcal{H}}_k(\mathbf{E}) < \overline{\mathcal{H}}_k(\rho_0, \theta_0) < \overline{\mathcal{H}}_k(\mathbf{H}) \quad (2.7)$$

for $\rho_0 < \rho_{th} = \nu - \sqrt{\varepsilon}$. Figure 2.7 clearly illustrates the three distinct regions of ion acceleration in the BEW case. Note that the boundary between the forbidden

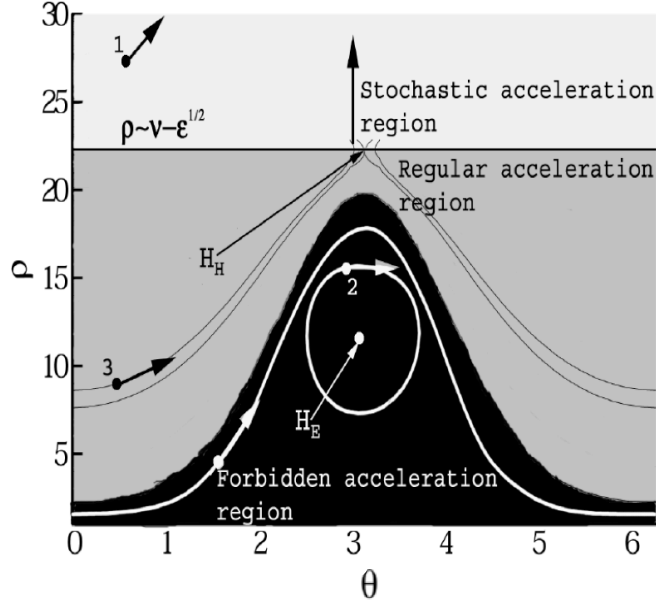


Figure 2.7. Region plot depicting the three distinct domains of BEW acceleration ($\varepsilon = 10$, $\nu_1 = 24.3$) in the ρ - θ plane. Sample ion phase space trajectories are included for clarity. This figure was taken from Ref. [35].

and regular regions is only approximate. Nevertheless, the figure still captures the most important feature of BEW acceleration: an ion with very low initial velocity can be coherently accelerated up to and through the stochastic threshold. Thus, the broadened resonance characteristic of SEW acceleration is clearly not required for BEW acceleration to occur.

Figure 2.8 features the time evolution of ρ and $Y_{GC} - Y_{GC0}$ (the normalized Y -displacement of the guiding center, where $Y = ky$) for three test ions. The black curve represents an ion in the forbidden acceleration region. The ion is coherently accelerated and decelerated periodically as its Larmor radius oscillates between ρ_{th} and some minimum value. The ion's guiding center remains fixed in Y (aside from ignorable fluctuations) for all time. The red curve represents an ion that starts in the stochastic region such that $\rho_0 > \rho_{th}$. The ion experiences appreciable energization as its Larmor radius oscillates stochastically in the region above ρ_{th} . Over time, the guiding center of the ion experiences a net drift in the $\mathbf{k} \times \mathbf{B}$ direction (in this configuration, the negative Y direction). Finally, the blue curve represents an ion that starts in the regular acceleration regime and is coherently accelerated through the stochastic threshold. This curve in particular illustrates the principal benefit of

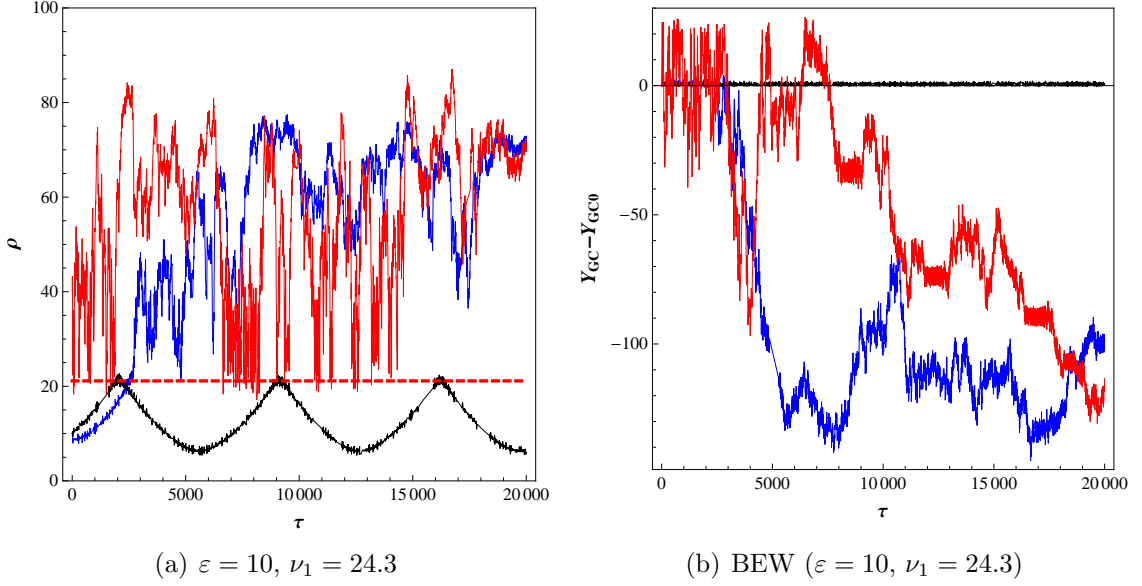


Figure 2.8. Time evolution of (a) ρ and (b) Y_{GC} in the off-resonant BEW case ($\varepsilon = 10$, $\nu_1 = 24.3$) for various initial conditions (ρ_0 and θ_0). The dotted red line represents the SEW stochastic threshold ρ_{th} . Note that stochastic acceleration results in a net displacement of the guiding center in the $\mathbf{k} \times \mathbf{B}$ direction.

BEW over SEW: despite ρ_0 being less than half of ρ_{th} , the stochastic regime is clearly still accessible to the ion. Furthermore, while the ion's guiding center remains fixed during the coherent portion of the acceleration, upon stochastic energization it too experiences a clear negative displacement in Y_{GC} .

Now that the basics of off-resonant BEW acceleration have been effectively characterized, we seek to briefly examine how ion behavior changes with the wave parameters ε and ν . Figure 2.9 features several Poincaré plots that illustrate how the structure of BEW phase space changes with these parameters. We see that as the normalized frequencies ν_1 and ν_2 of the exciting waves decreases, the stochastic threshold decreases linearly (as expected, since $\rho_{th} = \nu - \sqrt{\varepsilon}$), as do the locations of the elliptic and hyperbolic points. However, for very low ν_1 , the BEW phase space structure seems to collapse to the elliptic point and a regular acceleration region is not easy to define (although subsequent numerical investigations of particle trajectories have demonstrated that regular acceleration does indeed occur at these low frequencies). Nevertheless, it is apparent that if we want to increase the overall accessibility of the stochastic regime for a general ion distribution, a viable option is to decrease the normalized frequencies of the exciting waves. However, given that the stochastic

threshold decreases with increasing ν , one expects the upper bound of the stochastic regime ρ_{UB} to decrease as well (as is the case for SEW).⁴

The remaining plots in Figure 2.9 illustrate how BEW phase space changes with increasing wave amplitude ε . We see that as ε increases, the regular acceleration region experiences an appreciable expansion and dips to much lower values of ρ_0 . Since ρ_{th} goes as the negative square root of ε , the stochastic threshold also decreases with increasing amplitude (but inspection of the featured plots reveals that the square root serves to significantly dampen this effect). Furthermore, numerical results have also confirmed that increasing ε greatly decreases the timescale of the acceleration, as one would intuitively expect. Thus, by increasing the normalized amplitude of the exciting waves, we can further increase the accessibility of the stochastic region. The principal difference between increasing ε and decreasing ν is that while the former mainly increases the fraction of ions that start in the regular acceleration region, the latter mainly increases the fraction of ions that start in the stochastic acceleration region.

Note that for certain combinations of ε and ν (such that $\nu - \sqrt{\varepsilon} < 0$) this treatment of BEW acceleration actually predicts a negative value for the stochastic threshold ρ_{th} . Numerical investigations of particle trajectories reveal that in these cases, the stochastic regime essentially expands to fill the entirety of the phase space. However, as will be demonstrated in Chapter 4, consideration of the EIC dispersion relation renders this scenario largely unphysical in the context of a real plasma.

⁴Given the lack of theoretical development in this area, Jorns is currently conducting an analytical investigation to determine an upper bound ρ_{UB} for BEW acceleration.

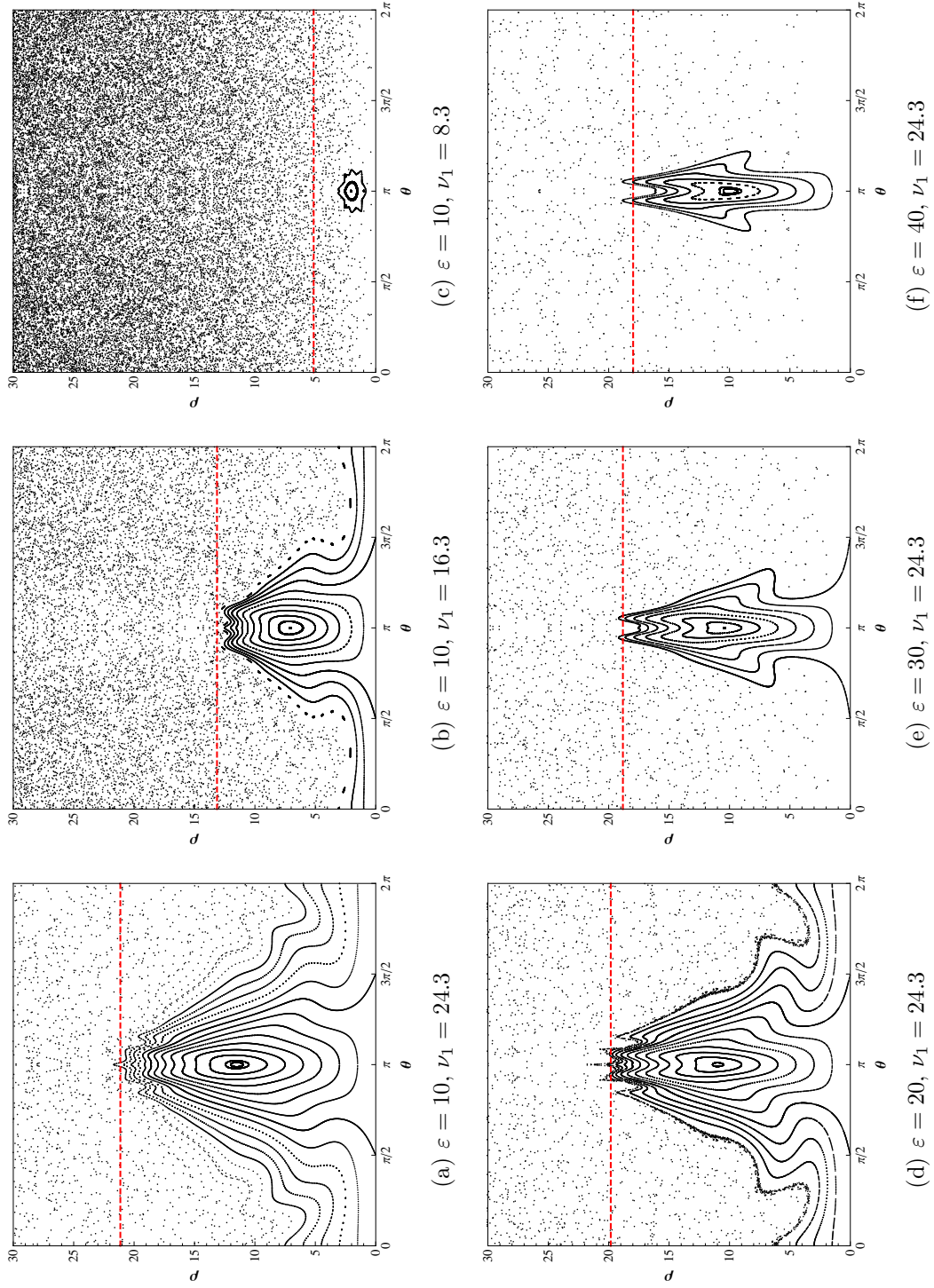


Figure 2.9. Off-resonant BEW Poincaré sections for various normalized amplitude and frequency combinations. As ε increases, the regular acceleration region expands. The stochastic threshold ρ_{th} decreases linearly with ν .

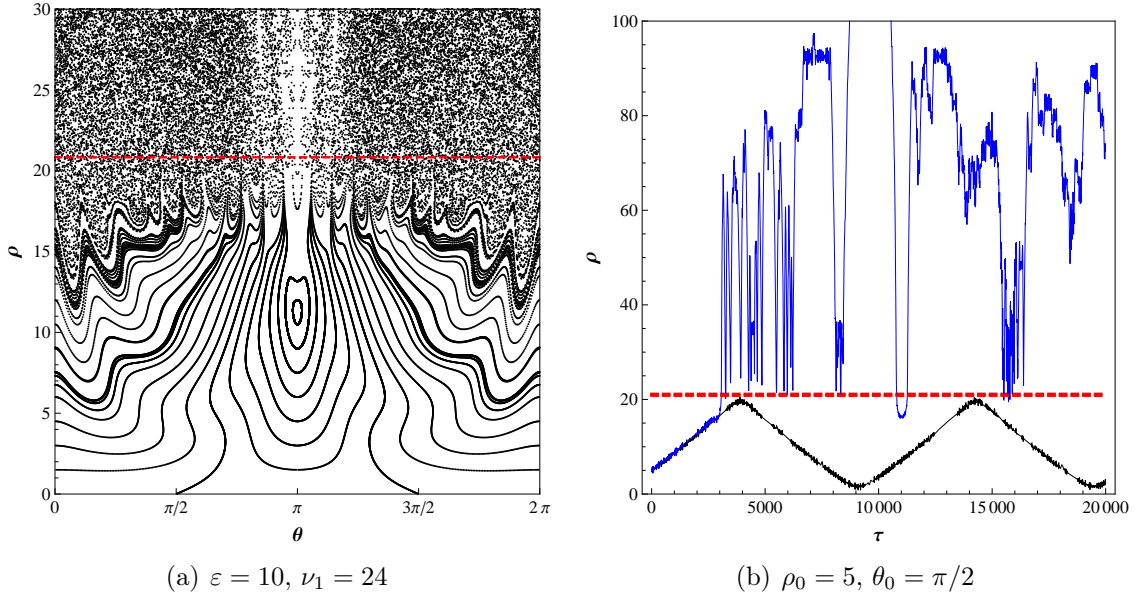


Figure 2.10. (a) Poincaré section depicting the structure of BEW phase space in the on-resonant case. Note the array of hyperbolic points below the stochastic threshold that serve to expand the regime of regular acceleration. (b) Trajectory plot featuring an ion subject to off-resonant ($\nu_1 = 24.3$, black curve) and on-resonant ($\nu_1 = 24$, blue curve) BEW. Initial conditions are identical in both cases. The ion is trapped in the off-resonant case, but in the case of on-resonance, it is regularly accelerated.

To close out our discussion of electrostatic wave acceleration, we consider the case of on-resonant BEW acceleration (see Figure 2.10 for the relevant Poincaré section). Near the stochastic threshold, BEW phase space has a structure similar to the on-resonant SEW case, featuring an array of hyperbolic points just below ρ_{th} . However, we also note that the single hyperbolic point at $\theta = \pi$ that was characteristic of off-resonant BEW acceleration has been replaced by two hyperbolic points that straddle the mirror plane of the section. Thus, we see that many ions in formerly closed trajectories about the elliptic point are no longer trapped (as they were in the off-resonance), and thus can access the stochastic region via one of the two central hyperbolic points. Figure 2.10(b) illustrates the time evolution of ρ for two identical test ions. The black curve represents the off-resonant case, in which the ion is clearly trapped in the forbidden region. The blue curve, however, represents the on-resonant case, in which the same ion (with identical initial conditions) is stochastically accelerated upon reaching ρ_{th} . From the Poincaré section, we also note that no ions span the full θ range without undergoing stochastic energization. In fact, we can conclude from this plot that the only ions that cannot access the stochastic regime are those

in the immediate vicinity of the elliptic point (see the closed orbits in the 2.10(a)). Thus, in the on-resonant case, while the forbidden region essentially collapses to the elliptic point, the regular acceleration region expands to fill the majority of phase space beneath ρ_{th} .

2.4 Propulsive Applications

As aforementioned, Jorns and Choueiri have demonstrated both analytically and experimentally that BEW propagation is a comparatively efficient method for heating a plasma. Thus, the BEW phenomenon clearly has potential applications in the heating stage of an electrothermal thruster.

In this thesis, however, we seek to demonstrate the feasibility of a propulsion concept that exploits the direct acceleration of individual ions via BEW (as opposed to ensemble heating and subsequent expansion through a suitable nozzle). As we demonstrated in the previous section, the physical manifestation of BEW acceleration is an increase in the Larmor radius of the ion. In the next chapter, we introduce the fundamentals of the Beating Wave Thruster concept – a propulsion mechanism that exploits ion precession by using a steeply-sloped magnetic field to convert gyro-motion to linear motion. By introducing beating waves into the system, we hope to convert the radial BEW acceleration observed in the uniform field case into linear ion acceleration in the sloped field case, thereby enhancing the overall performance and efficiency of the thruster. Furthermore, we also hope that the stochastic drift of the guiding center in the $\mathbf{k} \times \mathbf{B}$ direction will help to minimize wall losses in the context of an actual thruster geometry. And finally, since the properties of BEW acceleration clearly change with the variation of wave parameters, we expect BWT performance characteristics to change in a related fashion, thereby implying thruster variability.

Chapter 3

Beating Wave Thruster (BWT) Concept

In this chapter, we formally introduce the Beating Wave Thruster (BWT) concept and review and expand upon the foundational work conducted by Jorns and Choueiri in 2010 [1]. We begin with a discussion of magnetic field topography, followed by a mathematical description of the single-ion problem in the context of Hamiltonian mechanics. We continue with a detailed description of single-ion dynamics in the absence of BEW (the “unperturbed” case) and extend our initial analysis to a thermalized ensemble of ions via numerical simulation. We conclude with a brief introduction to the corresponding “perturbed” case, which comprises the bulk of the following chapter.

3.1 Magnetic Field Topography

In 2010, Jorns and Choueiri proposed a thruster concept that uses beating electrostatic waves to directly accelerate ions within a magnetized plasma [1]. Critical to the success of this configuration is the topology of the applied magnetic field within the confines of the thruster. A rectilinear, z -oriented field was chosen for this particular application, with a magnetic null at $y = 0$, a steep positive slope for $|y| < \delta$, and constant $|\mathbf{B}|$ for $|y| > \delta$. In vector notation,

$$\mathbf{B} = B_0 f(y) \hat{z} \tag{3.1}$$

where

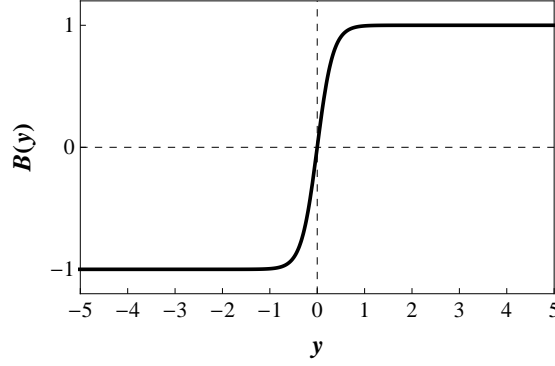


Figure 3.1. Magnetic field configuration as described by Eq. 3.5 for $B_0 = \delta = 1$. Note that the field is (approximately) homogeneous for $|y| > \delta$.

$$f(y) = \begin{cases} -1 & \text{if } y < -\delta \\ 1 & \text{if } y > \delta \\ 0 & \text{if } y = 0 \end{cases} \quad (3.2)$$

and

$$f'(y) > 0 \quad \text{if } -\delta \leq y \leq \delta \quad (3.3)$$

The hyperbolic tangent function exhibits these properties when scaled by the appropriate factors:

$$f(y) = \tanh \frac{3y}{\delta} \quad (3.4)$$

Substitution of this test function into (3.1) yields the following expression for the ideal applied magnetic field within the bounds of the thruster (see Figure 3.1):

$$\mathbf{B} = B_0 \tanh \frac{3y}{\delta} \hat{z} \quad (3.5)$$

For all subsequent analytical and numerical calculations, we will assume that the applied magnetic field is defined by (3.5) unless otherwise noted. We will also assume a two-dimensional geometry (i.e. the magnetic field lines extend to $\pm\infty$ in the z -direction).

The hyperbolic tangent function is an advantageous field representation for a number of reasons. Aside from satisfying the prescribed conditions, (3.5) also maintains a degree of physical fidelity in that it has continuous derivatives. Furthermore, the fact

that the field is defined by a single function over the entire domain (as opposed to a set of piecewise functions) greatly simplifies our analysis by eliminating the need to consider and treat separate subdomains of y . Lastly, this configuration can be very nearly approximated with a clever configuration of current loops, making it fairly easy to reproduce in the laboratory (see Chapter 5 for a more detailed description).

The antisymmetric field configuration depicted in 3.1 and described by (3.5) is intended to exploit the gyromotion of ions in the vicinity of the magnetic null. For now, let us consider only the unperturbed case in which no electrostatic waves are present. Ions that start in the homogeneous regions ($y > |\delta|$) will clearly begin to trace out simple Larmor trajectories. However, as ions approach the sloped region and begin to encounter B-field asymmetry, their trajectories become much more complex. Once an ion crosses the null, the direction of the Lorentz force is reversed, resulting in mirrored orbits that propagate along $y = 0$. In general, any ion whose trajectory crosses $y = 0$ will experience a net guiding center drift along the x -axis, while any ion whose trajectory enters the sloped region but does not cross $y = 0$ will experience a net ∇B drift in the $-x$ -direction while remaining trapped on one side of the null. Jorns and Choueiri posited that for a thermalized distribution of ions, this sloped configuration would yield a net ion current in the $+x$ -direction (and therefore, net thrust in the $-x$ -direction) along the magnetic null, and proposed the introduction of BEW as a means of effectively augmenting that current [1].

3.2 Hamiltonian Formulation

We begin our analysis by considering the single-ion problem. For a magnetized ion of mass m and charge q subject to a spectrum of n perpendicularly propagating electrostatic waves, the Hamiltonian takes the following form (see Appendix B):

$$h = \frac{1}{2m}(\mathbf{p} - q\mathbf{A})^2 + \frac{qE_0}{k} \sum_{i=1}^n \cos(kx - \omega_i t) \quad (3.6)$$

where \mathbf{p} is the canonical momentum vector, \mathbf{A} is the magnetic vector potential (such that $\nabla \times \mathbf{A} = \mathbf{B}$), and all wave parameters are defined as in Chapter 2. For simplicity, we have again assumed that all exciting waves are of equal amplitude, wave number, and phase. In the case of BEW ($n = 2$) and a z -directed, y -dependent magnetic field as in (3.5), the Hamiltonian can be restricted to the following form without loss of

generality (see Appendix B):

$$h = \frac{1}{2m} \left([p_x - qA_x(y)]^2 + p_y^2 \right) + \frac{qE_0}{k} \sum_{i=1}^2 \cos(kx - \omega_i t) \quad (3.7)$$

where wave frequencies ω_1 and ω_2 satisfy the beating criterion in (2.1) for $\alpha = 1$.

Next we nondimensionalize h via canonical transformation. After normalizing length to k^{-1} and time to ω_{ci}^{-1} , we obtain the k -normalized Hamiltonian:

$$\mathcal{H}_k = \frac{1}{2} \left([P_X - \bar{A}_X]^2 + P_Y^2 \right) + \varepsilon \sum_{i=1}^2 \cos(X - \nu_i \tau) \quad (3.8)$$

where

$$\begin{aligned} \mathcal{H}_k &= \frac{k^2}{m\omega_{ci}^2} h & \tau &= \omega_{ci} t & \nu_i &= \frac{\omega_i}{\omega_{ci}} & \varepsilon &= \frac{qkE_0}{m\omega_{ci}^2} \\ X &= kx & Y &= ky & \bar{A}_X &= \frac{qk}{m\omega_{ci}} A_x(Y/k) \end{aligned}$$

$$P_X = X' + \bar{A}_X \quad P_Y = Y' + \bar{A}_Y \quad \nu_1 = \nu \quad \nu_2 = \nu + 1$$

and the prime ($'$) denotes differentiation with respect to the normalized time variable τ . This matches the Hamiltonian derived by Jorns and Choueiri [1]. Expressing the Hamiltonian in this way generalizes our analysis by eliminating the need to specify values for k and ω_{ci} when studying ion trajectories.

The magnetic slope configuration described by (3.5) can also be expressed in k -normalized coordinates:

$$\mathbf{B} = B_0 \tanh \frac{3Y}{\bar{\delta}} \hat{z} \quad (3.9)$$

where $\bar{\delta} = k\delta$. The normalized magnetic vector potential is thus

$$\bar{A}_X = -\frac{\bar{\delta}}{3} \ln \left(\cosh \frac{3Y}{\bar{\delta}} \right) \quad (3.10)$$

Since \mathcal{H}_k was obtained via canonical transformation, the general form of Hamilton's equations remains unchanged:

$$P'_X = -\frac{\partial \mathcal{H}_k}{\partial X} \quad P'_Y = -\frac{\partial \mathcal{H}_k}{\partial Y} \quad X' = \frac{\partial \mathcal{H}_k}{\partial P_X} \quad Y' = \frac{\partial \mathcal{H}_k}{\partial P_Y} \quad (3.11)$$

This system of nonlinear differential equations is the culmination of the single-ion problem we sought to characterize at the start of this section. While it is analytically intractable, it can be solved using numerical methods (provided that the appropriate initial conditions are specified in advance).

3.3 Unperturbed Ion Trajectories ($\varepsilon = 0$)

In this section, we consider single-ion dynamics for $\varepsilon = 0$. The simplified Hamiltonian is

$$\mathcal{H}_k = \frac{1}{2} \left([P_X - \bar{A}_X]^2 + P_Y^2 \right) \quad (3.12)$$

Following the convention of Jorns and Choueiri [1], since \mathcal{H}_k and P_X are clearly constants of motion, we can express the Hamiltonian in terms of P_Y and an effective potential V_{eff} such that

$$V_{eff} = \frac{1}{2} \left([P_X - \bar{A}_X]^2 \right) \quad (3.13)$$

V_{eff} takes two forms depending upon the sign of P_X . For $P_X > 0$, the effective potential is a single well symmetric about $Y = 0$. For $P_X < 0$, V_{eff} becomes a symmetric double well with minima on the Y -axis and a local maximum at $Y = 0$ (see Figure 3.2).

The structure of this potential defines ion behavior in the unperturbed case. Jorns and Choueiri were able to classify particle trajectories based upon the sign of P_X and the value of the Hamiltonian \mathcal{H}_k for a given ion [1]. Their conclusions are summarized in the sections to follow. Subsequent analysis assumes $\bar{\delta} = 1$ unless otherwise noted.

$P_X > 0$

For an ion with $P_X > 0$, the effective potential is a symmetric single well with a minimum at $Y = 0$. Furthermore, for such an ion, the Hamiltonian must clearly satisfy the constraint $\mathcal{H}_k \geq V_{eff}(Y_0)$, where Y_0 is the initial Y -coordinate of the ion.

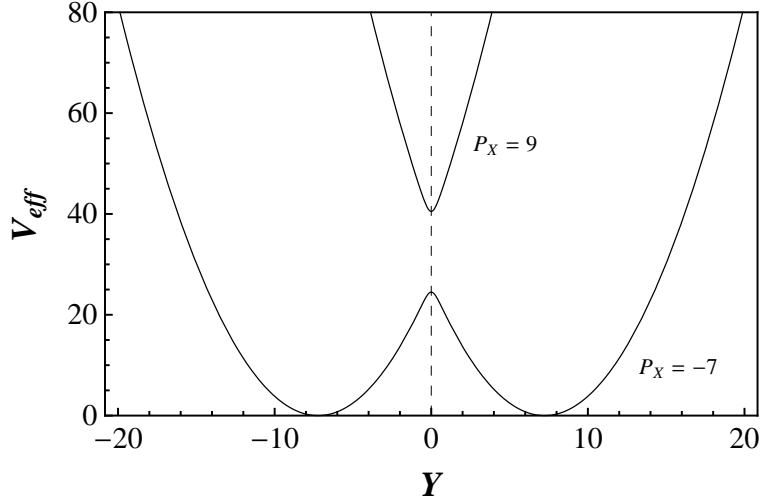


Figure 3.2. Plot of V_{eff} ($\bar{\delta} = 1$) for $P_X = 9$ and $P_X = -7$. Note the single well behavior for $P_X > 0$ and the double well behavior for $P_X < 0$.

The absolute minimum value of \mathcal{H}_k is the minimum of the effective potential itself: $V_{eff}(0) = P_X^2/2$. However, the Hamiltonian can only take on this value when $Y_0 = 0$

All ions with $P_X > 0$ are trapped in this single well. The Y -bounds of their trajectories (and thus, the turning points) are given by $V_{eff}(Y) = \mathcal{H}_k$. However, while for a uniform B-field this would imply simple Larmor precession, in the case of an antisymmetric magnetic slope configuration, this trapping results in mirrored orbits that propagate along the magnetic null in the $+x$ -direction (see Figure 3.3). Thus, for $P_X > 0$, ions will always exhibit forward-drifting trajectories. We will refer to these trajectories as “linear betatron” (or LB) orbits as per the nomenclature of Jorns and Choueiri [1].

$P_X < 0$

For $P_X < 0$, V_{eff} becomes a symmetric double well with minima on the Y -axis and a maximum at $Y = 0$. The magnitude of the maximum is precisely the magnitude of the minimum in the $P_X > 0$ case: $V_{eff}(0) = P_X^2/2$. Differentiation of (3.13) reveals that the minima occur at

$$Y = \pm \frac{\bar{\delta}}{3} \cosh^{-1} \left(e^{-3P_X/\bar{\delta}} \right) \quad (3.14)$$

Just as in the $P_X > 0$ case, the Hamiltonian of an ion with $P_X < 0$ must satisfy the

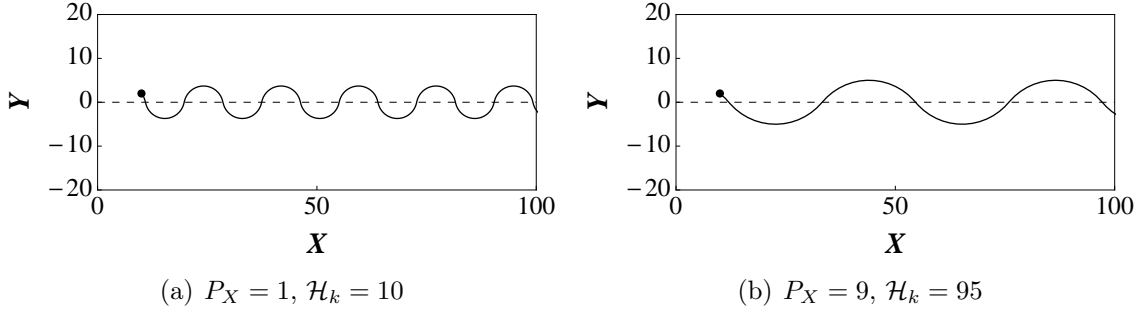


Figure 3.3. Sample ion trajectories for $P_X > 0$. A black dot is used to show the ion's initial position in each plot. In the LB case, the guiding center of ion motion generally lies across the magnetic null in the region of opposite field polarity. Thus, an ion will never complete more than half of a circular orbit before crossing $Y = 0$. As a result, Y is clearly single-valued in X for LB trajectories.

constraint $\mathcal{H}_k \geq V_{eff}(Y_0)$. As we consider ion behavior for different values of \mathcal{H}_k , we will assume that this condition is satisfied.

Let us consider the case where $P_X = -7$ and the Hamiltonian \mathcal{H}_k is small (see I in Figure 3.4). In this case, the ion is clearly trapped in a symmetric well about one of the minima, and exhibits Larmor precession due to the homogeneity of the magnetic field in that region (see trajectory I in Figure 3.5). The length of the \mathcal{H}_k segment that intersects the V_{eff} curve in Figure 3.4 is equal to twice the gyroradius of the ion. These trajectories will be referred to as Larmor orbits. It is important to note that this Larmor orbit classification is generalizable only to ions with $P_X < \bar{A}_X(\bar{\delta}) \approx -0.77$. If P_X does not satisfy this criterion, the minima of the double well fall within the sloped region and our analysis is no longer general (pure Larmor precession is clearly not attainable in the region $|Y| < \bar{\delta}$).

As the value of \mathcal{H}_k increases, Larmor precession persists (and the Larmor radius increases) until the ion begins to experience asymmetry about the minimum of the well (see II in Figure 3.4). This asymmetry serves to perturb the gyromotion of the particle. Physically, this corresponds to the ion just entering the magnetic slope region ($Y < |\bar{\delta}|$). Thus, for $V_{eff}(\bar{\delta}) < \mathcal{H}_k < V_{eff}(0)$, the ion experiences a grad-B drift in its guiding center in the $-x$ -direction, but still does not cross the magnetic null (see trajectory II in Figure 3.5). These trajectories will be referred to as grad-B (or ∇B) orbits.

For $\mathcal{H}_k > V_{eff}(0)$, the ion has enough energy to overcome the potential barrier at $Y = 0$ and actually cross the magnetic null (see III in Figure 3.4). For sufficiently low

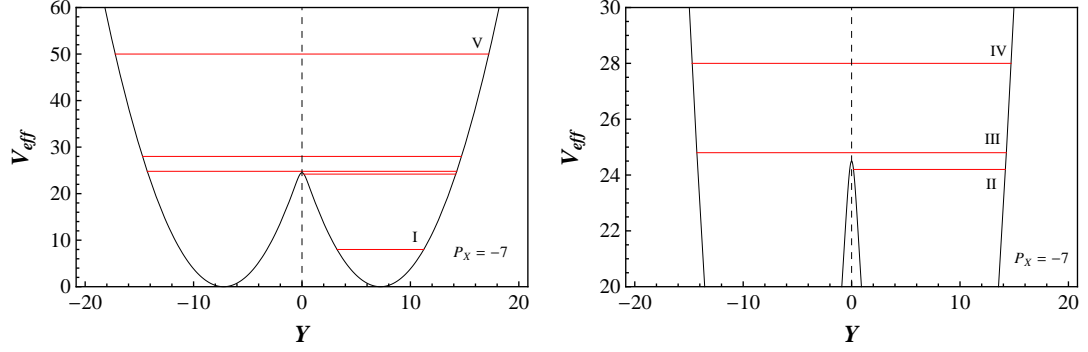


Figure 3.4. V_{eff} plot for $P_X = -7$. A magnified portion of the same plot is included for clarity. Red lines denote values of \mathcal{H}_k for five test ions. Each line matches up with a corresponding particle trajectory (labeled I-V) featured in Figure 3.5 below. A particle encounters a turning point (Y -bound) in its orbit whenever its corresponding \mathcal{H}_k line intersects the V_{eff} curve.

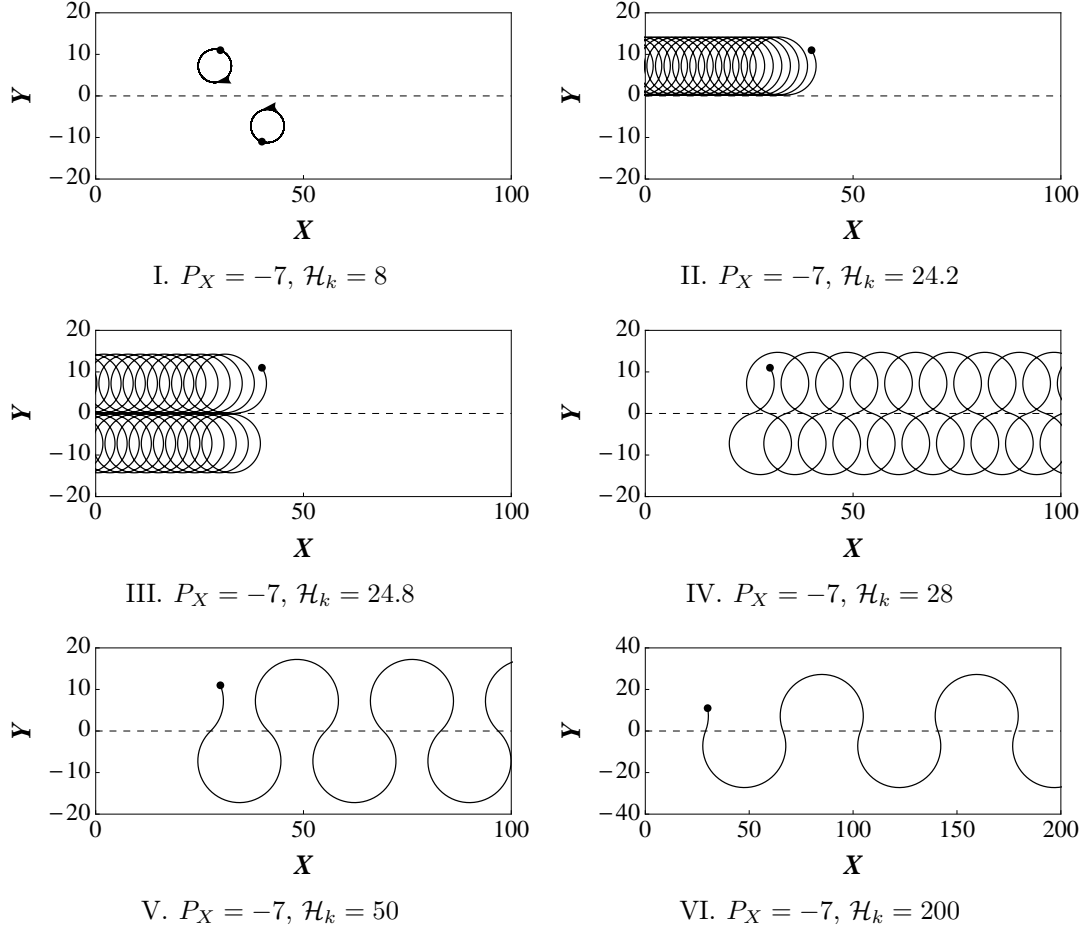


Figure 3.5. Characteristic ion trajectories for $P_X < 0$. Each trajectory (except VI) matches up with a corresponding \mathcal{H}_k value depicted in Figure 3.4.

values of \mathcal{H}_k , the ion follows a “figure-8” trajectory and experiences a net drift in the $-x$ -direction (see trajectory III in Figure 3.5). These will be referred to as reverse figure-8 orbits.

Jorns and Choueiri postulated a range in which these reverse figure-8 trajectories are observed: $V_{eff}(0) = \frac{1}{2}P_X^2 < \mathcal{H}_k < \frac{1}{2}(P_X - \bar{A}_X(\bar{\delta}) - \alpha\bar{\delta})^2$, where α is a scaling parameter.¹ By numerical methods, they determined that α was approximately 0.5 [1]. This value, however, is unphysical, and therefore incorrect. In order for the above inequality to have meaning in general, clearly $-\bar{A}_X(\bar{\delta}) - \alpha\bar{\delta}$ must be less than zero (since P_X is assumed negative). In other words, $\alpha > \frac{1}{3} \ln(\cosh 3) \approx 0.77$. Thus, for $\alpha \approx 0.5$, the aforementioned inequality cannot be satisfied for all P_X (the lower bound is actually greater than the upper bound for $P_X \lesssim -0.135$). Further numerical analysis returned a more appropriate value of $\alpha \approx 0.86$, which both exceeds the specified minimum and also agrees well with computed ion trajectories for several values of $\bar{\delta}$.

For $\mathcal{H}_k > \frac{1}{2}(P_X - \bar{A}_X(\bar{\delta}) - \alpha\bar{\delta})^2$, ions continue to trace out figure-8 trajectories, but experience a net drift in the $+x$ -direction (see IV in Figures 3.4 and 3.5). These will be referred to as forward figure-8 orbits. As \mathcal{H}_k is further increased, the figure-8 trajectories are stretched in X (and Y , but to a lesser extent) and ion motion converges to the linear betatron orbits observed in the $P_X > 0$ case (see trajectory VI in Figure 3.5).

3.4 Orbit Domain Representations

This completes our classification of characteristic ion orbits in the unperturbed case. The regions of phase space occupied by each trajectory are depicted graphically in Figure 3.6. Forward-drifting orbits (both forward figure-8 and LB trajectories) occupy an appreciable fraction of phase space compared to backward-drifting orbits (both grad-B and reverse figure-8 trajectories), thereby verifying the potential of this field configuration to produce a net linear ion current in the $+X$ -direction. However, the Larmor region appears massive as well – its boundary extends to negative infinity in P_X . Thus, in order to be able to intuit the overall behavior of an ion ensemble, it is necessary to recast orbit domains (and thus Figure 3.6) in terms of physical variables

¹Note that this α is not related to the nonzero integer α featured in the expression for the BEW criterion.

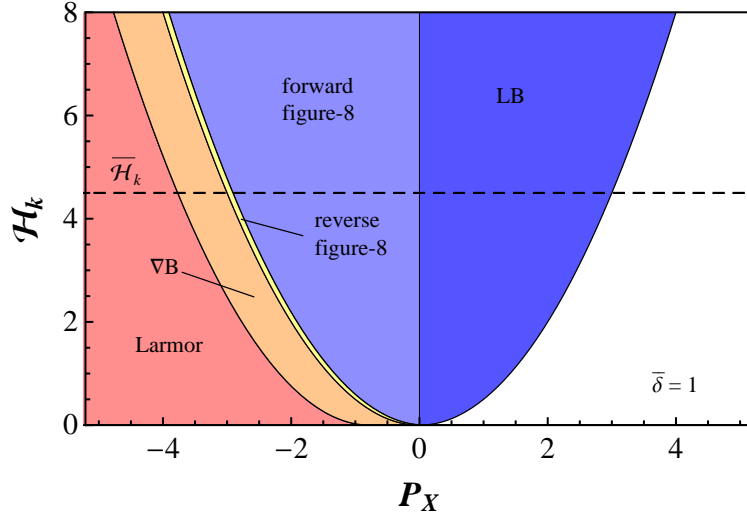


Figure 3.6. Trajectory classification plot depicting the domains of characteristic ion orbits in the P_X - \mathcal{H}_k plane. The white region is implicitly inaccessible to ions due to the inherent structure of the phase space.

– namely, the normalized Larmor radius ρ of the ion and the Y -position of its guiding center Y_{GC} .

We borrow from the procedure of Jorns and Choueiri to determine \mathcal{H}_k and P_X in terms of ρ and Y_{GC} [1]. We begin by expanding ion motion about the guiding center (X_{GC}, Y_{GC}) :

$$X = X_{GC} - \frac{B}{B_0} Y' \quad (3.15)$$

$$Y = Y_{GC} + \frac{B}{B_0} X' \quad (3.16)$$

While the quantity B/B_0 is clearly Y -dependent, we assume that the ion is in the positive homogeneous region ($Y > \overline{\delta}$), and therefore that B/B_0 is equal to positive one. As a consequence of this assumption, our final expression for Y_{GC} will not apply for ions whose trajectories and guiding centers are bounded by $|Y| < \overline{\delta}$. The antisymmetric nature of the problem allows us to consider only this positive domain without loss of generality.

By rearranging (3.16) and exploiting Hamilton's equations, we obtain

$$Y_{GC} = Y - X' = Y - P_X + \overline{A}_X \quad (3.17)$$

Recall that the normalized vector potential \bar{A}_X takes the following form:

$$\bar{A}_X = -\frac{\bar{\delta}}{3} \ln \left(\cosh \frac{3Y}{\bar{\delta}} \right) \quad (3.10)$$

However, as a result of our initial assumption $Y > \bar{\delta}$, the negative exponential in the cosh term is negligible, and the logarithm can be approximated as follows:

$$\ln \left(\cosh \frac{3Y}{\bar{\delta}} \right) \approx \ln \left(\frac{1}{2} e^{3Y/\bar{\delta}} \right) = \frac{3Y}{\bar{\delta}} - \ln 2$$

Combining this result with 3.10 and 3.17 yields a final expression for P_X that depends only on Y_{GC} (since $\bar{\delta}$ is fixed for a given slope configuration):

$$P_X = \frac{\bar{\delta}}{3} \ln 2 - Y_{GC} \quad (3.18)$$

Note that if we wanted to find an expression for P_X in terms of Y_{GC} for $Y < -\bar{\delta}$, we need only reverse the sign of Y_{GC} in (3.18).

Next we seek an expression that relates \mathcal{H}_k and ρ . Again for $Y > \bar{\delta}$, we can express (3.15) and (3.16) in terms of the gyroradius ρ and the cyclotron phase angle θ (measured clockwise from the $\mathbf{B} \times \mathbf{k}$ direction):

$$X = X_{GC} + \rho \sin \theta \quad (3.19)$$

$$Y = Y_{GC} + \rho \cos \theta \quad (3.20)$$

where it follows from (3.15) and (3.16) that $\rho^2 = X'^2 + Y'^2$.

We know from our definitions of generalized momenta that the unperturbed Hamiltonian can be expressed as $\mathcal{H}_k = \frac{1}{2}(X'^2 + Y'^2)$. Thus,

$$\mathcal{H}_k = \frac{\rho^2}{2} \quad (3.21)$$

We have thus determined \mathcal{H}_k and P_X in terms of ρ and Y_{GC} for $Y > \bar{\delta}$. Next we map the orbit domains featured in Figure 3.6 from P_X - \mathcal{H}_k phase space to the Y_{GC} - ρ plane.

First, due to our initial assumption that $Y > \bar{\delta}$, we define the region in which our orbit classifications are not valid:

$$\rho < \bar{\delta} - |Y_{GC}| \quad (3.22)$$

In this domain, both the physical ion trajectory and the guiding center of the ion fall within the bounds of the magnetic slope. Thus, our results are not generalizable to this region, and precise ion orbits are undetermined. This area is represented by the brown triangle in Figure 3.7.

The orbit domains are defined in terms of ρ and Y_{GC} as follows:

Larmor	$\bar{\delta} - Y_{GC} < \rho < Y_{GC} - \frac{\bar{\delta}}{3} \ln(2 \cosh 3)$
∇B	$Y_{GC} - \frac{\bar{\delta}}{3} \ln(2 \cosh 3) < \rho < Y_{GC} - \frac{\bar{\delta}}{3} \ln 2$
reverse figure-8	$Y_{GC} - \frac{\bar{\delta}}{3} \ln 2 < \rho < Y_{GC} - \frac{\bar{\delta}}{3} \ln(2 \cosh 3) + \alpha \bar{\delta}$
forward figure-8	$\rho > Y_{GC} - \frac{\bar{\delta}}{3} \ln(2 \cosh 3) + \alpha \bar{\delta} \quad (\text{for } Y_{GC} > \frac{\bar{\delta}}{3} \ln 2)$
LB	$\rho > \frac{\bar{\delta}}{3} \ln 2 - Y_{GC} \quad (\text{for } Y_{GC} < \frac{\bar{\delta}}{3} \ln 2)$

Finally, we introduce a physical boundary in the form of thruster walls and consider only particles whose trajectories fall within the region $|Y| < L$, where L is the Y -distance from the wall to the magnetic null. Clearly, for $Y > \bar{\delta}$, an ion must meet the following condition in order to avoid collision with the wall:

$$\rho < L - Y_{GC} \quad (3.23)$$

This completes our description of orbit domains in Y_{GC} - ρ space for the case of $Y > \bar{\delta}$. These domains are depicted graphically in Figure 3.7(a).

It is clear from the antisymmetry of the problem that the trajectory domain plot for $Y < -\bar{\delta}$ is simply the reflection of Figure 3.7(a) over Y_{GC} (see Figure 3.7(b)). The union of these reflected figures yields the final orbit classification plot for $|Y| > \bar{\delta}$ featured in Figure 3.7(c).

Note that these ρ versus Y_{GC} plots do not agree with the plots of Jorns and Choueiri [1]. Their plots featured a wall cutoff of $\rho < L - |Y_{GC}|$ over the entire Y_{GC} domain. However, this boundary condition is not appropriate due to the nature of LB orbits. Consider an ion following an LB trajectory in the region above the magnetic null ($Y > 0$). Such an ion can clearly possess an arbitrarily large ρ and an arbitrarily large negative Y_{GC} as long as the two values satisfy the following compound inequality: $\frac{\bar{\delta}}{3} \ln 2 - Y_{GC} < \rho < L - Y_{GC}$. Thus, the magnitudes of the guiding center and Larmor

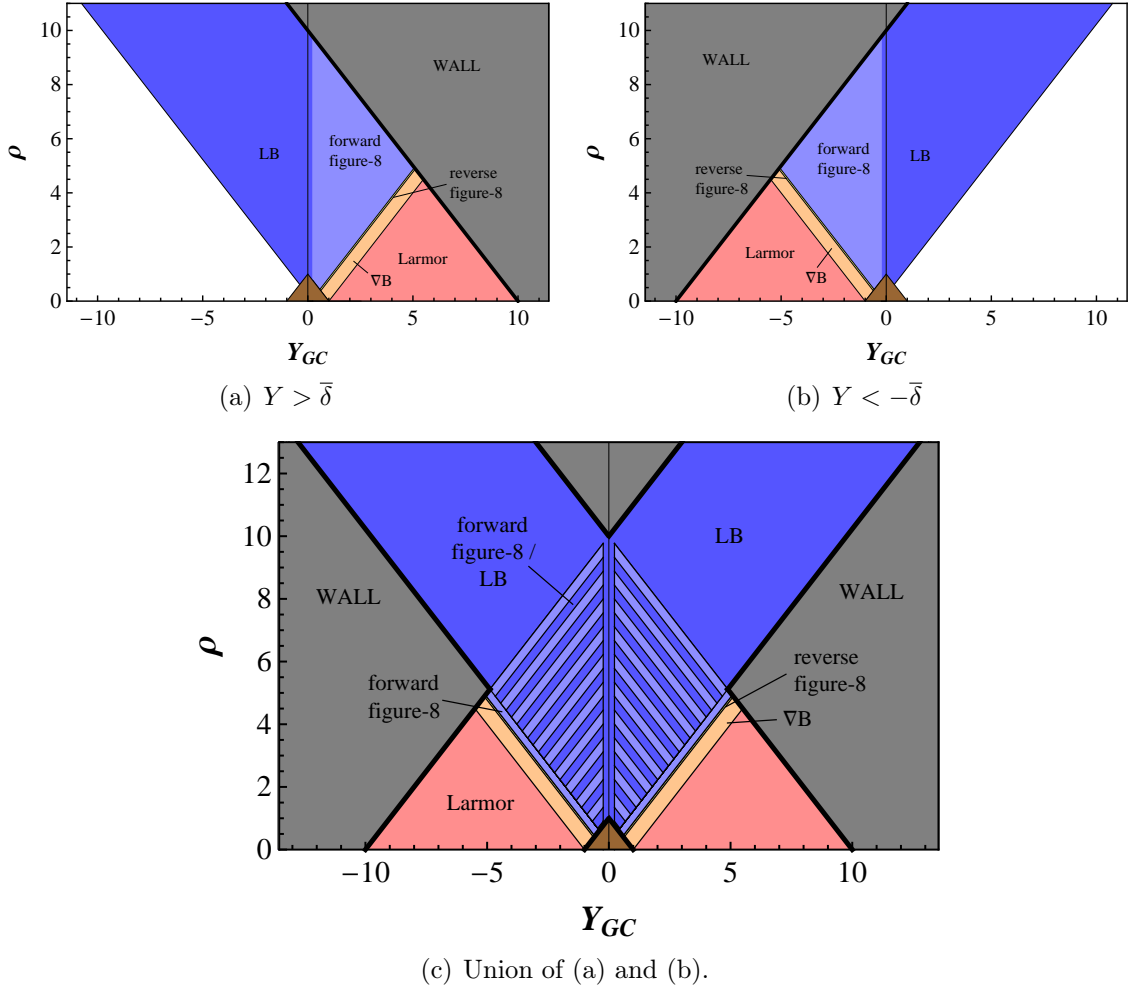


Figure 3.7. Region plots depicting characteristic orbit domains in Y_{GC} - ρ space. (a) and (b) were derived under the specified restrictions on Y . (c) is the complete trajectory classification plot for $|Y| > \bar{\delta}$. The brown region is indeterminate by our analysis, and the gray regions are inaccessible due to the presence of physical walls. For all plots, $\bar{\delta} = 1$ and $L = 10$.

radius may be much larger than L for a LB ion. As long as the aforementioned inequality is satisfied, the ion's physical trajectory will indeed fall within the region of allowable motion ($0 < Y < L$). Also note that while our guiding center analysis was conducted assuming that $Y > \bar{\delta}$, numerical results imply that the previous assertion is also generalizable to LB ions whose trajectories are bounded by $|Y| < \bar{\delta}$. These bounded LB ions tend to be the most “efficient” contributors to the linear ion current as nearly all of their kinetic energy is X -directed ($\mathcal{H}_k \approx X'^2/2$).

Figure 3.7 illustrates how ion orbit domains change with $\bar{\delta}$ for fixed L . As $\bar{\delta} \rightarrow 0$, the B-field approaches a Heaviside step function in Y and the magnetic slope region essentially disappears. As a result, ∇B and reverse figure-8 domains vanish, leaving only Larmor, forward figure-8, and LB trajectories accessible to ions. As we increase the value of $\bar{\delta}$ (for fixed L), we observe that while the domain of the Larmor region shrinks, the grad-B and reverse figure-8 regions expand appreciably in both phase and physical space. Inspection of the aforementioned forward figure-8 criteria reveals that the forward-drifting region also expands, but in general this expansion is small enough to be deemed negligible. We also note that with increasing $\bar{\delta}$, the indeterminate region represented by the brown triangle begins to occupy an increasingly larger fraction of the ρ - Y_{GC} region plot. Thus, in the interests of minimizing the relative magnitudes of the backward-drifting and indeterminate domains, it is clearly desirable for $\bar{\delta}$ to be small.

Included in each \mathcal{H}_k - P_X plot in Figure 3.7 is an arbitrary root mean square (RMS) value for the normalized Hamiltonian of a hypothetical ion ensemble (denoted by $\overline{\mathcal{H}_k}$). In physical space, this corresponds to a RMS Larmor radius value $\bar{\rho}$, which is also included in relevant region plots. For small $\bar{\rho}$, the relative length of the $\bar{\rho}$ segment that falls within a given orbit domain in ρ - Y_{GC} space yields an intuitive (albeit rough) estimate of the relative prominence of that particular orbit in the context of the entire ensemble. For $\bar{\rho}$ close to zero, a majority of ions are trapped in Larmor orbits – very few follow forward-drifting trajectories. As $\bar{\rho}$ increases, the number of ions subject to forward-drifting orbits also initially increases. However, the fraction of ions that “escape” to the walls also grows with $\bar{\rho}$. These two conflicting behaviors imply that for a given thruster geometry, an optimal $\bar{\rho}$ value can be determined such that the percentage of ions subject to forward-drifting orbits is a maximum. But before we can verify this postulate, we must first examine the general behavior of an ion ensemble in a confined magnetic slope geometry via numerical simulation.

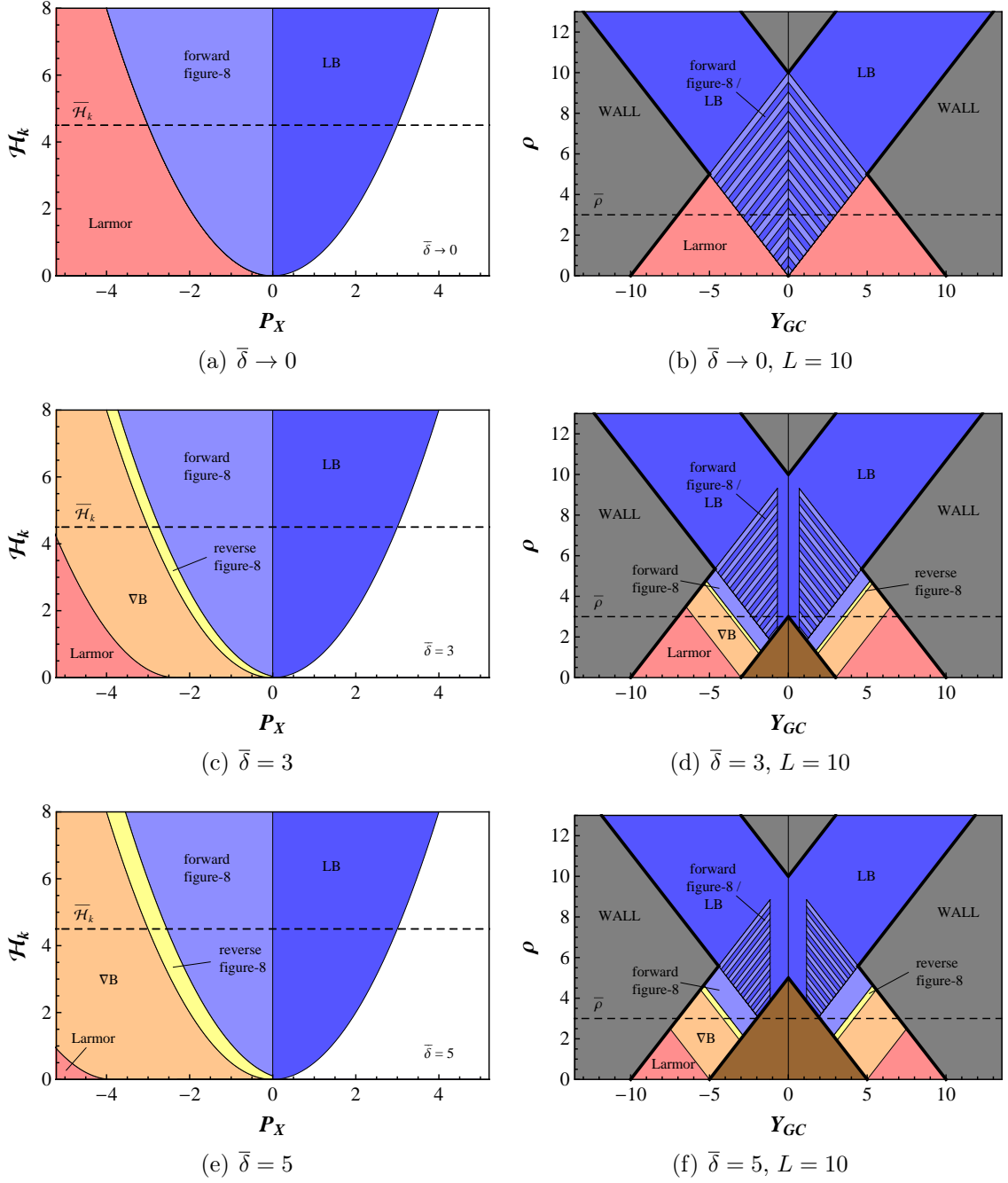


Figure 3.8. Region plots depicting characteristic ion orbit domains in \mathcal{H}_k - P_X and ρ - Y_{GC} space for several values of $\bar{\delta}$. Corresponding RMS \mathcal{H}_k and ρ values ($\bar{\mathcal{H}}_k$ and $\bar{\rho}$, respectively) are included for reference.

3.5 Ensemble Behavior (k -normalized)

To start, we assume that the initial velocity distribution of a collisionless² ion ensemble within the confines of the thruster geometry is described by a two-dimensional (since only the perpendicular velocity is relevant) Maxwell-Boltzmann distribution. Thus, in k -normalized coordinates, the distribution function of each individual velocity component is

$$f_V(V_i) dV_i = \frac{1}{\bar{\rho}\sqrt{\pi}} \exp\left[-\frac{V_i^2}{\bar{\rho}^2}\right] dV_i \quad (3.24)$$

where $V_X = X'$, $V_Y = Y'$, and $\bar{\rho}$ is the normalized RMS Larmor radius of the ensemble. This expression defines a normal distribution of the component V_i with mean value $\mu = 0$ and standard deviation $\sigma = \bar{\rho}/\sqrt{2}$.

To determine the characteristic behavior of such an ensemble in the presence of a magnetic slope, we start with a sample size of approximately 15,000 ions and divide them evenly amongst approximately three thousand starting Y positions (such that $\bar{\delta} < |Y_0| < L$, where the subscript $_0$ denotes an initial value). After defining a desired $\bar{\rho}$ for the ensemble, we then randomly select initial V_X and V_Y values for individual ions by drawing from the distribution defined in (3.24). From V_{X0} and V_{Y0} alone we can determine a given ion's initial Larmor radius by using $\rho_0^2 = V_{X0}^2 + V_{Y0}^2$. From V_{X0} and Y_0 , we can determine P_{X0} from its definition, and thus, by way of (3.18) we can also determine Y_{GC0} .

The left-hand column of Figure 3.9 features contour plots of three two-dimensional Maxwellians in the ρ - Y_{GC} plane, each with a different $\bar{\rho}$ value. Note that no ions start in the indeterminate region ($|Y| < \bar{\delta}$). We see that as $\bar{\rho}$ increases, the distribution widens in ρ as expected. However, we also note that increasing $\bar{\rho}$ causes the two halves of the distribution (one on each side of the magnetic null) to conically diverge.

The right-hand column features the same three distributions, but confines them to the geometry of the thruster. We clearly see that for small $\bar{\rho}$, particles are generally trapped in the Larmor regions and few wall losses are observed. As $\bar{\rho}$ increases, ions begin to populate the forward-drifting regions in much greater numbers, but the divergence of the corresponding unconstrained distribution indicates that wall losses increase significantly with $\bar{\rho}$. Note that in Figure 3.9(f) the triangular regions

²While a collisionless model is clearly not physical, it is a common first-order approximation [39] and greatly simplifies our analysis. We briefly discuss the potential effects of collision in Chapter 5.

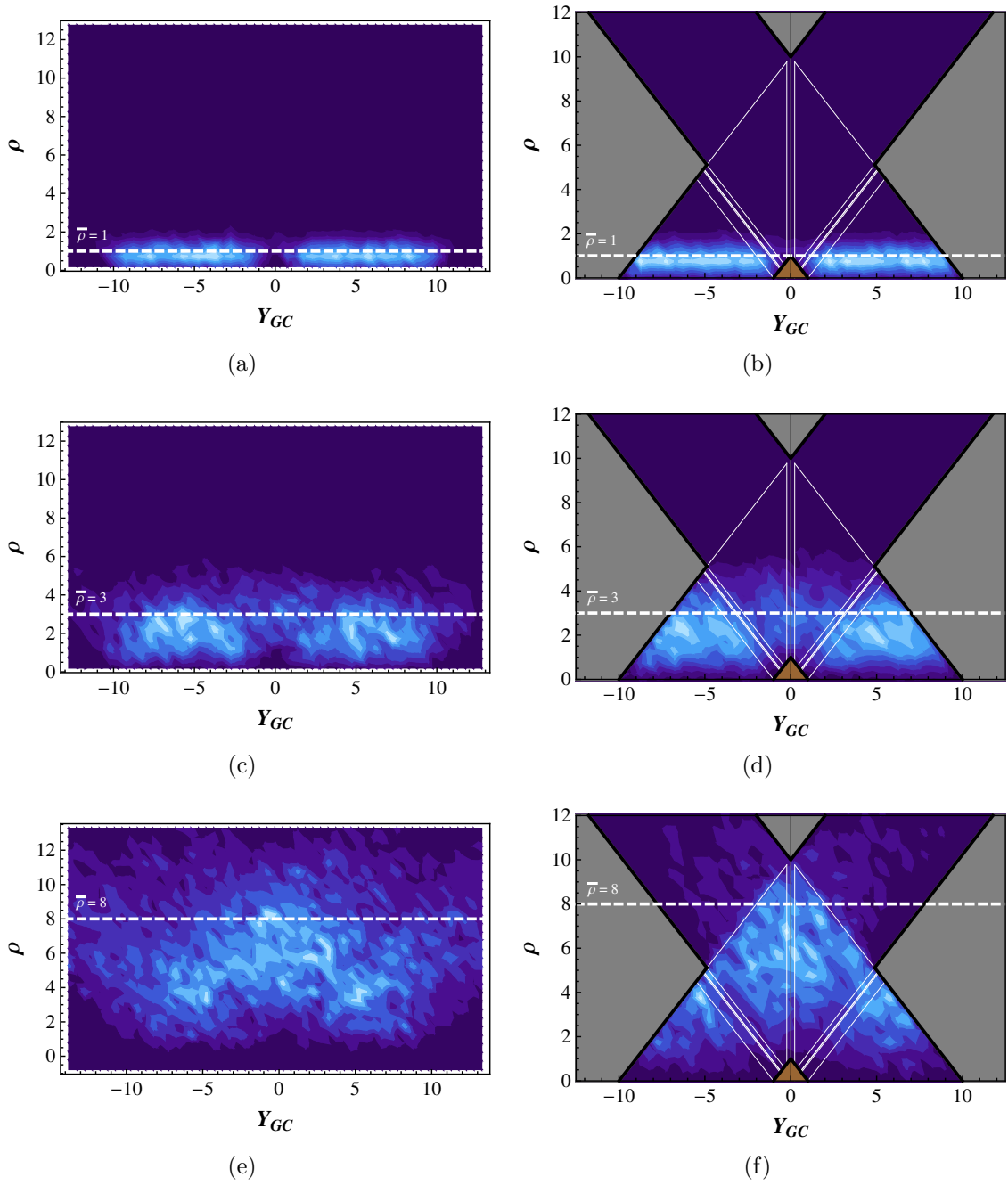


Figure 3.9. The left-hand column features contour plots of three 2-D Maxwellian velocity distributions in the ρ - Y_{GC} plane for various $\bar{\rho}$. Lighter regions indicate greater particle density. The right-hand column depicts these same distributions subject to the constraints of thruster geometry. White lines are used to delimit the orbit domains described in 3.4. For all plots, $\bar{\delta} = 1$ and $L = 10$.

delimiting the forward figure-8 / LB orbit domains have well-defined boundaries in the contour plot. Ion density abruptly falls off as we cross into the purely LB regions. This confined density elevation represents the intersection of the two divergent regions of the unconstrained distribution.

Thus, numerical simulation clearly verifies that while increasing $\bar{\rho}$ pushes particles into the forward-drifting region, it also increases wall losses.

3.5.1 $\bar{\rho}$ Optimization

As aforementioned, the conflicting effects of increasing the normalized RMS Larmor radius imply that an optimal $\bar{\rho}$ value can be determined such that the percentage of ions subject to forward-drifting orbits is a maximum.

In order to quantify this optimum over a wide range of parameters, we loop the numerical simulations used to generate Figure 3.9 and collect data for varying $\bar{\delta}$, $\bar{\rho}$, and L . Two quantities are considered: ξ_{esc} , the percentage of ions that escape to the walls, and ξ_f , the percentage of ions that fall in the forward-drifting region. Both quantities are defined relative to the total number of ions in the initial distribution. These numerical studies reveal that for a given $\bar{\delta}$ (as long as $\bar{\delta}$ is relatively small compared to $\bar{\rho}$ such that $\bar{\delta}/\bar{\rho} \lesssim 1/3$), plots of ξ_{esc} versus the ratio $\bar{\rho}/L$ can be closely approximated by a single mean curve.³ Thus, the fraction of ions that escape to the walls is dependent only on the ratio of the normalized RMS Larmor radius $\bar{\rho}$ to the normalized thruster bound L . For ξ_f , while the mean curve approximation is less valid for large $\bar{\rho}/L$, the region in the vicinity of the maximum is tightly confined. Thus, since we are only interested in quantifying the conditions at this optimum, the mean curve approximation is justified in this case as well.

Figure 3.10 depicts the results of this numerical study for three values of $\bar{\delta}$. Figure 3.10(a) illustrates that ξ_{esc} increases dramatically for $\bar{\rho}/L \lesssim 1$, and less so for $\bar{\rho}/L \gtrsim 1$. Furthermore, for a given $\bar{\rho}/L$, ξ_{esc} clearly increases with $\bar{\delta}$ – yet another reason why small $\bar{\delta}$ is desirable. Thus, Figure 3.10(a) conclusively validates the claim that the fraction of ions that escape to the walls increases with $\bar{\rho}/L$.

Figure 3.10(b) shows that ξ_f has a clear maximum, giving credence to our initial claim that this configuration can indeed be optimized. Clearly, there exists an optimal $\bar{\rho}/L$ such that the fraction of forward-drifting ions is maximized. Polynomial fits in

³Mean curves for a given $\bar{\delta}$ were determined by taking a moving average of the relevant data set.

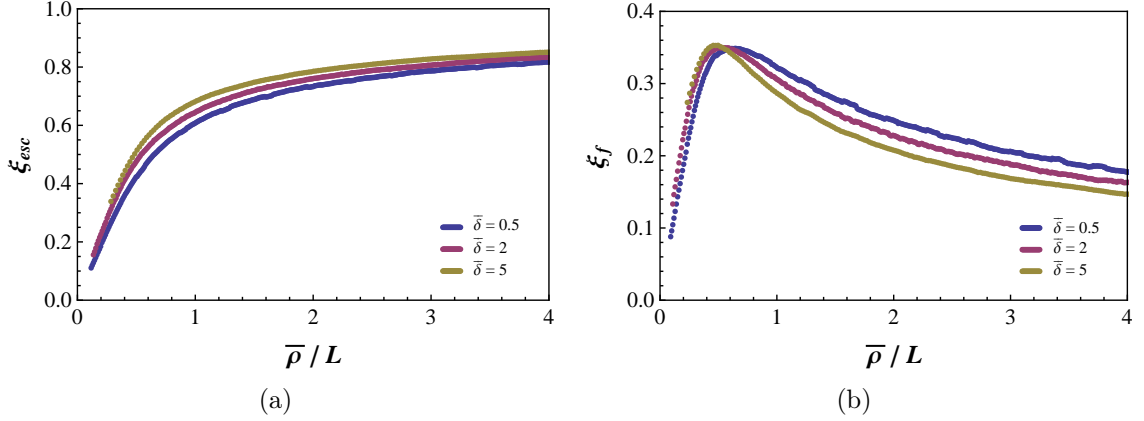


Figure 3.10. Mean curve approximations over a host of $\bar{\rho}$ and L values illustrating the clear dependence of (a) ξ_{esc} and (b) ξ_f on the ratio $\bar{\rho}/L$. (a) reveals a slight upward shift in the ξ_{esc} curve for increasing $\bar{\delta}$, while (b) possesses a clear maximum in ξ_f that appears to shift leftward as $\bar{\delta}$ is increased.

the vicinity of these maxima for various $\bar{\delta}$ reveal that

$$\xi_{f,max} \approx 0.353 \pm 2\% \quad (3.25)$$

$$\left(\frac{\bar{\rho}}{L}\right)_{max} \approx 0.647 - 0.0443 \bar{\delta} \quad (3.26)$$

The maximum $\xi_{f,max}$ varies little with $\bar{\delta}$, and is essentially constant. The optimal value of $\bar{\rho}/L$ decreases with $\bar{\delta}$, and can be approximated by the linear dependence featured in (3.26). Therefore, the maximum fraction of a Maxwellian ion distribution subject to forward-drifting orbits for a given geometric configuration is approximately 35%. Furthermore, this maximum occurs when the geometric parameters approximately satisfy (3.26). However, inspection of Figure 3.10(a) reveals that at $(\bar{\rho}/L)_{max}$, the corresponding value for ξ_{esc} hovers around 0.5. Thus, while the fraction of forward-drifting ions is indeed a maximum, approximately 50% of the ions still escape to the walls – certainly not a trivial fraction.

Next we use these criteria to determine the optimal $\bar{\rho}$ value for the geometric configuration featured in Figure 3.10 ($\bar{\delta} = 1$, $L = 10$). From (3.26), we determine that the optimal $\bar{\rho}$ is approximately 6.0. For this distribution, simulation returns ξ_{esc} and ξ_f values of 0.495 and 0.35, respectively, both of which are in the range we expect. Figure 3.11 features a contour plot of this optimized configuration.

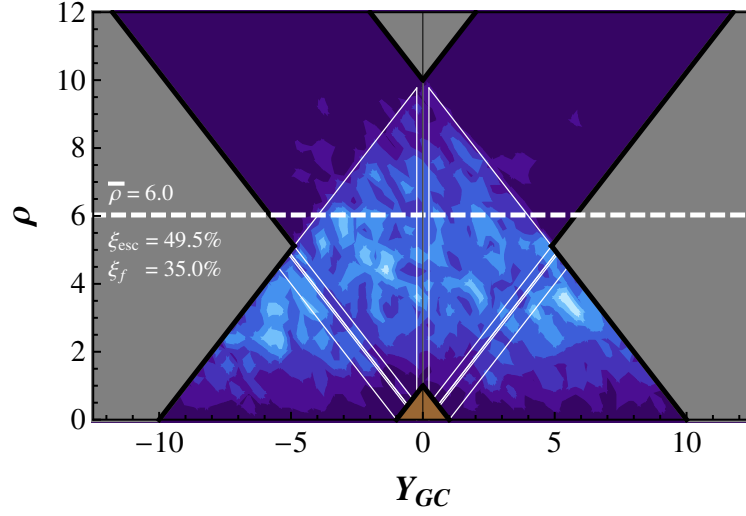


Figure 3.11. Contour plot depicting the optimal Maxwellian for $\bar{\delta} = 1$ and $L = 10$.

Note that if any two of the three parameters in (3.26) are known, an accurate optimum value for the third can be provided so long as the previously prescribed conditions on $\bar{\delta} / \bar{\rho}$ and $\bar{\delta} / L$ are satisfied.

3.6 Alternative Hamiltonian Formulation

In this section, we pause from our discussion of ensemble behavior, and consider an alternate representation of the Hamiltonian before proceeding. Rather than normalizing length by k , the wave number of the propagating electrostatic waves, we consider normalization by $\bar{\rho}_L$, the RMS Larmor radius of a hypothetical ion ensemble.⁴ This formulation has some significant advantages in the context of ensemble simulation that will soon become apparent.

⁴The RMS Larmor radius $\bar{\rho}_L$ is not to be confused with the normalized RMS Larmor radius $\bar{\rho}$. $\bar{\rho}_L$ has units of length, while $\bar{\rho}$ is dimensionless.

The $\bar{\rho}_L$ -normalized BEW Hamiltonian $\mathcal{H}_{\bar{\rho}_L}$ is

$$\mathcal{H}_{\bar{\rho}_L} = \frac{1}{2} \left([P_X - \bar{A}_X]^2 + P_Y^2 \right) + \frac{\varepsilon}{\kappa} \sum_{i=1}^2 \cos(\kappa X - \nu_i \tau) \quad (3.27)$$

where

$$\begin{aligned} \mathcal{H}_{\bar{\rho}_L} &= \frac{1}{m\omega_{ci}^2 \bar{\rho}_L^2} h & \tau &= \omega_{ci} t & \nu_i &= \frac{\omega_i}{\omega_{ci}} & \kappa &= k \bar{\rho}_L & \varepsilon &= \frac{qE_0}{m\omega_{ci}^2 \bar{\rho}_L} \\ X &= \frac{x}{\bar{\rho}_L} & Y &= \frac{y}{\bar{\rho}_L} & \bar{A}_X &= \frac{q}{m\omega_{ci} \bar{\rho}_L} A_x(\bar{\rho}_L Y) \\ P_X &= X' + \bar{A}_X & P_Y &= Y' & \nu_1 &= \nu & \nu_2 &= \nu + 1 \end{aligned}$$

and the prime ($'$) again denotes differentiation with respect to τ .

Note that in the unperturbed case ($\varepsilon = 0$), this Hamiltonian is symbolically identical to the k -normalized Hamiltonian. Thus, all of the analysis that we have performed on \mathcal{H}_k equally applies to $\mathcal{H}_{\bar{\rho}_L}$. While the difference in normalization changes the meaning of the variables, the relationships between them are preserved.

The principle advantage of this normalization scheme has to do with the normalized RMS Larmor radius $\bar{\rho}$ – clearly a very important parameter when considering ensemble behavior within the thruster geometry. In the context of k -normalization, $\bar{\rho} = k\bar{\rho}_L$. Normalization by $\bar{\rho}_L$, however, yields $\bar{\rho} = \bar{\rho}_L / \bar{\rho}_L = 1$. Thus, in the RMS Larmor radius normalization scheme, $\bar{\rho}$ is fixed at one, and therefore completely independent of temperature. Coupled with (3.24), this implies that the corresponding expression for the Maxwellian distribution function is also fixed; therefore, we can simulate the behavior of a thermalized ion ensemble without needing to specify the actual ion temperature. Thus, ensemble studies conducted in the context of the $\bar{\rho}_L$ -normalization are theoretically generalizable to all values of T_i .

3.7 Ensemble Behavior ($\bar{\rho}_L$ -normalized)

In $\bar{\rho}_L$ -normalized coordinates, a 2-D Maxwellian has the following velocity component distribution:

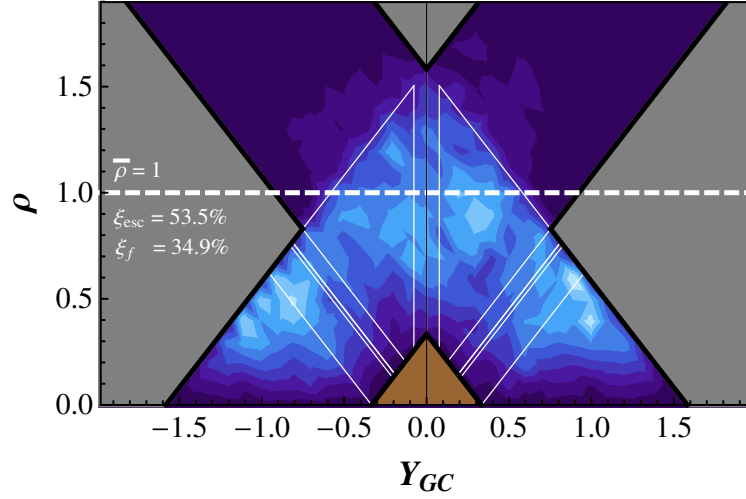


Figure 3.12. Contour plot depicting the optimal thruster geometry for a $\bar{\rho}_L$ -normalized ion ensemble with $\bar{\delta} = 1/3$. This is equivalent to the optimal thruster configuration for a k -normalized ensemble with $\bar{\delta} = 1/3$ and $L = 1.6$.

$$f_V(V_i) dV_i = \frac{1}{\sqrt{\pi}} \exp[-V_i^2] dV_i \quad (3.28)$$

This expression defines a normal distribution of the component V_i with mean value $\mu = 0$ and standard deviation $\sigma = 1/\sqrt{2}$. Again, this distribution is fixed; it is a universal Maxwellian that represents a thermalized ion ensemble at an arbitrary temperature.

3.7.1 L Optimization

Note that the behavior of a $\bar{\rho}_L$ -normalized ensemble in a magnetic slope configuration is identical to the behavior of a k -normalized ensemble with $\bar{\rho} = 1$. Thus, if we specify a value for $\bar{\delta}$ (again, such that $\bar{\delta}/\bar{\rho} \lesssim 1/3$), we can use (3.26) to determine an ideal value for the thruster wall bound L . In fact, for a $\bar{\rho}_L$ -normalized ion ensemble, since $\bar{\rho}$ is equal to one by definition, (3.26) becomes a one-to-one function relating L_{max} and $\bar{\delta}$:

$$L_{max} \approx \frac{1}{0.647 - 0.0443 \bar{\delta}} \quad (3.29)$$

For $\bar{\delta} = 1/3$ (the upper bound of our restriction on $\bar{\delta}/\bar{\rho}$), we find that the optimal L value is approximately 1.6. In this configuration, approximately 34.9% of the ions fall

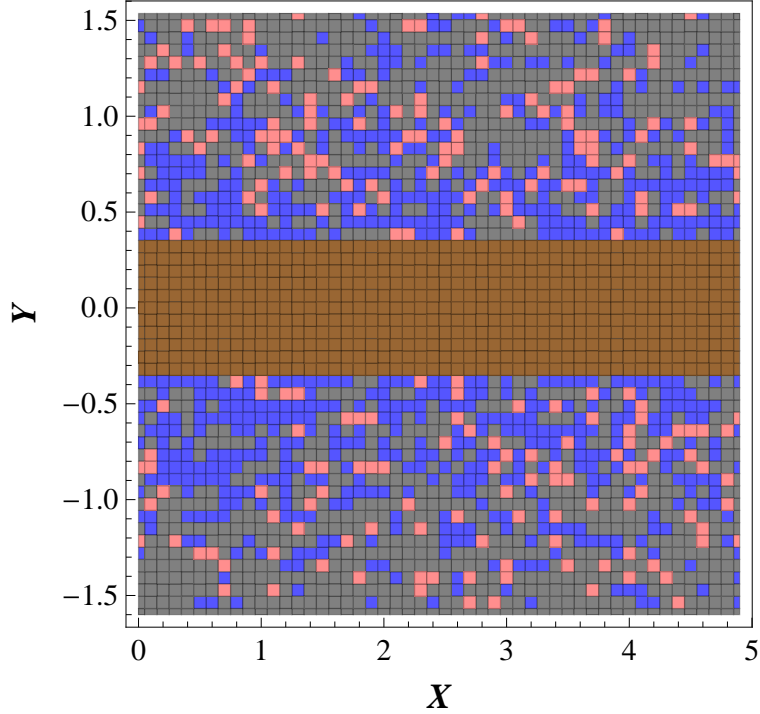


Figure 3.13. Distribution of ion trajectories in physical space for the optimized geometry determined in Section 3.7.1. Brown squares indicate ions that start in the magnetic slope region ($\bar{\delta} = 1/3$), gray squares indicate ions that are lost to the walls, red squares indicate ions that are trapped in Larmor or reverse-drifting orbits, and blue squares indicate ions that follow forward-drifting trajectories.

in the forward-drifting region, while 53.5% are lost to the walls. Given the constraint on the magnitude of $\bar{\delta}$ and the fact that the value of $\bar{\rho}$ is fixed, this geometric configuration essentially represents the universal optimum for every thermalized distribution of ions subject to a steeply-sloped z -directed magnetic field.

3.8 Benchmark Specific Impulse

In this section, we continue with our treatment of $\mathcal{H}_{\bar{\rho}_L}$ and determine a theoretical specific impulse value for our L -optimized thruster geometry. We begin with a distribution of ions in physical space whose initial velocities have been randomly determined by sampling from the $\bar{\rho}_L$ -normalized Maxwellian distribution in (3.28). A sample distribution of trajectories for such an ensemble is featured in Figure 3.13.

To determine the theoretical exhaust velocity of such an ensemble, we clearly only need to consider forward-drifting ions. For completeness, we also consider ions that

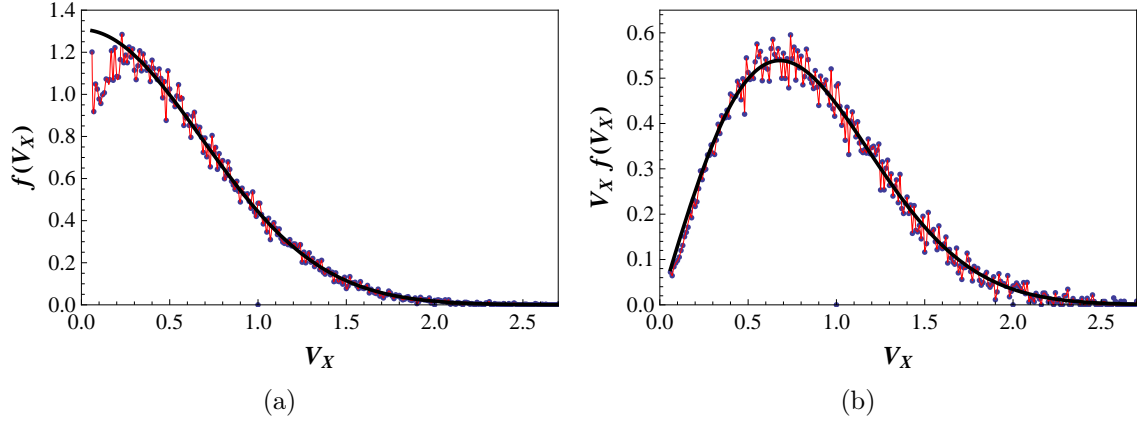


Figure 3.14. (a) Average exit velocity distribution. The black curve is a half-Gaussian best fit. (b) A plot of the product of exit velocity and the distribution $f(V_X)$. The integral of the resulting curve is the average exit velocity, or the (normalized) exhaust velocity U_{ex} .

start in the sloped region, which we neglected in our analytical treatment. Furthermore, for this analysis, we assume that ions lost to the walls do not contribute to the exhaust plume. To determine the exhaust velocity, we concentrate our ensemble in a very small X -range (~ 0.1) and specify a plane in X that we define as the exit plane. An ion that breaks this plane is considered part of the exhaust plume, and the average velocity V_X at which it does so is considered to be the exit velocity of the ion. As expected, the exhaust velocity of the thruster is defined as the average velocity of the exhaust plume.

The obvious drawback to using this particular technique is that for small time intervals, only the fastest ions will actually be able to break the exit plane, thereby skewing numerical results in favor of a higher average exhaust velocity. However, the error associated with this method can be mitigated both by increasing the time interval over which the numerical integration is performed and by decreasing the relative X -distance between the ion's starting position and the exit plane.

Figure 3.14(a) depicts the exit velocity distribution for a sample size of approximately 10,000 ions. This plot unambiguously demonstrates that the magnetic slope configuration can indeed produce a net linear ion current in the X -direction. The distribution can be approximated by a half-Gaussian, which agrees very well with numerical results for large V_X . But for small V_X , numerical results clearly diverge from the fit. While this could indeed be a characteristic of the thruster itself (which is likely given that this drop-off was observed even for very large time intervals), it

could also be a result of the drawbacks of our chosen method. However, seeing as the exhaust velocity is defined such that

$$U_{ex} = \int_0^\infty V_X f(V_X) dV_X \quad (3.30)$$

and noting the improved correlation of the transformed fit in Figure 3.14(b), we conclude that for the purposes of exhaust velocity calculations, the half-Gaussian approximation is acceptable.

In the end, this simulation yields a normalized exhaust velocity U_{ex} of 0.6. In other words, in this optimized geometry in the unperturbed case, the average exiting ion enters the exhaust plume with an X -velocity equal to 60% of the average initial perpendicular velocity of the ensemble.

From this normalized exhaust velocity value, we use realistic physical parameters to calculate the benchmark I_{sp} for the optimal unperturbed thruster configuration. By definition,

$$U_{ex} = \frac{u_{ex}}{\bar{v}} \quad (3.31)$$

where \bar{v} is the RMS velocity of the 2-D ensemble. Also by definition (see Appendix C),

$$\bar{v} = \sqrt{\frac{2k_B T_i}{m}} \quad (3.32)$$

where k_B is Boltzmann's constant, T_i is the temperature of the ion ensemble, and m is the ion mass. Thus, by specifying an ion temperature T_i and recalling our expression (1.2) for I_{sp} , we can determine u_{ex} for an ensemble of ions each with mass m .

Let us consider an ensemble of hydrogen ions ($m \approx 1.67 \times 10^{-27}$ kg) with an average temperature of $T_i = 0.1$ eV. For $g_0 = 9.81$ m/s², this yields a theoretical I_{sp} of approximately 270 s. For an ensemble of argon ions ($m \approx 6.63 \times 10^{-26}$ kg), this theoretical I_{sp} drops precipitously to about 40 s.

3.9 Benchmark Thrust

Next we use the average exhaust velocity distribution to determine an approximate expression for the thrust generated by this magnetic slope configuration. We recall

from Chapter 1 that thrust is defined as

$$\mathbf{T} = \dot{m}\mathbf{u}_{ex} \quad (3.33)$$

By assuming that these two quantities are not independent, we can approximate the \dot{m} term as follows:

$$\dot{m} = nm\xi_f A u_{ex} = 2nm\xi_f \bar{\rho}_L L_{max} \ell u_{ex} \quad (3.34)$$

where A is the cross-sectional area of the thruster, ℓ is the depth of the thruster in the z -direction, n is the average ion density, and m is the ion mass. The inclusion of ξ_f accounts for the fact that only forward drifting ions contribute to the mass flow from the thruster. Thus, we can approximate the thrust generated per unit thruster depth (in z) in terms of fundamental physical parameters as follows:

$$\frac{T}{\ell} = 2nm\xi_f \bar{\rho}_L L_{max} u_{ex}^2 = 2^{5/2} (\xi_f L_{max} U_{ex}^2) \frac{n\sqrt{m}(k_B T_i)^{3/2}}{qB_0} \quad (3.35)$$

We see from the above expression that we can change the thrust of the unperturbed optimized configuration for a given plasma via the manipulation of three parameters: n , T_i , and B_0 . However, this expression is only an approximation, and considers neither the mechanism by which thrust is actually transferred to the spacecraft nor the complex particle interactions that are often characteristic of plasma behavior. Nevertheless, it should still provide a somewhat reasonable estimate for the expected thrust level of a given configuration. Even if the actual values it produces turn out to be inaccurate, the expression can still be used to gauge the relative thrust levels of comparable configurations.

In calculating hypothetical thrust values, we use data collected by Jorns and Choueiri in 2010 from the second-generation Beating Wave Experiment (BWXII) [40]. Thus, for a singly ionized argon plasma with $n \approx 10^{10} \text{ cm}^{-3}$ and $T_i \approx 0.1 \text{ eV}$ in a B-field of 500 Gauss, the calculated linear thrust density is approximately $7.4 \times 10^{-7} \text{ N/m}$ – an incredibly small result. For a hydrogen plasma of equal density and temperature, the thrust density is even lower: $T/\ell \approx 1.2 \times 10^{-7} \text{ N/m}$.

3.10 Introduction to the Perturbed Case ($\varepsilon \neq 0$)

The calculated specific impulse values featured in Section 3.8 are remarkably low for electric thrusters. However, given the fact that in the unperturbed case, the Hamiltonian of each individual ion is conserved, these results are unsurprising. In its current form, this magnetic field configuration essentially takes the thermal energy of an ion ensemble and concentrates a portion of it in the $+X$ -direction, establishing a linear ion current along the magnetic null. If the thruster were 100% efficient, it would concentrate 100% of that thermal energy such that $U_{ex} \approx 1$. Thus, in its current configuration (and for the specified ion temperature), the maximum I_{sp} (assuming $U_{ex} = 1$) for a hydrogen thruster of this type is only about 450 s (for an argon thruster it is approximately 70 s). Much of the same reasoning applies to why the thrust values calculated in Section 3.9 are so low.

In the interest of enhancing both current flow and current density along the magnetic null (and thereby increasing both the net thrust and I_{sp} of the thruster), in the next chapter we consider the perturbed case ($\varepsilon \neq 0$) and investigate the effects that BEW propagation have on the propulsive characteristics of the sloped field configuration.

Chapter 4

Effects of BEW Propagation

In this chapter, we study the corresponding perturbed case ($\varepsilon \neq 0$) in which ions within the confines of the thruster geometry are subject to BEW. Our ultimate goal is to demonstrate that BEW propagation increases and enhances ion current flow along the magnetic null, thereby significantly improving the propulsive characteristics of the BWT configuration. First, using the initial analysis conducted by Jorns and Choueiri as a guide [1], we briefly discuss how BEW propagation can alter ion orbits in the presence of a magnetic slope. We then attempt to eliminate unphysical combinations of ν and κ by introducing a normalized expression for the dispersion relation of an electrostatic ion cyclotron wave propagating in a real plasma. After determining a rough estimate for the optimal ν and κ values as a function of wave amplitude ε , we then conduct numerical simulations using Monte Carlo methods to determine the effects of BEW on specific impulse, thrust generation, and wall losses within the thruster. We conclude with a summary of major findings.

4.1 Perturbed Ion Trajectories ($\varepsilon \neq 0$)

In this section, we consider single-ion dynamics for $\varepsilon \neq 0$. Recall that the $\bar{\rho}_L$ -normalized BEW Hamiltonian is

$$\mathcal{H}_{\bar{\rho}_L} = \frac{1}{2} \left([P_X - \bar{A}_X]^2 + P_Y^2 \right) + \frac{\varepsilon}{\kappa} \sum_{i=1}^2 \cos(\kappa X - \nu_i \tau) \quad (4.1)$$

Given that this formulation lends itself to ensemble analysis, we will be working with the $\bar{\rho}_L$ -normalized Hamiltonian for the remainder of this chapter.

Our goal is to determine how BEW propagation alters the orbits of unperturbed

ions. Following the convention of Jorns and Choueiri [1], we partition our analysis by grouping ions based on the relationship between the initial Y -position of the guiding center Y_{GC0} , the initial normalized Larmor radius ρ_0 , and the stochastic threshold for BEW acceleration ρ_{th} . Note that while the (k -normalized) stochastic threshold was defined as $\rho_{th} = \nu - \sqrt{\varepsilon}$ in Chapter 2, $\bar{\rho}_L$ normalization yields a slightly different expression due to the presence of an additional parameter κ [38]:

$$\rho_{th} = \frac{\nu}{\kappa} - \sqrt{\frac{\varepsilon}{\kappa}} \quad (4.2)$$

First we group unperturbed ions into two categories: a forward-drifting category (which includes forward figure-8 and LB trajectories) and a non-forward-drifting category (which includes reverse figure-8, grad-B, and Larmor trajectories). Recall from Chapter 3 that a given unperturbed ion will only follow a forward-drifting trajectory if $\rho_0 > \rho_f$, where

$$\rho_f = |Y_{GC0}| - \frac{\bar{\delta}}{3} \ln(2 \cosh 3) + \alpha \bar{\delta} \quad (4.3)$$

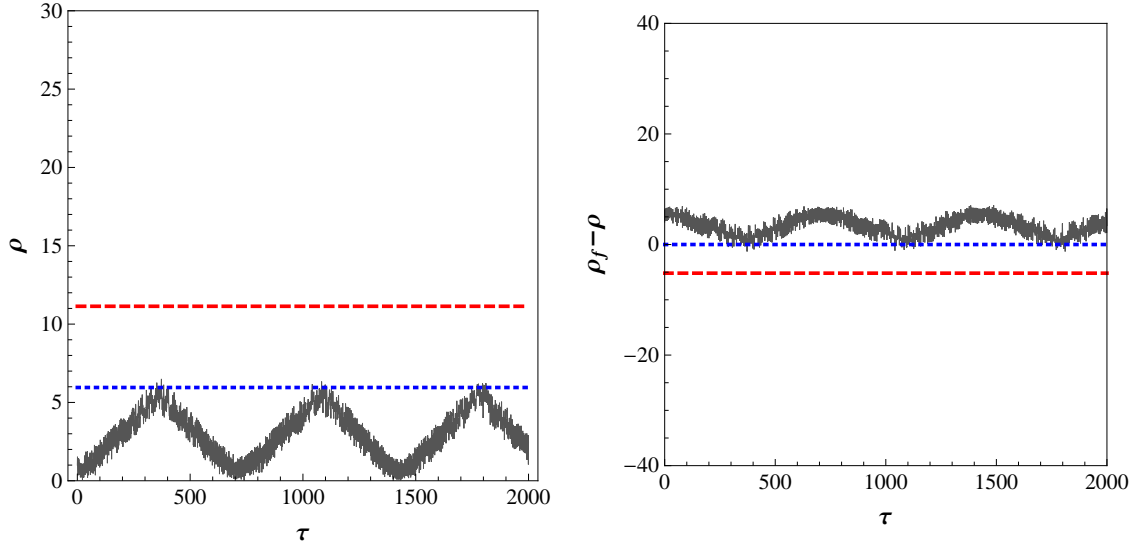
Next, we treat four relevant cases of motion based on the initial conditions of a given ion (more specifically, the relationship between ρ_0 , ρ_f , and ρ_{th}).

CASE 1: $\rho_0 < \rho_f < \rho_{th}$

In the case where $\rho_0 < \rho_f < \rho_{th}$, the ion starts in the non-forward-drifting regime, and the Larmor radius at which it enters the forward-drifting regime is *below* the stochastic threshold for BEW acceleration.

Figure 4.1 depicts the time evolution of ρ and $\rho_f - \rho$ for a test ion subject to BEW that satisfies $\rho_0 < \rho_f < \rho_{th}$. The sign of $\rho_f - \rho$ determines the drift behavior of the ion. For $\rho - \rho_f > 0$, the Larmor radius of the ion is less than the Larmor radius required to enter the forward-drifting region; therefore, the ion follows a non-forward-drifting trajectory. For $\rho_f - \rho$, the ion's gyroradius is greater than the Larmor radius required for the ion to enter the forward-drifting regime; thus, the ion follows a forward-drifting trajectory.

Figure 4.1(a) shows that for $\rho_0 < \rho_f < \rho_{th}$, the test ion coherently accelerates up to ρ_f , but immediately decelerates upon encountering the magnetic null. Figure 4.1(b) depicts the same behavior: the ion coherently approaches the forward-drifting



(a) Time evolution of ρ (gray). The dotted blue line represents ρ_f ; the dashed red line represents ρ_{th} . (b) Time evolution of $\rho_f - \rho$ (gray). The dotted blue line represents the boundary between forward-drifting and non-forward-drifting trajectories; the dashed red line represents the stochastic threshold ($\rho_f - \rho_{th}$).

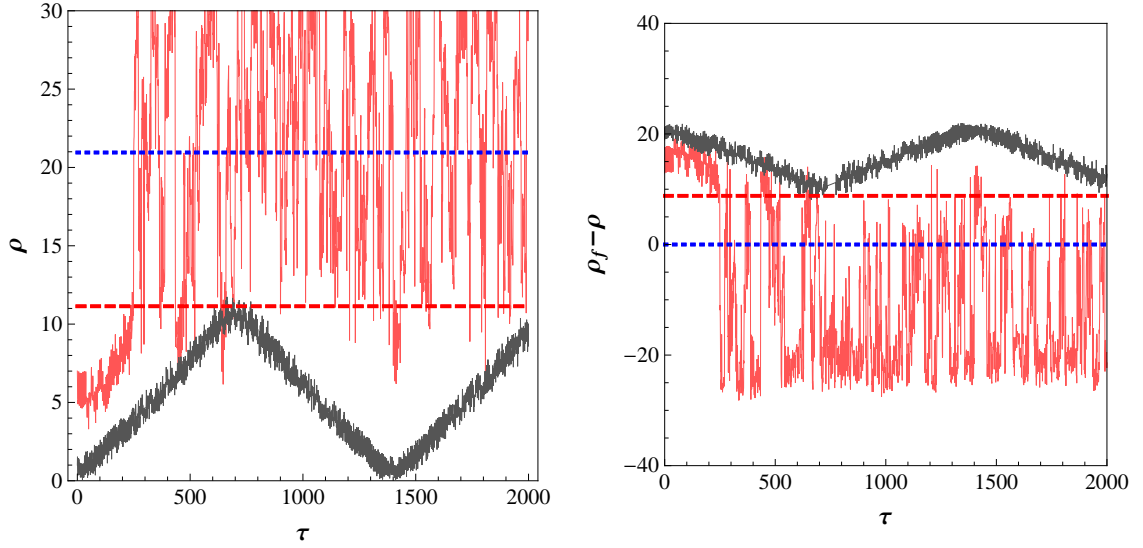
Figure 4.1. Time evolution of (a) ρ and (b) $\rho_f - \rho$ for $\rho_0 < \rho_f < \rho_{th}$ (wave parameters: $\varepsilon = 10$, $\nu_1 = 14.3$, and $\kappa = 1$).

region, but is deflected upon reaching the $\rho_f - \rho = 0$ barrier. While numerical results have shown that this does not necessarily prevent the ion from entering the forward-drifting regime, it *does* prevent the ion from remaining in the forward-drifting regime for appreciable periods of time (i.e. more than a few Larmor orbits). These ions tend to experience periodic kicks in X_{GC} that are too small and infrequent to be considered forward-drifting. Thus, we conclude that on the whole, ions initially in non-forward-drifting orbits *cannot* be coherently accelerated into the forward-drifting regime.

CASE 2: $\rho_0 < \rho_{th} < \rho_f$

For $\rho_0 < \rho_{th} < \rho_f$, the ion clearly starts outside the forward-drifting regime, and the Larmor radius at which it enters said regime is *above* the BEW stochastic threshold.

The gray curve in Figure 4.2(a) represents an ion that starts in the forbidden acceleration region. As expected, the ion coherently accelerates up to the stochastic threshold ρ_{th} and then decelerates, never reaching the forward-drifting regime. The



(a) Time evolution of ρ . The dotted blue line represents ρ_f ; the dashed red line represents ρ_{th} . (b) Time evolution of $\rho_f - \rho$. The dotted blue line represents the boundary between forward-drifting and non-forward-drifting trajectories; the dashed red line represents the stochastic threshold ($\rho_f - \rho_{th}$).

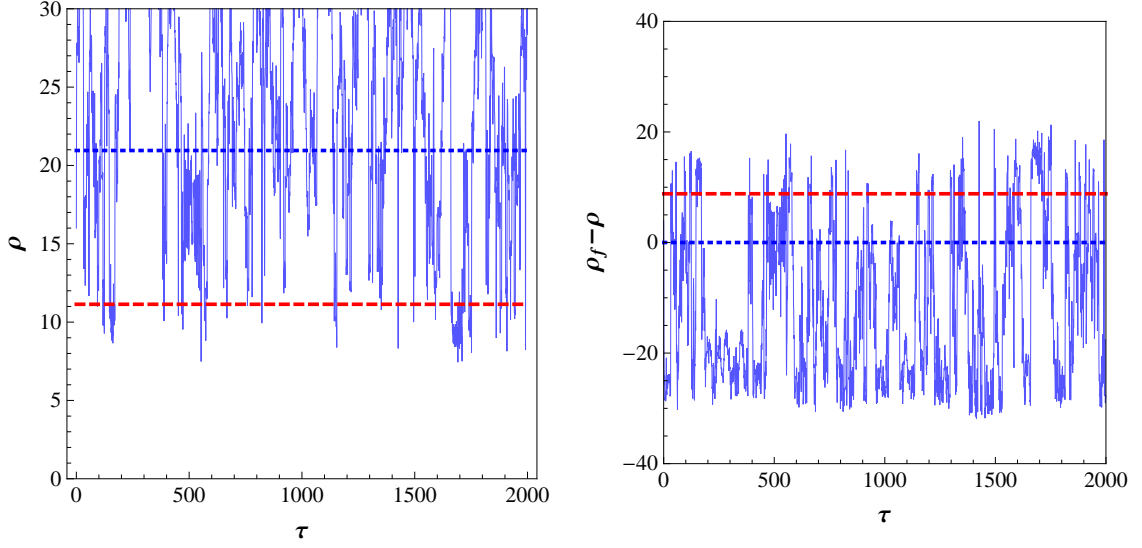
Figure 4.2. Time evolution of (a) ρ and (b) $\rho_f - \rho$ for $\rho_0 < \rho_{th} < \rho_f$ (wave parameters: $\varepsilon = 10$, $\nu_1 = 14.3$, and $\kappa = 1$). The gray curves represent an ion in the forbidden acceleration region; the red curves represent an ion in the regular acceleration region.

red curve, however, represents an ion that begins in the regular acceleration region. This ion is coherently accelerated up to the threshold ρ_{th} where it is then stochastically accelerated into the forward-drifting regime (where it remains, on average; see Figure 4.2(b)). Thus, for $\rho_0 < \rho_{th} < \rho_f$, BEW propagation can clearly push an ion into the forward-drifting regime as long as it begins in the regular acceleration region. To simplify our analysis, we make the same approximation as Jorns and Choueiri and assume that on average (over θ) ions with $\rho_0 > \rho_{th}/2$ (i.e. ρ above the elliptic point **E**) are subject to regular acceleration [1]. Thus, we define our first criterion for non-forward-drifting ions to be pushed into the forward-drifting regime:

$$\frac{\rho_{th}}{2} < \rho_0 < \rho_{th} < \rho_f \quad (4.4)$$

CASE 3: $\rho_{th} < \rho_0 < \rho_f$

In the case where $\rho_{th} < \rho_0 < \rho_f$, the ion begins outside the forward-drifting regime, but its initial Larmor radius places it in the stochastic acceleration region.



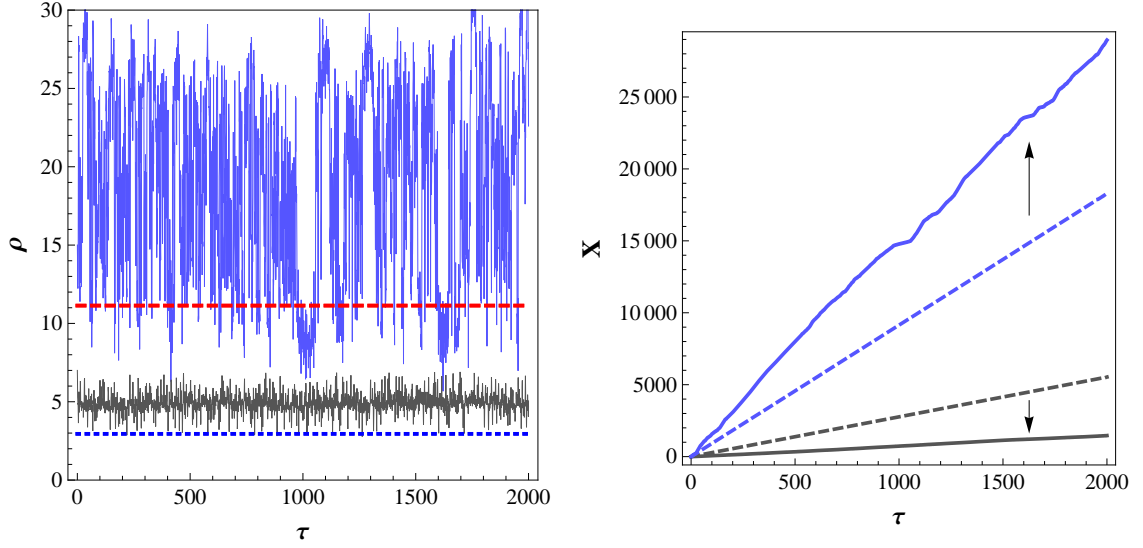
(a) Time evolution of ρ . The dotted blue line represents ρ_f ; the dashed red line represents ρ_{th} . (b) Time evolution of $\rho_f - \rho$. The dotted blue line represents the boundary between forward-drifting and non-forward-drifting trajectories; the dashed red line represents the stochastic threshold ($\rho_f - \rho_{th}$).

Figure 4.3. Time evolution of (a) ρ and (b) $\rho_f - \rho$ for $\rho_{th} < \rho_0 < \rho_f$ (wave parameters: $\varepsilon = 10$, $\nu_1 = 14.3$, and $\kappa = 1$). The gray curves represent an ion in the forbidden acceleration region; the red curves represent an ion in the regular acceleration region.

Figure 4.3 clearly illustrates that this ion is stochastically accelerated from the outset and promptly enters the forward-drifting regime, where it remains on average for all time. Thus, we can generalize (4.5) to all ions with $\rho_0 < \rho_f$ as follows:

$$\frac{\rho_{th}}{2} < \rho_0 < \rho_f \quad (4.5)$$

This expression defines the conditions under which an ion initially following a non-forward-drifting trajectory can be pushed into the forward-drifting region. Thus, the magnitude of ρ_{th} essentially determines the fraction of the reverse-drifting and Larmor populations that can be linearly accelerated along the magnetic null. The smaller the magnitude of ρ_{th} , the greater the number of ions in a given thermalized distribution that can be pushed into forward-drifting trajectories.



(a) Time evolution of ρ . The dotted blue line represents ρ_f ; the dashed red line represents ρ_{th} . (b) Time evolution of X . Dashed lines represent unperturbed trajectories; solid lines represent perturbed trajectories. The X velocity of an ion is defined as the slope of its corresponding curve.

Figure 4.4. Time evolution of (a) ρ and (b) X for $\rho_f < \rho_0 < \rho_{th}$ (gray) and $\rho_f < \rho_{th} < \rho_0$ (blue) for wave parameters $\varepsilon = 10$, $\nu_1 = 14.3$, and $\kappa = 1$).

CASE 4: $\rho_0 > \rho_f$

The final case considers the possibility that ions initially in the forward-drifting region may be pushed into non-forward-drifting orbits as a result of BEW propagation.

Numerical results indicate that these initially forward-drifting ions tend to remain in the forward-drifting region even after BEW perturbation. However, the manner in which their trajectories propagate in X tends to change based on the magnitude of ρ_0 relative to ρ_{th} .

As one might expect, ions with $\rho_0 > \rho_{th}$ tend to stochastically accelerate as they drift forward in X (see Figure 4.4(a)). As a consequence of this stochastic acceleration, their resultant perturbed X velocities tend to be much higher than their originally-unperturbed counterparts. The blue curves in Figure 4.4(b) demonstrate this velocity shift. While the dashed blue line represents the unperturbed X trajectory, the solid blue line represents the corresponding perturbed X trajectory. The plot clearly demonstrates that the X velocity of the ion (i.e. the slope of the corresponding blue curve) jumps after the application of BEW.

For $\rho_0 < \rho_{th}$, however, forward-drifting ions tend not to accelerate at all (see Figure 4.4(a)). The only exception occurs when ions are in the immediate vicinity of ρ_{th} . These ions do tend to undergo regular acceleration and subsequently jump into the stochastic regime. However, aside from this limited range of ρ_0 values near the stochastic threshold, most forward-drifting ions actually exhibit an appreciable *decrease* in X velocity upon encountering BEW. Figure 4.4(b) illustrates this substantial decrease in velocity for a test ion with $\rho_f < \rho_0 < \rho_{th}$ upon BEW propagation.

Therefore, not only does lowering ρ_{th} effectively increase the number of trapped ions that can be pushed into the forward-drifting region for a given distribution, but it also greatly enhances the flow of ions that were already following forward-drifting trajectories prior to BEW propagation. Thus, we can conclude that by decreasing the magnitude of ρ_{th} , it is likely that we can also dramatically improve the performance of the BWT thruster.

4.2 Ion Channeling

BEW propagation also has a visible benefit in the context of electric propulsion due to the tendency of guiding centers to drift in the $\mathbf{k} \times \mathbf{B}$ direction after the onset of stochasticity. In the context of this sloped field configuration, this implies that ions in the stochastic region will actually be siphoned towards the magnetic null, a phenomenon which we will henceforth refer to as “ion channeling.”

Figure 4.5 illustrates this phenomenon for a test ion in the regular acceleration region. We see that Y_{GC} remains roughly constant while the ion coherently accelerates. Upon breach of the stochastic threshold, however, the guiding center drops precipitously in Y and gravitates towards the magnetic null, after which it enters the forward-drifting region and the average value of Y_{GC} approaches zero.

Numerical results indicate that ions subject to SEW experience a similar $\mathbf{k} \times \mathbf{B}$ drift in their guiding centers. However, since the stochastic regime is accessible to a larger portion of the ion population in the beating wave case, we expect the channeling effect to be generally more prominent for BEW than for SEW.

This channeling behavior is important from a propulsion standpoint because it implies a net stochastic transport of particles towards the magnetic null, and therefore away from the thruster walls. This effect therefore helps to mitigate characteristic wall losses that hinder the performance of many existing electric thrusters.

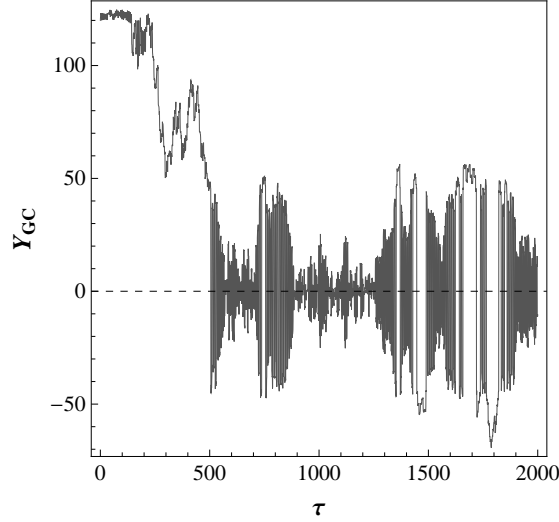


Figure 4.5. Time evolution of Y_{GC} for a test ion in the regular acceleration regime ($\varepsilon = 10$, $\nu_1 = 14.3$, and $\kappa = 1$). Dense regions about the magnetic null are characteristic of forward-drifting trajectories, in which the guiding center switches sign each time the ion crosses $Y = 0$.

4.3 EIC Dispersion Relation

According to the definition of ρ_{th} :

$$\rho_{th} = \frac{\nu}{\kappa} - \sqrt{\frac{\varepsilon}{\kappa}} \quad (4.6)$$

we can make the stochastic threshold arbitrarily small by manipulating the parameters ε , ν , and κ as we please. In fact, if we increase the normalized amplitude enough, the above expression implies that we can even have a *negative* stochastic threshold.

However, this notion of an arbitrarily small (or negative) ρ_{th} is unphysical in that it neglects the actual behavior of EIC waves in a plasma. The first problem is that in a real plasma, ν and κ are not independent of one another. EIC waves propagate according to the following (approximate) dispersion relation (for $T_e \gg T_i$, where T_e is the electron temperature and T_i is the ion temperature) [40]:

$$\omega^2 = \omega_{ci}^2 + k^2 \frac{Z k_B T_e}{m} \quad (4.7)$$

where Z is the ion charge (in units of e). In $\bar{\rho}_L$ -normalized coordinates, this expression becomes

$$\nu^2 = 1 + \kappa^2 \frac{Z T_r}{2} \quad (4.8)$$

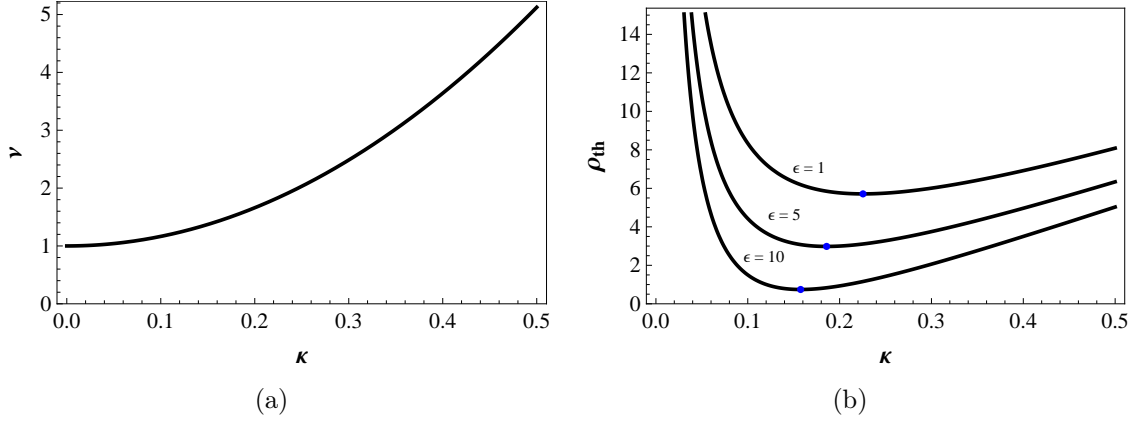


Figure 4.6. (a) Plot of the EIC dispersion relation for $T_r \approx 30$. (b) Plot of theoretical ρ_{th} values for various normalized wave amplitudes (again, for $T_r \approx 30$). Blue points represent minimum values of ρ_{th} .

where T_r is the ratio of the electron temperature to the ion temperature (T_e / T_i). By using this expression to relate ν and κ we introduce a degree of physical fidelity into our analysis that would be absent otherwise.

Next we consider self-consistency at its lowest order. We are investigating ion acceleration by beating electrostatic waves; however, in a real plasma, electrostatic waves propagate via perturbations in the electron and ion population. Thus, since all of our analysis up to this point has featured the use of constant wave parameters, we have implicitly assumed that the exciting waves are unaltered by ion dynamics. In reality, this limits the scope of our investigation to relatively small wave amplitudes ($\epsilon \lesssim 10$) [38].

Thus, by combining these limiting criteria with measured electron and ion temperature values, we can come up with a first-order approximation for the value of ρ_{th} in a real plasma. For the purposes of this investigation, we use BWXII temperature data collected by Jorns and Choueiri in 2010 [40]. For a singly-ionized ($Z = 1$) argon plasma, they measured electron and ion temperatures of 3 and 0.1 eV, respectively (thus, $T_r \approx 30$). Given that $T_e \gg T_i$, our expression for the dispersion relation (4.8) is valid. The resulting relationship between ν and κ is plotted in Figure 4.6(a). Note that (consistent with the observations referenced in Chapter 2) EIC waves cannot propagate for $\nu < 1$ ($\omega < \omega_{ci}$).

Now that we have determined the relationship between ν and κ , we combine the dispersion relation with our small-amplitude approximation to determine allowable ρ_{th} values for various wave amplitudes. Figure 4.6(b) features ρ_{th} curves for $\epsilon = 1$,

5, and 10. We clearly see that for a given wave amplitude, there is a corresponding minimum value of ρ_{th} . Given that we are seeking to minimize the stochastic threshold, we will refer to this minimum as the optimum value for ρ_{th} . We clearly see that for the given spectrum of allowable wave amplitude values, the universal optimum occurs for $\varepsilon = 10$. For this wave amplitude, the stochastic threshold is minimized when $\kappa \approx 0.16$ and $\nu \approx 1.47$, yielding an optimal ρ_{th} value of approximately 0.75. In the next section, we use these optimized wave parameters to deduce the specific impulse of the BWT thruster via numerical simulation. Before proceeding, however, we recall that in the $\bar{\rho}_L$ normalization scheme, $\bar{\rho}$ is implicitly equal to one. Thus, for this particular set of physical wave parameters, $\rho_{th} < \bar{\rho}$. This implies that a significant portion of the ion population will undergo stochastic acceleration, which in turn will push trapped ions into the forward-drifting regime while simultaneously enhancing the X velocity of ions that are already-forward-drifting.

4.4 BWT Specific Impulse Estimate

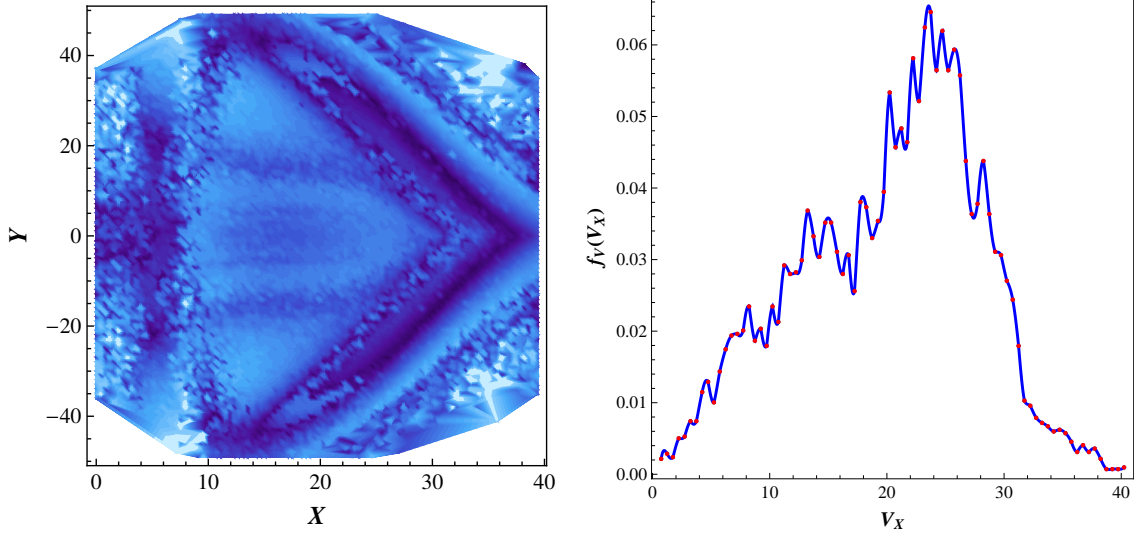
Now that we have determined wave parameters that optimize ρ_{th} for a physical plasma, we can conduct numerical simulations to determine the average exhaust velocity of the BWT thruster in the case of BEW propagation. We follow a procedure similar to that used in Chapter 3 to deduce the exhaust velocity of an unperturbed ensemble in a magnetic slope configuration. To start, we evenly distribute 10,000 ions in the X and Y intervals $[0, 2\pi/\kappa]$ and $[-L, L]$, respectively. Note that the upper bound of the X interval is equal to the normalized wavelength, and was chosen due to the spatial periodicity of the exciting waves. The initial X and Y velocities of each ion are determined by sampling from the Maxwellian described in 3.7. The ensemble is assumed to be collisionless; only single-ion dynamics are considered in simulation. The exit plane is located one wavelength ($2\pi/\kappa$) from the upper bound of the X interval, and ions that breach this plane are considered to be part of the exhaust plume (which in the context of a two-dimensional geometry, is really an exhaust “sheet”). Their instantaneous velocity upon doing so is their exit velocity, denoted by V_X . For each individual ion, we monitor the numerical integration of Hamilton’s equations at each time step to ensure that the ion remains within the Y limits set by the thruster bound L . Ions whose trajectories exceed these bounds are considered lost to the walls. Numerical integration is performed over long timescales to minimize the error

associated with low-velocity particles.

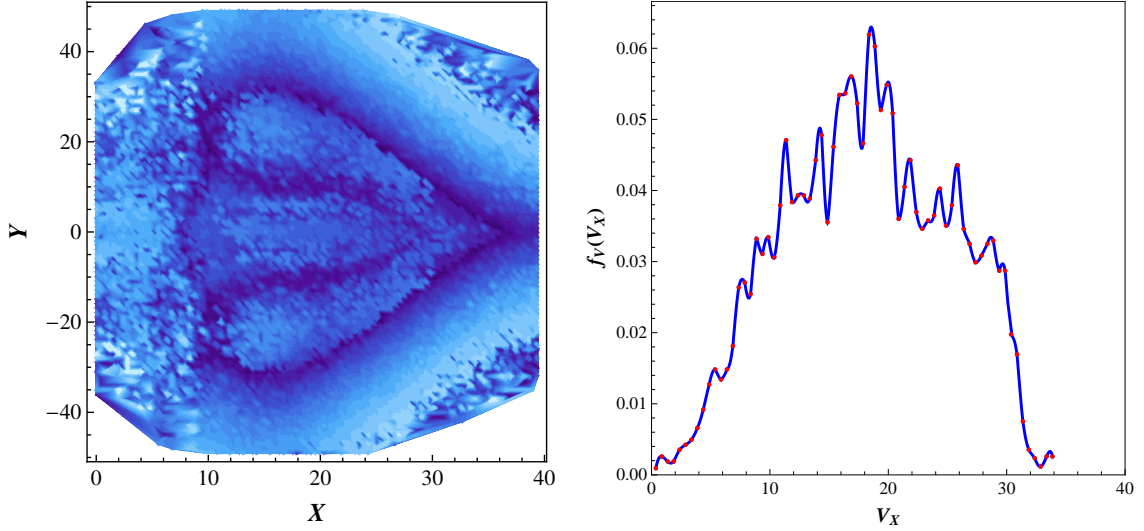
In conducting these simulations, it became immediately clear that the optimized geometry derived in Chapter 3 for the unperturbed case was not readily applicable to the perturbed case. However, this was to be expected for two reasons. In the unperturbed case, a geometry that features a large fraction of particles in the Larmor region is a mark of inefficiency; precessing particles can never break the exit plane of the thruster, and therefore cannot contribute to thrust generation. A principal benefit of BEW propagation, however, is its ability to push particles from Larmor precession into forward-drifting orbits. In the BEW case, the Larmor region can be thought of as a massive reservoir from which particles can be selectively drawn to alter the density of the current flowing along the magnetic null. Thus, a geometry that features a large number of initially-trapped particles is actually desirable (to a degree) in the BEW case. Another reason why the unperturbed optimized geometry is inapplicable in this case has to do with the fundamental nature of the BEW acceleration mechanism. The physical manifestation of BEW acceleration for an ion is a change in its Larmor radius. Upon breaking the stochastic threshold, an ion's Larmor radius dramatically increases and subsequently oscillates chaotically about some mean value greater than ρ_{th} . This notion, coupled with the fact that ions can only be pushed into forward-drifting orbits if they breach the stochastic threshold, implies that the population of forward-drifting ions that results from the introduction of BEW has a relatively large average ρ value. This also implies that while BEW can both increase and enhance flow in the X direction, it can also greatly increase the Y -range swept out by ions as they propagate forward in X . Thus, any BEW propagation in the context of the unperturbed optimized geometry (where $L = 1.6$) that would otherwise enhance current flow just results in an overwhelmingly large percentage of the ions being lost to the walls ($> 95\%$). Thus, a new thruster geometry had to be determined if the simulations were to have any meaning.

For the optimal wave parameters described in 4.3 ($\varepsilon = 10$, $\kappa = 0.16$ and $\nu = 1.47$), numerical investigations of ion trajectories revealed that forward-drifting ions exhibited an upper bound in Y of approximately 50. Thus, we set $L = 50$ in the interests of increasing net ion flow while also decreasing the percentage of ions that collide with the thruster walls.

Figure 4.7 illustrates some of the major results of the simulation. The BEW density plot featured in Figure 4.7(a) depicts an interesting velocity distribution in



(a) Normalized exit velocity density plot (BEW). (b) Normalized exit velocity distribution (BEW).



(c) Normalized exit velocity density plot (SEW). (d) Normalized exit velocity distribution (SEW).

Figure 4.7. The left column features density plots illustrating the spatial distribution of exit velocities for BEW and SEW. Lighter colors indicate regions of higher exit velocity; white areas indicate regions with no forward-drifting ions. The right column features plots of the normalized exit velocity distribution for BEW and SEW. For SEW, $\varepsilon = 10\sqrt{2}$, $\kappa = 0.16$ and $\nu = 1.47$. For BEW, $\varepsilon = 10$, $\kappa = 0.16$ and $\nu_1 = 1.47$. In both cases, $\bar{\delta} = 1/3$.

the X - Y plane. Given that the electrostatic perturbations are defined by a cosine function, at $\tau = 0$ the crests of the wave structure are at the X extremes of the plot, while the trough falls in the middle ($X = \pi/\kappa$). The pure white areas in the corners of the plot indicate regions in which no forward-drifting ions are present; all ions that start in these regions are lost to the walls. We clearly see from the plot that a large percentage of high velocity ions begin in the BEW trough; ions that begin on the far-left crest are generally not accelerated to comparable exit velocities. To first-order, this seems to make intuitive sense. Ions that start in the trough can more easily “catch” (and subsequently “ride”) the electrostatic wave as it propagates forward in X , just as a surfer can more easily catch an ocean wave if he begins in the wave trough and gradually picks up speed (as opposed to starting out near the peak of the wave crest).¹ If we examine the other side of the plot, however, we see a pronounced dark region to the left of the far-right crest that branches out from the magnetic null, forming a symmetric V-structure that looks almost like an oblique shockwave. On average, ions in this region have very low normalized exit velocities (some as low as 0.5). For ions that begin near the null, this behavior can be understood based on the location of the ions relative to the forward-propagating crest of the wave structure. However, for the rest the V, this explanation is not applicable since many of the remaining ions begin fairly close to the trough. One possible explanation is that these ions fall on the back edge of the forward-moving crest *only after they have reached the forward-drifting region*. The timescale for ion channeling clearly increases with the Y distance of an ion from the null, which would explain why the V-structure shoots backward in X . However, further numerical studies are required in order to fully elucidate the physics responsible for the well-defined structure of this density plot.

We pause for a moment to acknowledge the significance of this structure in the context of the single-ion problem. Because the velocity and cyclotron phase angles of all simulated ions are randomly chosen, one would expect the velocity distribution in the X - Y plane to be more chaotic, given that orbit classes are dictated not by X and Y , but rather by Y_{GC} and ρ . In our case, however, while the density plot does feature small regions of randomized velocity values, the majority of the plot is structured and essentially continuous. The reason for this has to do with the relative

¹While the beating behavior of the waves certainly complicates this picture, we will use the simple “surfer” analogy for the purposes of clarity and explanation.

magnitudes of $\bar{\rho}$ and ρ_{th} . In this case, given that $\bar{\rho} > \rho_{th}$, very few ions fall in the regular and forbidden acceleration regions, and thus, very few ions remain trapped in non-forward-drifting orbits upon BEW excitation. As a result, the cyclotron phase angle is likely to be insignificant in the context of BEW acceleration for an arbitrary ion. The well-defined structure of the exit velocity density plot in the X - Y plane is primarily a result of the distance between the ion and the null, and the transport time that it takes for the ion to get there.

Figure 4.7(b) depicts the velocity distribution of ions that breached the exit plane during the course of the simulation. The distribution peaks around 25. The average value of this distribution – which is equal to the normalized exhaust velocity U_{ex} – is approximately 21. For an ion temperature of approximately 0.1 eV, this yields an I_{sp} value of approximately 1500 s for argon. For a hydrogen thruster with the same T_i , the corresponding I_{sp} value is nearly 9500 s. These values clearly represent a vast improvement over the unperturbed configuration, and puts the Beating Wave Thruster in the same I_{sp} range as many existing Hall and ion thruster configurations (see Table 1.3).

Numerical results also indicated that the fraction of ions that break the exit plane (denoted by ξ_{ex}) is approximately 0.837. Note that ξ_{ex} in the perturbed case is essentially equivalent to ξ_f in the unperturbed case. Furthermore, the fraction of ions that escape to the walls of the thruster (ξ_{esc}) in the perturbed case is approximately 0.163. This implies that the percentage of ions that remain trapped in Larmor or reverse-drifting orbits during BEW propagation is $< 0.1\%$. This represents an astronomical increase in efficiency over the unperturbed case (where $\xi_f = \xi_{ex} \approx 0.535$, $\xi_{esc} \approx 0.349$, and the remaining 11.6% of ions were trapped in non-forward-drifting orbits). Thus, it is clear from these numerical results that BEW acceleration appreciably increases – and enhances – the net flow of ions in the X direction along the magnetic null.

For the purpose of comparison, Figure 4.7 also depicts the results of a simulation featuring SEW propagation for equal energy densities. The exit velocity density plot featured in Figure 4.7(c) possesses a similarly well-defined structure as the corresponding BEW plot. However, the dark (low-velocity) regions are not as pronounced and exhibit an interesting looped structure such that they actually pervade the middle of the plot. Furthermore, the lightest regions appear near the magnetic null at the left wave crest, and in the region outlining the low-velocity contour. Again, we concede that in order to fully understand this plot and its potential implications, further nu-

merical studies are required. An examination of the exit velocity distribution featured in Figure 4.7(d) reveals a clear shift in both the peak and mean values of V_X . While the distribution peaks around 19, the average exhaust velocity U_{ex} is approximately 18. Furthermore, there are noticeably fewer high-velocity particles ($V_X \gtrsim 30$) in the SEW case as compared to the BEW case. Numerical results reveal that for SEW, $\xi_{ex} \approx 0.850$ and $\xi_{esc} \approx 0.150$. These values are comparable to the corresponding BEW results. This makes sense given that the theoretical benefit of BEW over SEW in the context of wall loss minimization is due to the existence of a regular acceleration region. However, given the relative magnitudes of $\bar{\rho}$ and ρ_{th} , the regular acceleration region is negligibly small in this case; thus, for the chosen wave parameters, BEW and SEW propagation result in comparable levels of ion channeling.

From U_{ex} , we can calculate theoretical specific impulse values for the single wave case. Using the same plasma parameters that we used to calculate BEW I_{sp} , the corresponding SEW I_{sp} values for argon and hydrogen fuel are 1275 s and 8000 s. These values represent a 15% decrease in I_{sp} relative to BEW levels for equal energy densities.

Thus, in the context of the chosen wave parameters, while BEW and SEW result in similar wall losses, beating wave propagation results in a higher exhaust velocity (and thus, I_{sp}). Since the stochastic threshold ρ_{th} is so low relative to $\bar{\rho}$ (such that the regular acceleration is negligibly small), these results suggest that BEW acceleration may feature a more effective stochastic acceleration process than SEW. This is yet another topic of potential further theoretical investigation.

4.5 Optimization Procedure

The L value that was used in this particular simulation was determined based on a combination of intuition and small-scale investigation of ion trajectories. In this section, however, we consider a potential procedure for optimizing the BWT geometry so as to maximize thruster performance.

First, it is clear that to minimize wall losses, it is desirable for $L > |Y_{UB}|$, where $|Y_{UB}|$ is the approximate upper Y bound of forward-drifting ion trajectories for a given set of wave parameters. Furthermore, given that BEW acceleration (like its SEW counterpart) has an upper bound in ρ (ρ_{UB}), it is obvious that L cannot be made arbitrarily large, otherwise particles near the walls would never be able to reach

the magnetic null (for a collisionless plasma). However, given that BEW stochastic acceleration also causes a net shift in the guiding center towards the magnetic null, this implies that a particle with $|Y_{GC}| > \rho_{UB}$ can still potentially reach the null and be pushed into the forward-drifting region. We will refer to the maximum $|Y_{GC}|$ value for which this phenomenon occurs as $|Y_{GC,max}|$. From these observations, we conclude that while $L > |Y_{UB}|$ will help to significantly minimize walls losses, the optimal L value (in terms of the total number of ions that can be pushed into forward-drifting orbits via BEW propagation) for the perturbed case lies somewhere in the vicinity of $|Y_{GC,max}|$ (which numerical results reveal tends to be much larger than $|Y_{UB}|$). However, in order to determine the actual optimum geometry for a given pair of beating waves, we need explicit expressions for both $|Y_{UB}|$ and $|Y_{GC,max}|$, neither of which have been (accurately) theoretically defined. Thus, further developments in this area would allow us to effectively optimize BWT geometry from the standpoint of both mass flow (thrust generation) and wall loss minimization.

4.6 BWT Thrust Estimate

Recall the linear thrust density equation derived in Chapter 3:

$$\frac{T}{\ell} = 2^{5/2} (\xi_{ex} L_{max} U_{ex}^2) \frac{n \sqrt{m} (k_B T_i)^{3/2}}{q B_0} \quad (3.35)$$

where we have replaced ξ_f with ξ_{ex} . Citing the figures reported in the previous section ($L_{max} = 50$, $U_{ex} = 21$, and $\xi_{ex} = 0.837$), we can use this expression to calculate theoretical thrust values for the Beating Wave Thruster. If we again assume that $n \approx 10^{10} \text{ cm}^{-3}$, $T_i \approx 0.1 \text{ eV}$, and $B_0 \approx 500 \text{ Gauss}$, the approximate thrust densities for argon and hydrogen are 0.07 N/m and 0.01 N/m , respectively (the corresponding SEW thrust densities are nearly 30% smaller). Not only does this represent a significant improvement over unperturbed thrust levels, but it also indicates that from the perspective of thrust generation, the Beating Wave Thruster can compete with many existing (and currently operational) ion and Hall thruster configurations [2]. Thus, while these thrust values are approximate, they are encouraging nonetheless.

From 3.35, we can see how thrust density scales with various plasma parameters. For a given pair of beating waves and a fixed (normalized) thruster geometry (i.e. fixed ξ_{ex} , L_{max} , and U_{ex}), we see that there are several ways to increase the thrust

density of the BWT. In choosing a fuel to maximize thrust, high ion mass and low ion charge are desirable. However, we see from the definition of u_{ex} :

$$u_{ex} = U_{ex} \sqrt{\frac{2k_B T_i}{m}} \quad (4.9)$$

that greater ion mass also results in reduced exhaust velocity (and thus, reduced I_{sp}). Thus, in terms of fuel selection, there is a clear tradeoff between thrust density and specific impulse.

Another way of increasing BWT thrust density is to increase the ion density n . However, as will be discussed briefly in Chapter 5, there is an upper limit to the allowable ion density for a given ion temperature due to the potentially negative effects of collisional processes on thruster performance.

Thrust density will also increase in response to decreasing B_0 (the magnitude of the magnetic field in the homogeneous regions); however, this will also increase the geometric scale of the thruster (since all lengths are normalized by $\bar{\rho}_L$ and $\bar{\rho}_L \propto B_0^{-1}$).

And finally, we can also increase BWT thrust density by increasing the ion temperature T_i . By (3.35) (and for fixed wave parameters), this is the most efficient way to increase the thrust, since $T / \ell \propto T_i^{3/2}$. Increasing the ion temperature would also increase the thruster scale, but to a much lesser extent (since $\bar{\rho}_L \propto \sqrt{T_i}$). Furthermore, we see from (4.9) that u_{ex} is also proportional to $\sqrt{T_i}$. Thus, by increasing the ion temperature of the plasma, we can increase both the thrust *and* the specific impulse of the BWT.

4.7 Summary of Results

In this chapter, we have effectively demonstrated via numerical simulation and subsequent calculations that BEW propagation increases both the velocity and density of the linear ion current that forms along the null of a steeply-sloped rectilinear magnetic field for a thermalized ion ensemble. We have also demonstrated that the “ion channeling” characteristic of BEW acceleration helps to mitigate walls losses that plague other electric thrusters. Theoretical specific impulse and thrust density values strongly indicate that BEW direct ion acceleration is an effective propulsion mechanism, and therefore, that the Beating Wave Thruster has significant potential as a future electric propulsion device.

Chapter 5

Conclusions and Future Work

In this chapter, we summarize the major findings of this thesis, and conclude with a brief discussion of open questions and future work.

5.1 Conclusions

The goal of this thesis was to demonstrate the feasibility and validity of a new plasma propulsion concept that uses beating electrostatic waves to augment the linear ion current generated by a thermalized ion ensemble in a rectilinear magnetic slope geometry. Many things were discovered while pursuing this end goal: some were directly related, and some were more peripheral.

Early on, an inconsistency was found between the analytical and actual upper bounds of the stochastic region for SEW acceleration, indicating the need for further theoretical development in that area. After the introduction of the magnetic slope topography, the analysis of unperturbed single-ion dynamics was rehashed and corrected, orbit domains were clearly illustrated, and the analysis was extended to a thermalized ion ensemble via numerical simulation. Optimal unperturbed thruster configurations were numerically deduced under two normalization schemes, and simulation results unambiguously indicated that a rectilinear, steeply-sloped magnetic field does indeed produce a net linear ion current that flows along the magnetic null. Benchmark specific impulse and thrust density values were determined, and unperturbed thruster performance was shown to be very poor. After the introduction of the perturbed case, an investigation of ion dynamics for $\varepsilon \neq 0$ was conducted that expanded on the previous work of Jorns and Choueiri [1]. It was shown that stochastic acceleration was required in order for trapped ions to be pushed into forward-drifting

orbits, and that already-forward-drifting ions were often decelerated if $\rho_0 < \rho_{th}$. The “ion channeling” phenomenon was demonstrated numerically, in which stochastic ions are preferentially transported away from the thruster walls and towards the magnetic null. It was ultimately deduced that to a large degree, the magnitude ρ_{th} essentially dictates thruster performance. The EIC dispersion relation was then introduced and wave amplitudes were limited to preclude self-consistent effects. Optimal wave parameters were determined, and subsequent numerical simulations featuring both single and beating electrostatic wave propagation were conducted to deduce resulting thruster characteristics. It was ultimately demonstrated that (for the given wave parameters) while SEW and BEW performed similarly in terms of wall loss minimization, BEW was superior in both thrust generation and specific impulse. The BWT was thus shown to possess specific impulse and thrust levels comparable to existing ion and Hall thruster configurations (for argon, $I_{sp} \approx 1500$ s and $T/\ell \approx 0.07$ N/m). Nearly 85% of ions were shown to contribute to the BWT exhaust plume, while only 15% of the initial ion population was shown to escape to the thruster walls.

Based on these preliminary results, it is reasonable to assert that the BWT concept has the potential to form the basis of a new class of electrodeless, efficient, and variable electric thruster that rivals – and could potentially surpass – the performance of operational ion and Hall thrusters. Thus, the further investigation and optimization of this novel ion acceleration mechanism could be the next step in Man’s ongoing journey to conquer curiosity, expand human possibility, and navigate the yet-uncharted waters of the final frontier – space.

5.2 Future Work

While this thesis accomplished its main goal, there is still much future work to be done regarding both the Beating Wave Thruster concept and BEW acceleration in general. Our discussion is split into three separate categories: continued theoretical development, simulation improvements, and proof-of-concept demonstration.

5.2.1 Continued Theoretical Development

As aforementioned, there is still much theoretical work to be done that relates to BEW acceleration, both in general and in the context of a steeply-sloped magnetic

field. Important topics of future investigation include (but are certainly not limited to): determining an accurate expression for ρ_{UB} (the upper bound of the stochastic region) in the BEW case, deriving an expression for $|Y_{UB}|$ (the upper bound of Y motion for perturbed forward-drifting trajectories), determining accurate analytical expressions that relate thrust and specific impulse to wave and plasma parameters, defining the theoretical power requirement for thruster operation at a given amplitude and frequency, elucidating the mechanism by which thrust is actually transferred to the spacecraft, investigating magnetic detachment of the plume upon breaching the exit plane, and determining an optimized thruster geometry for the BWT system.

5.2.2 Simulation Improvements

The simulation utilized to determine specific impulse and thrust estimates for the BWT thruster features small-amplitude waves with time-independent wave parameters, and only considers single-ion dynamics in the context of a collisionless ensemble. While clearly not entirely physical, this model still yields a numerical estimate of the thrust and specific impulse levels that we can expect from an actual Beating Wave Thruster. Furthermore, it also gives us some important insight into the behavior of an ion ensemble in the presence of a magnetic slope and BEW propagation. However, several additional elements can be introduced into the simulated system to increase its physical fidelity (and therefore, its accuracy), all of which also greatly increase the total computation time required to complete a given simulation. These improvements are described briefly below.

Collisions

The next logical step in simulating an ensemble of ions is to introduce particle interactions in the form of ion-ion collisions. Spektor outlines a comparatively simple method for simulating collisions in his doctoral dissertation [10]. In the context of BEW acceleration, an important quantity to consider when evaluating the effects of collisions on ensemble behavior is the Hall parameter, which is defined as the ratio of the gyrofrequency to the collision frequency [2]:

$$\beta = \frac{\omega_{ci}}{\nu_c} \quad (5.1)$$

Since the BWT thruster concept exploits the Larmor motion of particles to produce

a linear ion current, we conclude that if $\beta < 1$, in all likelihood, the effectiveness of the BWT thruster will decrease dramatically. For ion-ion collisions, the collision frequency ν_i goes as $n_i T_i^{-3/2}$ (where n_i is the ion density) [41]. Thus, for a given plasma (i.e. fixed ion charge and mass), we can increase the Hall parameter by increasing the magnitude of the magnetic field, decreasing the ion density, and/or increasing the ion temperature.

Multiple Species

After collision implementation, the next step towards physical fidelity is introducing a second species into the system: electrons. As one might expect, the inclusion of electrons immensely complicates particle dynamics. Thus, Particle-in-Cell (PIC) codes (which are generally much more complex than the Monte Carlo methods featured in this thesis) may be necessary in order to accurately capture two-species ensemble behavior [42]. However, despite the difficulties associated with including a second species in our analysis, the benefits are many. One particularly important topic that can be investigated via PIC simulations is plume neutrality. Jorns and Choueiri theorized that the ejection of ions from the end of the thruster geometry would create an ambipolar electric field of sufficient strength to drag the electron population with it, thereby ensuring the quasi-neutrality of the exhaust [1]. However, while BEW acceleration causes a linear ion current to propagate in the positive X direction, it also simultaneously causes a linear electron current to flow in the negative X direction. Thus, while one can intuit that electron inclusion will have a negative impact on both BWT thrust and specific impulse values, PIC simulation would provide the numerical evidence necessary to either support or refute this claim.

Self-Consistency

Finally, we can further enhance our numerical simulations by removing the assumption of small-amplitude waves with time-independent wave parameters and considering how perturbations in the ion and electron populations actually alter the properties of the exciting waves as they propagate through the plasma. Since increasing the wave amplitude decreases the time scale on which BEW acceleration occurs, it is likely that these self-consistent simulations will result in even higher values for BWT thrust and specific impulse, given that our analysis was generally limited to small ε ($\lesssim 10$). To

conduct such a numerical investigation on a large scale, however, would likely require a very complex (and hopefully very efficient) base code, coupled with immense computational power (possibly even a supercomputer).

3-D Geometry

Generalization to a three-dimensional (as opposed to a two-dimensional) thruster geometry – which we have assumed in all prior analysis – is yet another potential improvement that can be tacked on to our baseline simulation. This dimensional expansion would allow us to investigate fringe effects and plume characteristics after it has been ejected from the thruster.

5.2.3 Proof-of-Concept Demonstration

Preliminary simulation has clearly shown that the BWT has potential as an electric propulsion concept. Thus, while developing BEW theory and simulation architecture is very important, so is the demonstration of BWT performance in a laboratory setting. Thus, a proof-of-concept experiment is a critical next step in the actual development of BWT technology. It is our intention to adapt BWXII for this very purpose.

One of the most important aspects of the proof-of-concept experiment is going to be the accurate reproduction of a steeply-sloped magnetic field within the vacuum chamber. In their original paper, Jorns and Choueiri proposed a thruster design that featured the use of two parallel current sheets to produce the desired magnetic field (see Figure 5.1(a)) [38]. However, this design is insufficient. While finite current sheets would indeed produce a magnetic slope, the slope would be extremely shallow and occupy the vast majority of the span between the two plates. This becomes apparent when one takes the limit of very large plates, since the magnetic field between two infinite current sheets with parallel currents is identically zero. Thus, since the BWT concept calls for a steep magnetic slope, the current sheet geometry is not applicable when trying to reproduce the idealized field configuration used in our previous analysis.

One simple configuration that can effectively reproduce the necessary field configuration to a very good approximation is featured in Figure 5.1. An antisymmetric arrangement of current loops (or Helmholtz coils) is shown at the $x = 0$ cross-section

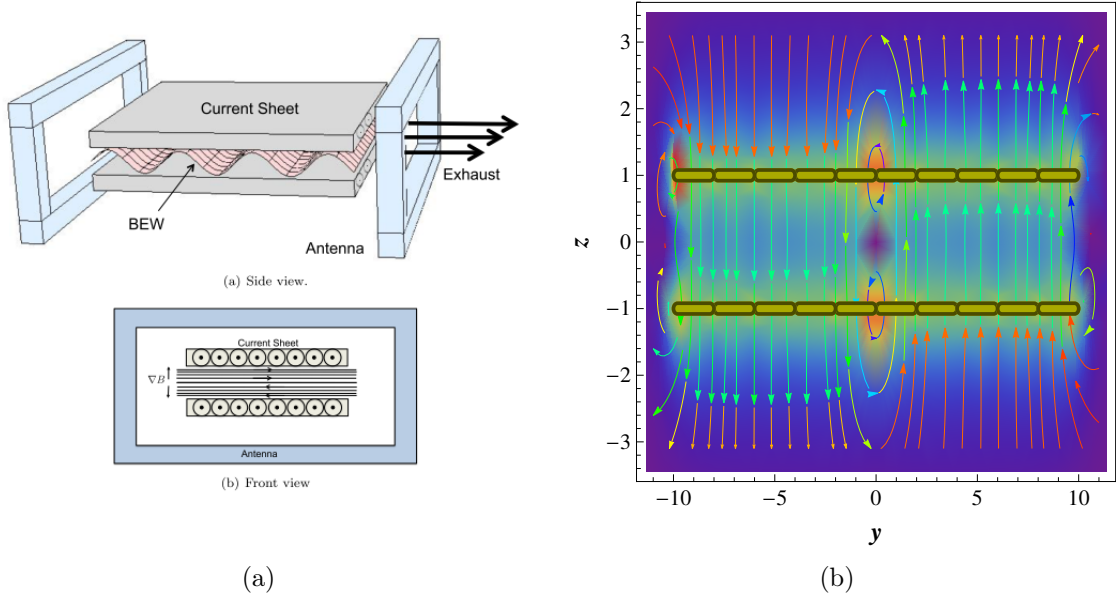


Figure 5.1. (a) Originally proposed configuration featuring the use of two current sheets to produce a sloped magnetic field (taken from Ref. [38]). However, this design does not result in a steep magnetic slope. (b) Magnetic field vector and density plot for an antisymmetric configuration of current loops. By inspection, we see that for a given z -value between -1 and 1, the field is approximately homogeneous for $1 < |y| < 9$, features a magnetic null at $y = 0$, and is steeply-sloped in the interval $|y| < 1$. The positive x -axis (and thus, the direction of the net ion current) points out of the page.

of the y - z plane. Axial vectors of each current loop point in the z -direction. Loops in quadrants I and IV have current flowing in one direction; loops in quadrants II and III have current flowing in the opposite direction. This produces a magnetic field with two near-homogeneous regions of opposite polarity, and a magnetic null (coupled with a sharp magnetic slope) at their interface. Linear ion current flows out of the page in the positive x -direction.

A sampling of field magnitudes along $z = 0$ was taken to deduce field dependence on y . Parameters were scaled appropriately in an attempt to match the theoretical field described by (3.5). Figure 5.2 features a plot of the numerical data deduced from the above sampling, as well as the hyperbolic tangent field profile described by (3.5) for $B_0 = \delta = 1$. Aside from minor field oscillations and fringe effects at large y , the current loop field matches the theoretical field very well, suggesting that this simple current loop configuration could be an effective way of producing the desired field in a laboratory setting. Furthermore, while permanent magnets could be used to produce a similar magnetic field topography, the use of current loops allows for

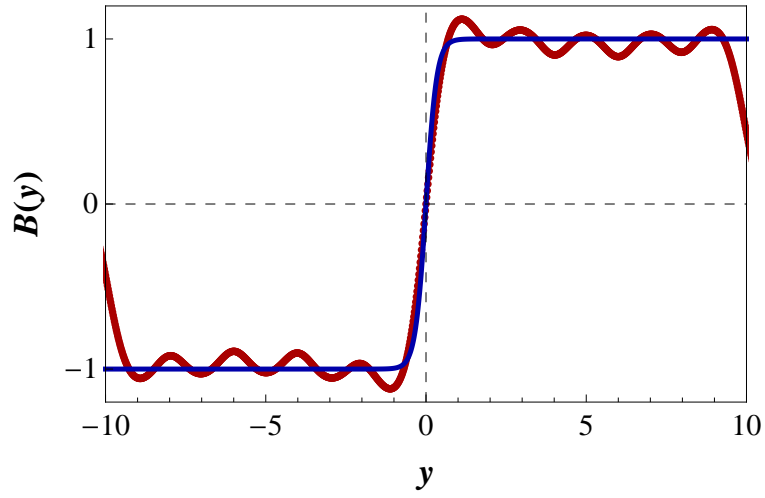


Figure 5.2. Magnetic field for the above current loop configuration along $z = 0$ (red curve). The blue curve is a theoretical field (3.5) with $B_0 = \delta = 1$.

B-field tuning (and thus the adjustment of grad-B in the sloped region) since $B \propto I$. Once BWT thrust and I_{sp} levels have been successfully measured in the laboratory, they can be used to cross-check the theory developed both in this thesis and in the seminal paper of Jorns and Choueiri [1], and ultimately, to spur the development of an actual thruster design.

Appendix A

Hamiltonian Mechanics

Here we conduct a general review of Hamiltonian mechanics for a classical system, and briefly describe the numerical methods used to solve Hamilton's equations in the context of this thesis.

A.1 The Hamiltonian Formulation

We begin our discussion of the Hamiltonian formulation by defining the Lagrangian of a classical system:

$$\mathcal{L} = T(\mathbf{q}, \dot{\mathbf{q}}, t) - V(\mathbf{q}, \dot{\mathbf{q}}, t) \quad (\text{A.1})$$

where T and V are the kinetic and potential energy of the system, respectively, and q is a generalized coordinate vector. Using this Lagrangian, we define a corresponding generalized momentum vector as follows:

$$\mathbf{p} = \frac{\partial \mathcal{L}}{\partial \dot{\mathbf{q}}} = \nabla_{\dot{\mathbf{q}}} \mathcal{L} \quad (\text{A.2})$$

where $\nabla_{\dot{\mathbf{q}}}$ denotes the gradient with respect to $\dot{\mathbf{q}}$.

The Hamiltonian of a classical system is defined as the Legendre transform of the Lagrangian:

$$h = \dot{\mathbf{q}} \cdot \mathbf{p} - \mathcal{L}$$

where \mathbf{q} and \mathbf{p} are the generalized coordinate and momentum vectors, respectively.

The time evolution of a system with Hamiltonian h is described by Hamilton's equations as follows:

$$\dot{\mathbf{p}} = -\nabla_{\mathbf{q}}h \qquad \dot{\mathbf{q}} = \nabla_{\mathbf{p}}h \qquad (\text{A.3})$$

For a n -dimensional system, (A.3) defines a set of $2n$ first-order differential equations that can be solved simultaneously (provided that $2n$ initial conditions have also been specified).

A.2 Numerical Methods

For all Hamiltonians derived in this thesis (see Appendix B), Hamilton's equations are analytically intractable and must be solved using numerical methods.

The phase space of a Hamiltonian system is a symplectic manifold that possesses a natural symplectic structure in the canonically conjugate coordinates [43]. This manifold possesses the symplectic two-form $\omega = dp \wedge dq$ (which explains the anti-symmetric nature of Hamilton's equations). Physically, this two-form represents the oriented phase space area. The time evolution of a Hamiltonian system (also called Hamiltonian flow) leaves the symplectic two-form invariant [44, 45]. Thus, if we want to obtain accurate numerical solutions to Hamilton's equations, it is clearly desirable to use an integration algorithm that also preserves ω [46, 47].

A numerical integration algorithm that exactly preserves the two-form ω is called a symplectic integrator. These integrators are advantageous for solving Hamilton's equations not only because they preserve the inherent phase space structure of a Hamiltonian system, but also because they have been shown to possess long-time stability [47]. Symplectic integrators can be either explicit or implicit.¹ Both types were used in the context of this thesis. The cases in which they were used are outlined briefly in the subsections to follow.

¹Explicit numerical integration methods determine the future state of a system solely from its current state. Implicit methods determine the state of a system by considering the current and future states simultaneously. As a result, explicit integration algorithms tend to be comparatively more efficient [48].

A.2.1 Separable Case

A Hamiltonian is separable if it can be written in the following form:

$$h = T(\mathbf{p}) + V(\mathbf{q}) \quad (\text{A.4})$$

This “decoupling” of \mathbf{p} and \mathbf{q} implies that an explicit symplectic integrator can be used to accurately and efficiently determine the time evolution of the system [49]. As such, for all of the one-dimensional separable Hamiltonians featured in Chapter 2, a fourth-order symplectic partitioned Runge-Kutta numerical integration algorithm was used to solve Hamilton’s equations and construct the Poincaré sections that elucidated magnetized ion behavior in the presence of propagating electrostatic waves.

A.2.2 Nonseparable Case

In the nonseparable case, the Hamiltonian cannot be written in the previous form. As a result, \mathbf{p} and \mathbf{q} are indeed coupled, and implicit symplectic methods must be used to determine the time evolution of the system. Thus, for all Hamiltonians involving a y -dependent vector potential, a fourth-order fixed-step implicit Runge-Kutta Gauss method was used to numerically solve Hamilton’s equations.

Appendix B

Derivation of the Hamiltonian

Here we derive the Hamiltonian for a magnetized ion subject to a spectrum of electrostatic waves propagating in the x -direction. Several magnetic field configurations and normalization schemes are considered.

B.1 Arbitrary B-field

Consider an ion of mass m and charge q in an electromagnetic field. The Lagrangian is

$$\mathcal{L} = \frac{1}{2}m\dot{\mathbf{x}}^2 + q\mathbf{A} \cdot \dot{\mathbf{x}} - q\phi \quad (\text{B.1})$$

where \mathbf{x} is the position vector of the particle, \mathbf{A} is the magnetic vector potential, and ϕ is the electrostatic potential [50]. The canonical momenta are

$$p_i = \frac{\partial \mathcal{L}}{\partial \dot{x}_i} = m\dot{x}_i + qA_i \quad (\text{B.2})$$

We recall from Appendix A that the Hamiltonian is defined as the Legendre transform of the Lagrangian:

$$h = \dot{\mathbf{x}} \cdot \mathbf{p} - \mathcal{L}$$

Thus, in terms of the generalized coordinates and momenta:

$$h = \frac{1}{2m}(\mathbf{p} - q\mathbf{A})^2 + q\phi \quad (\text{B.3})$$

Next, we consider a spectrum of propagating electrostatic waves defined by

$$\mathbf{E} = \sum_{i=1}^n E_{0,i} \sin(k_i x - \omega_i t + \varphi_i) \hat{x} \quad (\text{B.4})$$

The corresponding electrostatic potential must satisfy $\nabla\phi = -\mathbf{E}$. Thus,

$$\phi = \sum_{i=1}^n \frac{E_{0,i}}{k_i} \cos(k_i x - \omega_i t + \varphi_i) \quad (\text{B.5})$$

We then set $k_1 = k_2 = k$, $E_{0,1} = E_{0,2} = E_0$, and $\varphi_1 = \varphi_2 = 0$ to simplify our analyses. This yields the following expression for the Hamiltonian of a generally-magnetized ion subject to a spectrum of electrostatic waves propagating in the x -direction:

$$h = \frac{1}{2m} (\mathbf{p} - q\mathbf{A})^2 + \frac{qE_0}{k} \sum_{i=1}^n \cos(kx - \omega_i t) \quad (\text{B.6})$$

Clearly, $n = 1$ in the SEW case. In the BEW case, $n = 2$ and ω_1 and ω_2 are related by the beating criterion in (2.1).

B.2 Rectilinear (z -directed) B-field

Here we specialize the general Hamiltonian (B.6) by defining a z -directed magnetic field. Three cases are considered. In Case 1, the B-field is uniform. In Case 2, the B-field is y -dependent. In Case 3, the B-field is x - and y -dependent.

B.2.1 Case 1: UNIFORM

In this case,

$$\mathbf{B} = B_0 \hat{z} \quad (\text{B.7})$$

The magnetic vector potential \mathbf{A} must satisfy the relation $\nabla \times \mathbf{A} = \mathbf{B}$. Thus, without loss of generality, we can define a vector potential such that

$$A_x = 0 \quad A_y = \int_0^x B_0 dx' = B_0 x \quad A_z = 0 \quad (\text{B.8})$$

The Hamiltonian then takes the following (scalar) form:

$$h = \frac{1}{2m} \left(p_x^2 + [p_y - qB_0x]^2 \right) + \frac{qE_0}{k} \sum_{i=1}^n \cos(kx - \omega_i t) \quad (\text{B.9})$$

Since y is an ignorable coordinate, p_y is invariant. Without loss of generality, we choose $p_y = 0$ to simplify subsequent calculations. The expression for the Hamiltonian then becomes

$$h = \frac{1}{2m} \left(p_x^2 + q^2 B_0^2 x^2 \right) + \frac{qE_0}{k} \sum_{i=1}^n \cos(kx - \omega_i t) \quad (2.2)$$

Because this Hamiltonian is separable, we can use explicit symplectic integration to efficiently generate accurate Poincaré sections of particle motion. As demonstrated in Chapter 2, these plots offer direct insight into the acceleration mechanism, and serve as the foundation for much of the theory surrounding electrostatic wave acceleration.

B.2.2 Case 2: y -DEPENDENCE

In this case,

$$\mathbf{B} = B(y)\hat{z} \quad (\text{B.10})$$

Without loss of generality, we can define a vector potential such that

$$A_x = - \int_0^y B(y') dy' \equiv A_x(y) \quad A_y = 0 \quad A_z = 0 \quad (\text{B.11})$$

The Hamiltonian then assumes the form

$$h = \frac{1}{2m} \left([p_x - qA_x(y)]^2 + p_y^2 + p_z^2 \right) + \frac{qE_0}{k} \sum_{i=1}^n \cos(kx - \omega_i t) \quad (\text{B.12})$$

Since z is an ignorable coordinate, p_z is invariant and can be dropped from (B.13) without affecting the remaining equations of motion. The expression for the Hamiltonian then becomes

$$h = \frac{1}{2m} \left([p_x - qA_x(y)]^2 + p_y^2 \right) + \frac{qE_0}{k} \sum_{i=1}^n \cos(kx - \omega_i t) \quad (\text{B.13})$$

B.2.3 Case 3: x - AND y -DEPENDENCE

In this case,

$$\mathbf{B} = B(x, y)\hat{z} \quad (\text{B.14})$$

Without loss of generality, we can define a vector potential such that

$$A_x = - \int_0^y B(x, y') dy' \equiv A_x(x, y) \quad A_y = \int_0^x B(x', y) dx' \equiv A_y(x, y) \quad A_z = 0 \quad (\text{B.15})$$

After dropping p_z by the same argument as in the previous section, the Hamiltonian takes the scalar form

$$h = \frac{1}{2m} \left([p_x - qA_x(x, y)]^2 + [p_y - qA_y(x, y)]^2 \right) + \frac{qE_0}{k} \sum_{i=1}^n \cos(kx - \omega_i t) \quad (\text{B.16})$$

Note that (B.13) is just a special case of (B.16) with $A_x(x, y) = A_x(y)$ and $A_y(x, y) = 0$.

B.3 Canonical Transformations

It is often convenient to nondimensionalize the Hamiltonian – along with its generalized coordinates and momenta – in order to simplify subsequent analysis. This can be accomplished via canonical transformation. By expressing the Hamiltonian (and by extension, Hamilton's equations) in nondimensional form, we are free to conduct generalizable numerical studies of particle motion. We need not specify the cyclotron frequency or the particle mass (for example) in order to deduce characteristic ion behavior. By choosing different normalization parameters, we can characterize several nondimensional Hamiltonian formulations, each of which is useful in a particular context of analysis.

To start, we take the untransformed Hamiltonian h to be defined by (B.16) since it is more general than (B.13). In all of the following transformations, variables with time units are normalized by the ion cyclotron frequency $\omega_{ci} = qB_0/m$ in regions of

constant magnetic field. Transformed Hamiltonians are denoted by \mathcal{H} with a subscript indicating the parameter used to normalize variables with units of length.

Normalization by Wave Number k

When studying single particle motion, it is convenient to normalize translational variables by the wave number k . The transformed Hamiltonian \mathcal{H}_k takes the following form:

$$\mathcal{H}_k = \frac{1}{2} \left([P_X - \bar{A}_X]^2 + [P_Y - \bar{A}_Y]^2 \right) + \varepsilon \sum_{i=1}^n \cos(X - \nu_i \tau) \quad (\text{B.17})$$

where

$$\begin{aligned} \mathcal{H}_k &= \frac{k^2}{m\omega_{ci}^2} h & \tau &= \omega_{ci} t & \nu_i &= \frac{\omega_i}{\omega_{ci}} & \varepsilon &= \frac{qkE_0}{m\omega_{ci}^2} \\ X &= kx & Y &= ky & \bar{A}_X &= \frac{qk}{m\omega_{ci}} A_x(X/k, Y/k) & \bar{A}_Y &= \frac{qk}{m\omega_{ci}} A_y(X/k, Y/k) \\ P_X &= X' + \bar{A}_X & P_Y &= Y' + \bar{A}_Y \end{aligned}$$

The prime ($'$) denotes the derivative with respect to the normalized time variable τ .

Normalization by RMS Larmor Radius $\bar{\rho}_L$

For simulations involving a Maxwellian (thermalized) particle distribution, it is convenient to normalize translational variables by the root-mean-square Larmor radius $\bar{\rho}_L$ of the ensemble (see Appendix C for a more detailed discussion of thermalized distributions in the context of this thesis). The transformed Hamiltonian $\mathcal{H}_{\bar{\rho}_L}$ then takes the form

$$\mathcal{H}_{\bar{\rho}_L} = \frac{1}{2} \left([P_X - \bar{A}_X]^2 + [P_Y - \bar{A}_Y]^2 \right) + \frac{\varepsilon}{\kappa} \sum_{i=1}^n \cos(\kappa X - \nu_i \tau) \quad (\text{B.18})$$

where

$$\mathcal{H}_{\bar{\rho}_L} = \frac{1}{m\omega_{ci}^2 \bar{\rho}_L^2} h \quad \tau = \omega_{ci} t \quad \nu_i = \frac{\omega_i}{\omega_{ci}} \quad \kappa = k\bar{\rho}_L \quad \varepsilon = \frac{qE_0}{m\omega_{ci}^2 \bar{\rho}_L}$$

$$X = \frac{x}{\bar{\rho}_L} \quad Y = \frac{y}{\bar{\rho}_L} \quad \bar{A}_X = \frac{q}{m\omega_{ci}\bar{\rho}_L} A_x(\bar{\rho}_L X, \bar{\rho}_L Y) \quad \bar{A}_Y = \frac{q}{m\omega_{ci}\bar{\rho}_L} A_y(\bar{\rho}_L X, \bar{\rho}_L Y)$$

$$P_X = X' + \bar{A}_X \quad P_Y = Y' + \bar{A}_Y$$

This formulation is advantageous because it allows us to conduct large-scale numerical simulations on a thermalized ensemble without needing to specify a fixed temperature value. However, since we have introduced an exogenous quantity ($\bar{\rho}_L$) into the Hamiltonian, we must instead specify a value for the normalized wave number κ in order to ensure that the system is not underdetermined.

Action-Angle Coordinates

The one-dimensional Hamiltonian (2.2) can also be expressed in terms of action-angle coordinates. This transformation yields the following expression after wave number normalization:

$$\bar{\mathcal{H}}_k = I + \varepsilon \sum_{i=1}^n \cos(\rho \sin \theta - \nu_i \tau) \quad (\text{B.19})$$

where

$$I = \frac{\rho^2}{2} = \frac{1}{2}(X'^2 + X^2) \quad \text{and} \quad \rho = \frac{X}{\sin \theta} = \frac{X'}{\cos \theta}$$

In this formulation, ρ is the k -normalized Larmor radius and θ is the cyclotron phase angle of the particle (measured clockwise from the $+Y$ -axis in the X - Y plane).

RMS Larmor radius normalization yields a predictably similar Hamiltonian:

$$\bar{\mathcal{H}}_{\bar{\rho}_L} = I + \frac{\varepsilon}{\kappa} \sum_{i=1}^n \cos(\kappa \rho \sin \theta - \nu_i \tau) \quad (\text{B.20})$$

where ρ is now normalized by the root-mean-square Larmor radius of a thermalized ensemble. Note that in the context of this normalization scheme, the RMS value of the normalized Larmor radius – denoted by $\bar{\rho}$ – is just equal to one.

Appendix C

Maxwellian Distributions

In the context of this thesis, all numerical simulations implicitly assume that the initial speed distribution of a given ion ensemble is described by a two-dimensional Maxwellian [51]:

$$f_v(v) dv = \frac{mv}{k_B T_i} \exp \left[\frac{-mv^2}{2k_B T_i} \right] dv \quad (\text{C.1})$$

where v is ion speed, m is the ion mass, T_i is the ion temperature, and k_B is Boltzmann's constant. Note that $v^2 = \sum v_i^2$, where v_i are the ion velocity components. The RMS speed of this distribution is defined by

$$\bar{v} = \sqrt{\frac{2k_B T_i}{m}} \quad (\text{C.2})$$

Furthermore, the distribution of a given velocity component v_i is a simple Gaussian:

$$f_v(v_i) dv_i = \sqrt{\frac{m}{2\pi k_B T_i}} \exp \left[\frac{-mv_i^2}{2k_B T_i} \right] dv_i \quad (\text{C.3})$$

In terms of \bar{v} , (C.3) takes the following form:

$$f_v(v_i) dv_i = \frac{1}{\bar{v}\sqrt{\pi}} \exp \left[-\frac{v_i^2}{\bar{v}^2} \right] dv_i \quad (\text{C.4})$$

Next, in order to integrate such a distribution into our formulations of the Hamiltonian and Hamilton's equations, we express the velocity distribution in terms of normalized parameters.

Normalization by k

In terms of k -normalized parameters, the velocity distribution can be expressed as follows:

$$f_v(v_i) dv_i = f_V(V_i) dV_i = \frac{1}{\bar{V}\sqrt{\pi}} \exp\left[-\frac{V_i^2}{\bar{V}^2}\right] dV_i \quad (\text{C.5})$$

where $V_X = X'$, $V_Y = Y'$, and $\bar{V} = k\bar{v}/\omega_{ci}$. In this normalization scheme, \bar{V} is clearly equal to the normalized RMS Larmor radius $\bar{\rho}$:

$$\bar{\rho} = \sqrt{\langle \rho^2 \rangle} = \sqrt{\langle V_X^2 + V_Y^2 \rangle} = \sqrt{\langle V^2 \rangle} = \bar{V}$$

where $\langle \dots \rangle$ denotes the average value. Thus, we express the velocity distribution in terms of $\bar{\rho}$ as follows:

$$f_V(V_i) dV_i = \frac{1}{\bar{\rho}\sqrt{\pi}} \exp\left[-\frac{V_i^2}{\bar{\rho}^2}\right] dV_i \quad (3.24)$$

This expression defines a normal distribution of velocity component V_i with a mean value μ of zero and a standard deviation σ of $\bar{\rho}/\sqrt{2}$. For simulations involving a k -normalized Hamiltonian, all initial ion velocity component values are sampled from this distribution.

Normalization by $\bar{\rho}_L$

In terms of $\bar{\rho}_L$ -normalized parameters, the velocity distribution is

$$f_v(v_i) dv_i = f_V(V_i) dV_i = \frac{1}{\bar{V}\sqrt{\pi}} \exp\left[-\frac{V_i^2}{\bar{V}^2}\right] dV_i \quad (\text{C.6})$$

where $V_X = X'$, $V_Y = Y'$, and $\bar{V} = \bar{v}/\omega_{ci}\bar{\rho}_L$. But $\bar{\rho}_L = \bar{v}/\omega_{ci}$ by definition; thus, \bar{V} (and by extension, $\bar{\rho}$) is just equal to one. The velocity distribution can then be expressed in the following simplified form:

$$f_V(V_i) dV_i = \frac{1}{\sqrt{\pi}} \exp\left[-V_i^2\right] dV_i \quad (3.28)$$

This expression defines a normal distribution of velocity component V_i with a mean value μ of zero and a standard deviation σ of $1/\sqrt{2}$. All initial ion velocities for simulations involving a $\bar{\rho}_L$ -normalized Hamiltonian are sampled from this distribution.

Note that unlike the k -normalized distribution (which depends on the temperature-dependent parameter $\bar{\rho}$), this distribution is fixed since $\bar{\rho}_L$ normalization universally maps $\bar{\rho}$ to one. This implies that simulations involving $\bar{\rho}_L$ -normalized Hamiltonians are generalizable to all ion temperature values.

Bibliography

- [1] B. Jorns and E. Y. Choueiri, “A Plasma Propulsion Concept Based on Direct Ion Acceleration with Beating Electrostatic Waves,” *American Institute of Aeronautics and Astronautics*, pp. 1–19, 2010.
- [2] R. G. Jahn, *Physics of Electric Propulsion*. Mineola, N.Y.: Dover Publications Inc., 1996.
- [3] H. Arbit, *Combustion characteristics of the fluorine lithium hydrogen tripropellant combination*. New York N.Y.: American Institute of Aeronautics and Astronautics, 1968.
- [4] G. P. Sutton and O. Biblarz, *Rocket Propulsion Elements*. John Wiley and Sons, 2010.
- [5] European Space Agency, “Electric Spacecraft Propulsion,” 2004.
- [6] M. Martinez-Sanchez and J. E. Pollard, “Spacecraft Electric Propulsion – An Overview,” *Journal of Propulsion and Power*, vol. 14, no. 5, pp. 688–699, 1998.
- [7] K. Sankaran, L. Cassady, A. D. Kodys, and E. Y. Choueiri, “A survey of propulsion options for cargo and piloted missions to Mars,” *Annals of the New York Academy of Sciences*, vol. 1017, pp. 450–67, May 2004.
- [8] P. Wilbur, R. Jahn, and F. Curran, “Space electric propulsion plasmas,” *IEEE Transactions on Plasma Science*, vol. 19, no. 6, pp. 1167–1179, 1991.
- [9] E. Ahedo, J. M. Gallardo, and M. Martinez-Sanchez, “Effects of the radial plasma-wall interaction on the Hall thruster discharge,” *Physics of Plasmas*, vol. 10, p. 3397, July 2003.

- [10] R. Spektor, *Ion Energization by a Pair of Beating Electrostatic Waves*. Ph.d., Princeton University, 2006.
- [11] E. Chest, D. Estublier, B. Fallis, E. Gengembre, J. Gonzalezdelamo, N. Kutufa, D. Nicolini, G. SACCOCCIA, L. CASALINO, and P. DUMAZERT, “Flexible variable-specific-impulse electric propulsion systems for planetary missions,” *Acta Astronautica*, vol. 59, pp. 931–945, Oct. 2006.
- [12] C. A. Cattell, “S3-3 satellite instrumentation and data,” *The IMS Source Book: Guide to the International Magnetospheric Study Data Analysis*, pp. 91–98, 1982.
- [13] F. S. Mozer, C. W. Carlson, M. K. Hudson, R. B. Torbert, B. Parady, J. Yatteau, and M. C. Kelley, “Observations of Paired Electrostatic Shocks in the Polar Magnetosphere,” *Physical Review Letters*, vol. 38, no. 6, pp. 292–6, 1977.
- [14] P. M. Kintner, M. C. Kelley, R. D. Sharp, A. G. Ghielmetti, M. Temerin, C. Cattell, P. F. Mizera, and J. F. Fennell, “Simultaneous Observations of Energetic (keV) Upstreaming and Electrostatic Hydrogen Cyclotron Waves,” *Journal of Geophysical Research*, vol. 84, no. A12, pp. 7201–7212, 1979.
- [15] D. M. Klumpar, “Transversely Accelerated Ions: An Ionospheric Source of Hot Magnetospheric Ions,” *Journal of Geophysical Research*, vol. 84, no. A8, pp. 4229–4237, 1979.
- [16] E. Ungstrup, D. M. Klumpar, and W. J. Heikkila, “Heating of Ions to Superthermal Energies in the Topside Ionosphere by Electrostatic Ion Cyclotron Waves,” *Journal of Geophysical Research*, vol. 84, no. A8, pp. 4289–4296, 1979.
- [17] NASA Science News, “Up, Up, and away to the Magnetosphere - NASA Science,” 1999.
- [18] M. D. Montgomery, J. R. Asbridge, and S. J. Bame, “Vela 4 Plasma Observations near the Earth’s Bow Shock,” *Journal of Geophysical Research*, vol. 75, no. 7, pp. 1217–1231, 1970.
- [19] A. K. Ram, A. Bers, and D. Benisti, “Ionospheric ion acceleration by multiple electrostatic waves,” *Journal of Geophysical Research*, vol. 103, no. A5, pp. 9431–9440, 1998.

- [20] D. M. Klumpar, “Transversely accelerated ions - An ionospheric source of hot magnetospheric ions,” *Journal of Geophysical Research*, vol. 84, no. A8, pp. 4229–4237, 1979.
- [21] G. Lu, P. H. Reiff, T. E. Moore, and R. A. Heelis, “Upflowing Ionospheric Ions in the Auroral Region,” *Journal of Geophysical Research*, vol. 97, no. A11, pp. 16855–16863, 1992.
- [22] P. Satyanarayana, P. K. Chaturvedi, M. J. Keskinen, J. D. Huba, and S. L. Ossakow, “Theory of the Current-Driven Ion Cyclotron Instability in the Bottom-side Ionosphere,” *Journal of Geophysical Research*, vol. 90, no. A12, pp. 12209–12218, 1985.
- [23] A. W. Yau, B. A. Whalen, A. G. McNamara, P. J. Kellogg, and W. Bernstein, “Particle and Wave Observations of Low-Altitude Ionospheric Ion Acceleration Events,” *Journal of Geophysical Research*, vol. 88, no. A1, pp. 341–355, 1983.
- [24] C. R. Chappell, T. E. Moore, and J. H. Waite, “The Ionosphere as a Fully Adequate Source of Plasma for the Earth’s Magnetosphere,” *Journal of Geophysical Research*, vol. 92, no. A6, pp. 5896–5910, 1987.
- [25] M. Lockwood, M. O. Chandler, J. L. Horwitz, J. H. Waite, T. E. Moore, and C. R. Chappell, “The Cleft Ion Fountain,” *Journal of Geophysical Research*, vol. 90, no. A10, pp. 9736–9748, 1985.
- [26] R. T. Tsunoda, R. C. Livingston, J. F. Vickrey, R. A. Heelis, W. B. Hanson, F. J. Rich, and P. F. Bythrow, “Dayside Observations of Thermal-Ion Upwellings at 800-km Altitude: An Ionospheric Signature of the Cleft Ion Fountain,” *Journal of Geophysical Research*, vol. 94, no. A11, pp. 15277–15290, 1989.
- [27] S. Alba, G. Carbone, M. Fontanesi, C. Galassi, C. Riccardi, and E. Sindoni, “Electrostatic ion cyclotron waves in a low magnetized plasma,” *Plasma Physics and Controlled Fusion*, vol. 34, no. 2, p. 147, 1992.
- [28] F. Skiff, F. Anderegg, and M. Tran, “Stochastic particle acceleration in an electrostatic wave,” *Physical Review Letters*, vol. 58, pp. 1430–1433, Apr. 1987.
- [29] J. Goree, M. Ono, and K. L. Wong, “Observation of the backward electrostatic ion-cyclotron wave,” *Physics of Fluids*, vol. 28, no. 9, p. 2845, 1985.

- [30] S. L. Cartier, N. D'Angelo, and R. L. Merlino, "A Laboratory Study of Ion Energization by EIC Waves and Subsequent Upstreaming along Diverging Magnetic Field Lines," *Journal of Geophysical Research*, vol. 91, pp. 8025–8033, July 1986.
- [31] R. W. Motley and N. D'Angelo, "Excitation of Electrostatic Plasma Oscillations near the Ion Cyclotron Frequency," *Physics of Fluids*, vol. 6, p. 296, Dec. 1963.
- [32] C. Karney and A. Bers, "Stochastic Ion Heating by a Perpendicularly Propagating Electrostatic Wave," *Physical Review Letters*, vol. 39, pp. 550–554, Aug. 1977.
- [33] D. Benisti, A. K. Ram, and A. Bers, "Ion dynamics in multiple electrostatic waves in a magnetized plasma. I. Coherent acceleration," *Physics of Plasmas*, vol. 5, no. 9, p. 3224, 1998.
- [34] D. Benisti, A. K. Ram, and A. Bers, "Ion dynamics in multiple electrostatic waves in a magnetized plasma. II. Enhancement of the acceleration," *Physics of Plasmas*, vol. 5, no. 9, p. 3233, 1998.
- [35] R. Spektor and E. Y. Choueiri, "Ion acceleration by beating electrostatic waves: domain of allowed acceleration," *Physical Review E - Statistical, Nonlinear and Soft Matter Physics*, vol. 69, no. 4 Pt 2, p. 046402, 2004.
- [36] R. Spektor and E. Y. Choueiri, "Measurements of Ion Energization by a Pair of Beating Electrostatic Ion Cyclotron Waves," *International Electric Propulsion Conference*, pp. 1–11, 2005.
- [37] B. Jorns and E. Y. Choueiri, "Experiment for Plasma Energization with Beating Electrostatic Waves," *International Electric Propulsion Conference*, pp. 1–11, 2009.
- [38] B. Jorns and E. Y. Choueiri, "Ion Heating with Beating Electrostatic Waves," *Physical Review Letters*, vol. 106, Feb. 2011.
- [39] P. M. Bellan, *Fundamentals of plasma physics*. Cambridge University Press, 2006.
- [40] B. Jorns and E. Y. Choueiri, "Optimal Frequency for Plasma Heating with a Single Electrostatic Wave," *Joint Propulsion Conference*, no. July, 2010.

- [41] R. J. Goldston and P. H. Rutherford, *Introduction to Plasma Physics*. Institute of Physics Pub., 1995.
- [42] C. K. Birdsall and A. B. Langdon, *Plasma physics via computer simulation*. Taylor & Francis, 2004.
- [43] M. Sofroniou and G. Spaletta, “Symplectic Methods for Separable Hamiltonian Systems,” *Proceedings of the International Conference on Computational Science*, pp. 506–515, Apr. 2002.
- [44] R. Talman, *Geometric mechanics*. John Wiley and Sons, 2000.
- [45] D. D. Holm, *Dynamics and symmetry*. Imperial College Press, 2008.
- [46] H. Yoshida, “Symplectic Integrators for Hamiltonian Systems: Basic Theory,” *Chaos*, 1992.
- [47] P. J. Channell and C. Scovel, “Symplectic integration of Hamiltonian systems,” *Nonlinearity*, vol. 3, no. 2, p. 231, 1990.
- [48] H. M. Antia, *Numerical methods for scientists and engineers, Volume 1*. Birkhäuser, 2002.
- [49] J. Candy and W. Rozmus, “A symplectic integration algorithm for separable Hamiltonian functions,” *Journal of Computational Physics*, vol. 92, pp. 230–256, Jan. 1991.
- [50] L. N. Hand and J. D. Finch, *Analytical Mechanics*. Cambridge University Press, 1998.
- [51] F. Reif, *Fundamentals of Statistical and Thermal Physics*. Waveland Press, 2008.

Honor Code

This thesis represents my own work in accordance with University regulations.

Bayard G. Gardineer, IV